DEVELOPMENT AND CHARACTERIZATION OF A HIGH-SPEED MATERIAL-TESTING MACHINE, AND EXPERIMENTAL ANALYSIS OF FRICTIONAL FLASH HEATING AND DYNAMIC WEAKENING IN ROCK

A Dissertation

by

OMID SABER

Submitted to the Office of Graduate and Professional Studies of
Texas A&M University
in partial fulfillment of the requirements for the degree of

DOCTOR OF PHILOSOPHY

Chair of Committee,	Jorge L. Alvarado
Co-Chair of Committee,	Frederick M. Chester
Committee Members,	Gholamreza Langari
	Benchun Duan
Head of Department,	Andreas A. Polycarpou

August 2017

Major Subject: Mechanical Engineering

ABSTRACT

Experimental investigation of dependence of sliding-friction on velocity is necessary to understand the physics of earthquakes. Velocity-dependent friction is ideally studied in experiments by imposing step-wise changes in sliding-rate. In this dissertation, a novel High-Speed Biaxial (HSB) testing machine capable of imposing steps from quasi-static (1 $mm.s^{-1}$) to seismic (1 $m.s^{-1}$) sliding-rates has been developed and characterized. The HSB can achieve steps to seismic sliding-rates in only a few milliseconds under loads as high as 0.5 MN. Herein, the dynamics of the hydro-pneumatic loading-system of the HSB is studied, and by developing an analytical model, feasibility of achieving the desired velocity-steps under different load-path scenarios is assessed. Moreover, the HSB prototype is instrumented and tested to validate the model analysis. Based on the experimental results, a model of vibrations is developed for the continuous loading-system. The model is used to identify and treat vibration sources in the HSB prototype, and a modified design is proposed to reduce vibrations in the ultimate testing machine.

After development and verification of the HSB prototype, a series of sliding friction experiments were conducted to study dependence of friction on sliding-rate, slip history and normal-stress. At seismic sliding-rates, frictional heating can lead to dramatic frictional-weakening in rock. Here, I report on high-speed friction experiments for which flash-heated contacts are thermally imaged on rock samples. The thermographic images provide the first documentation of the geometry and spatial

distributions of load-bearing contacts formed in rock during frictional sliding at seismic rates. The thermographs display a highly heterogeneous distribution of temperature and stress at millimetric scale. The maximum temperature observed in our experiments (500 °C) is remarkably higher than average surface temperature calculated by other studies (100 °C), which reflects the localization of stress to small portions of the contact surface. The observations indicate that, opposed to the original micro-scale flash-weakening model, flash-heating occurs in multiple length- and time-scales. Accordingly, a multi-scale flash-weakening model is proposed and developed, which can simulate the transient friction more accurately. The new findings can play a key role in understanding nucleation and propagation of earthquake ruptures in natural faults.

DEDICATION

Dedicated to Zahra, Gholamhossein, and Nima, for their endless love, support and encouragement throughout my life.

ACKNOWLEDGEMENTS

I would like to express my special appreciation and thanks to Dr. Frederick Chester for all his contributions of time, ideas, and funding to make my PhD experience productive and stimulating. I am grateful for giving me the opportunity to learn and develop, and greatly appreciate your enthusiasm and immense knowledge.

I would like to express my sincere gratitude to Dr. Jorge Alvarado for his constant support, understanding and guidance throughout my study and writing of this dissertation. Thank you for giving me the opportunity to join this research project.

Also, I would like to thank my thesis committee members Dr. Gholamreza Langari and Dr. Benchun Duan for their support and insightful suggestions.

Thanks also to Clayton Powell for his assistance in the laboratory.

CONTRIBUTORS AND FUNDING SOURCES

This work was supported by a dissertation committee consisting of Professor Jorge Alvarado [chair of committee] and Professor Gholamreza Langari of the Department of Mechanical Engineering and the Department of Engineering Technology and Industrial Distribution, and Professor Frederick Chester [co-chair of committee] and Professor Benchun Duan of the Department of Geology and Geophysics.

All work conducted for the dissertation was completed by the student independently under advisement of Professor Frederick Chester and Professor Jorge Alvarado.

Funding Sources

This work was supported by the National Science Foundation under Grant No. EAR-1126762 and Texas A&M University.

TABLE OF CONTENTS

Page

Page

Page

LIST OF FIGURES

Page

Page

Page

Page

LIST OF TABLES

Page

CHAPTER I

INTRODUCTION[1]

1. 1 Motivation

In order to develop earthquake forecasting models, it is necessary to understand the physics of earthquakes. In the last two decades, several drilling programs have been undertaken to probe active faults. However, the costs of fault drilling projects are significantly high, and the maximum depth that can currently be drilled is limited. An alternative approach to studying earthquake mechanics is to combine laboratory experiments and numerical modeling with field geology. Frictional instabilities in fault zones have long been recognized as the cause of earthquakes; however, the underlying physical mechanisms associated to these instabilities are not well-understood or quantified. One characteristic that has a significant importance to the stability of frictional systems is the transient weakening and strengthening of friction associated with changes in the sliding rate [*Dieterich,* 1978; *Ruina*, 1983]. Shallow earthquakes reflect frictional slip instabilities on faults within the elastically stressed Erath's crust that can naturally arise if the coefficient of static friction is greater than that of kinetic

[1] Part of the data reported in this chapter is reprinted with permission of Springer from "Development of a Material-Testing Machine for Study of Friction: Experimental Analysis of Machine Dynamics and Friction of Rock." by O. Saber, F. M. Chester, and J. L. Alvarado (2016), *Experimental Mechanics* 56.5 (2016): 813-831, Copyright 2016 by Society for Experimental Mechanics.

friction. The Earth's crust, which is the outermost layer of rock in the Earth, is not a single solid piece, but is part of several tectonic plates that are normally bonded on the boundaries (i.e. are locked). However, because of tectonic plate motion, the crust is stressed and stores elastic energy. Accumulated stored energy can break the bonds across the faults and the bounding crust may begin to slide. If the sliding friction reduces with velocity, slip rate grows even further which lead to an unstable slip (i.e. an earthquake). Therefore, the mechanics of earthquake faulting is more broadly understood in the context of rate- and state-variable friction constitutive laws that describe the dependence of the coefficient of friction on sliding velocity and slip history. Velocity-dependent friction can explain a host of earthquake phenomena, including earthquake nucleation, aftershocks, triggered slip, and some characteristics of rupture propagation, as well as the recurrent healing and weakening necessary to produce stick-slip[2]; however, many aspects of friction are poorly understood, particularly at seismic slip rates[3]. Therefore, to fully understand dynamic rupture propagation and rupture arrest, it is essential to develop constitutive relations that define the dependence of friction on velocity [*Dieterich*, 1978; *Rice*, 2006; *Ruina*, 1983; *Marone*, 1998]. The rate and state

[2] Stick-slip is referred to cyclic locking and slipping intervals of two sliding surfaces. Stick-slip is best understood with a mass-spring model, where the spring is pushed against the mass to slide it on a frictional surface [*Dietrich*, 1978]. If a large and abrupt decay occurs in friction (as it switches from static to kinetic friction), the work done by friction up to static force equilibrium point is lower than the stored energy in the spring (converting to kinetic energy of mass), and therefore, the mass continues to slide and passes the static equilibrium point. Slip continues until the kinetic energy of the mass decreases to zero, and since it has passed the force equilibrium point, the driving force cannot continue to move it. In addition, friction increases as velocity decreases and static friction is achieved initiating another interval of sticking. Stability of slip depends on the velocity-weakening characteristics of rock (e.g. how abruptly friction changes), stiffness of the medium, and loading conditions (for more details see [*Dietrich*, 1978]).

[3] Seismic slip rates, also referred to as high-sliding rates in this dissertation, are in the range of 0.1-10 m/s. Based on displacement of natural faults and duration of earthquakes, the seismic slip-rate is found to be ~1 m/s in average.

constitutive relations that have been formulated are consistent with experimental observations at slow sliding rates and can successfully describe the effect of sliding rate, temperature and high normal stress on frictional strength of rocks [*Chester*, 1994]. However, these constitutive relations are based only on quasi-static experiments; laboratory testing apparatuses typically operate at sliding rates lower than 1 $mm.s^{-1}$ [*Linker and Dieterich*, 1992; *Chester*, 1994; *Marone*, 1998]. It is not clear whether these constitutive relations can describe behaviors at seismic sliding rates during an earthquake, which can be on the order of 1 $m.s^{-1}$ [e.g., *Niemeijer et al.*, 2012]. In natural faults, and at high slip-rates, significant frictional heating is possible which may lead to dramatic thermal weakening (e.g., melt lubrication at the true microscopic contact-junctions). In this dissertation, a High-Speed Biaxial (HSB) material-testing machine is developed to slide a rock sample sandwiched in between two stationary side-blocks under an adjustable normal stress. The normal stress simulates the normal load between bounding crustal rock along natural faults. The HSB is developed to impose step-like jumps in sliding rate so that the velocity dependence of friction can be investigated.

1. 2 Experimental testing of rock friction

In general, experiments designed to investigate the frictional behavior of rock generally involve sliding the surfaces of two blocks of rock past each other. In these tests, the rock blocks do not fail or break but slide on either fractured or pre-cut, prepared surfaces with or without an intervening layer of granular material called a

gouge layer[4] [e.g., *Paterson and Wong*, 2005]. Friction is represented by the stress across the sliding surface, specifically the shear stress parallel to the sliding direction divided by the normal stress on the surface. Friction tests can be conducted on confined or unconfined samples. In confined tests, samples are sealed in an impermeable membrane and surrounded by a pressurized gas or a fluid at a confining pressure, P_c. Confined tests simulate the high pressure condition in a depth of earth where an earthquake occurs. P_c is caused by overburden weight of layers of rock above of the nucleation point of the fault slip. In experiments, samples may be permeated by a fluid, normally water, at a pore fluid pressure, P_p, which is used to simulate the pressure of fluids in the fault acting in the pore spaces and cracks. Such a pressure tends to cause tension stress and open up pores and cracks. In contrast, P_c causes the cracks to be closed and restrict cracks propagation. As a result, at P_c, samples can bear even large P_p as long as $P_p<P_c$. Generally, the effective pressure P_e, which is equal to $P_c - P_p$, contributes to the normal stress. P_e determines the strength of rock against shear stresses. The shear strength of rocks is enhanced as P_e increases in a confined experiment.

1.2.1 Earthquake conditions

Earthquake conditions should be well-understood to be able to replicate them in laboratory testing conditions. The important parameters in simulating shallow crustal earthquakes are listed in Table 1.1, and the ranges of these parameters are presented. Earthquake-generating crustal fault zones are geometrically and compositionally

[4] Gouge layer consists of non-cohesive rock materials with super fine grains naturally created in fault zone as a result of rock surface wear.

complex. Faults consist of broad tabular zones of fractured rock bounding localized zones of concentrated deformation [e.g., *Chester and Logan*, 1986; *Chester and Chester*, 1998]. Frictional slip during earthquakes generally occurs within highly localized deformation zones containing fine (nanometric) granular material and discrete sliding surfaces, and the frictional properties of the localized deformation zones is considered central to the mechanics of earthquakes [e.g., *Niemeijer et al.*, 2012]. The geometrical attributes of localized deformation zones and slip surfaces vary over micrometer to kilometer length scales [e.g., *Sagy and Brodsky*, 2009]. However, conducting experiments on large scale samples (meter-sized samples) has shown that although the distribution of localized areas and wavelength of deformation are different compared to cm-sized samples, the microscopic mechanisms of deformation and weakening in the localized areas are similar to those in cm-sized samples [*Yamashita et al*., 2015]. Testing machines such as the one presented in this dissertation, employ centimeters to decimeter size samples that simulate localized deformation zones in natural faults. These serve to provide macroscopic friction laws useful for modeling at larger length scales, as well as the means to investigate the important chemical and physical processes operating at smaller length scales that give rise to frictional behavior.

Table 1.1: List of important parameters in simulating shallow crustal earthquakes and their ranges

Acceleration ($\dot{V}$)	$0.1 - 10^5$ ($m.s^{-2}$)
Velocity (V)	$0 - 10$ ($m.s^{-1}$)
Temperature (T)	25 – 350 (°C)
Pore Pressure (P_p)	0 – 100 (MPa)
Displacement (D)	0 – 1 (m)
Normal stress (NS)	0 – 250 (MPa)

1.2.2 Testing machines for simulating earthquakes in the lab

Friction experiments are generally done in four configurations as summarized in Figure 1.1. Thus far, most friction experiments at seismic sliding rates have been conducted in rotary-shear and impact-shear configurations [*Di Toro et al*., 2011; *Ma et al*., 2014; *Chang et al*., 2012; *Tisato et al*., 2012; *Proctor et al*., 2014; *Yao et al*., 2016a; *Yuan and Prakash*, 2008]. Rotary machines are popular for high-speed friction experiments because unlimited slip distances can be achieved using these machines (cylindrical samples can be twisted against each other for many turns). However, to date, confinement of samples has not been possible and these machines cannot operate at high normal stresses [*Neimeijer et al.*, 2012]. Although impact type tests can be conducted at very high normal stress and slip rates, confinement of the sample is not feasible in this configuration either, and the distance of frictional sliding is very small (1 mm or less). On the other hand, in triaxial and biaxial apparatuses, jacketed samples can be employed in pressure vessels to investigate the effects of pore fluid and confining pressure [e.g.,

Carpenter et al., 2009], but the existing machines in these two configurations use conventional servo-hydraulic loading systems and work at quasi-static sliding rates[5], and displacement cannot be very high (1-10 cm). The limitations of the existing friction testing-machines in achieving earthquake conditions are summarized in Table 1.2.

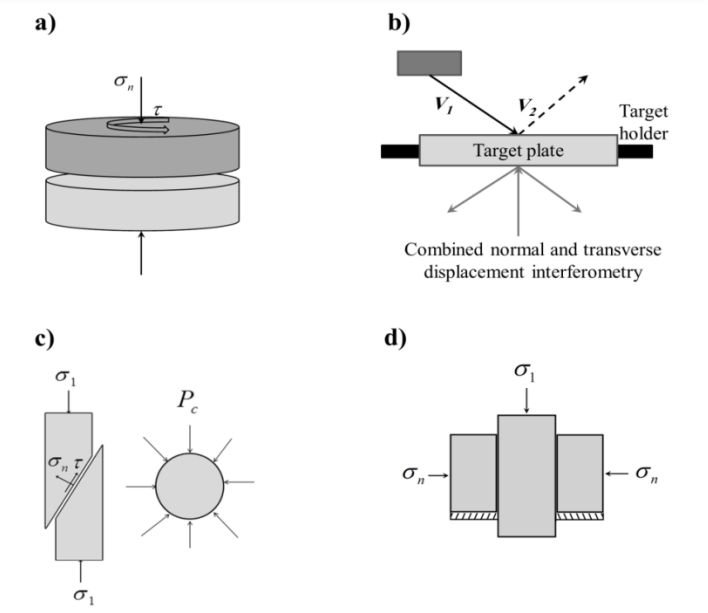

Figure 1.1: Comparison of different testing configurations. a) In rotary shear tests, two cylinders or rings of rock are rotated relative to each other about the cylinder axis. b) Impact type tests incorporate a contact surface that has an angle to the impact direction (V_1) and that undergoes frictional slip. c) In a triaxial friction test, a cylindrical sample containing an inclined fracture or precut surface is placed under P_c and loaded parallel to its axis to induce sliding of the sample [e.g., *Chester and Higgs*, 1992]. d) In a double direct shear test configuration, the sample is sandwiched between two stationary blocks of rock loaded in a direction perpendicular to the contacting surfaces by a normal stress σ_n. The central block is also loaded with a vertical force to generate shear stress on the contacting surfaces to cause sliding between the central and lateral blocks [e.g., *Dieterich*, 1978].

[5] In this dissertation, quasi-static friction is referred to coefficient of friction at sliding rates equal or lower than 1 mm/s.

Table 1.2: Current limitations of the existing friction testing machines in achieving earthquake conditions. The parameters were defined in Table 1.1.

Test Condition	Rotary test	Impact test	Triaxial test	Double-direct test
$\dot{V}$	Limited	Possible	Limited	Limited
V	Possible	Possible	Limited	Limited
T	Limited	Limited	Possible	Possible
P_p	Not Possible	Not Possible	Possible	Possible
D	Possible	Not Possible	Not Possible	Not Possible
NS	Limited	Possible	Possible	Possible

1. 3 Friction constitutive relations at quasi-static sliding-rate

As explained above, constitutive equations of friction have been successfully developed at static and quasi-static sliding conditions. In this section, those constitutive equations are briefly reviewed. Experimental analyses of friction have shown that if two non-sliding surfaces are in contact under a normal stress for duration of *t*, static friction increases with *t* based on a logarithmic relation [*Dietrich*, 1978]:

$$\mu = \mu_0 + A\log(Bt+1) \tag{1.1}$$

where, μ_0, A, B are constants. This relation indicates that strength of the bonds between the micro-scale contacts from the two surfaces increases with age of the contact. A similar behavior can be expected for sliding friction; i.e. as velocity is increased, duration of contacts (lifetime of contacts) decreases and the steady state shear stress (and

consequently friction) reduces. Accordingly, velocity dependence of the steady-state friction can be described with the following relation [*Dietrich*, 1978]:

$$\mu = \mu_0 + A \log\left(B \frac{d_c}{V} + 1 \right) \tag{1.2}$$

where, d_c is a characteristic slip distance related to dimension of micro-scale asperities, in which the population of contacts updates (lifetime of contacts reduces due to jump in velocity). Velocity dependence of the transient friction is presented by defining state variables. A simple form of rate-and-state relation can be written as [*Scholz*, 1998]:

$$\mu = \mu_0 + a \ln\left(\frac{V_2}{V_1} \right) + b \ln\left(\frac{V_1 \phi}{d_c} \right) \tag{1.3}$$

$$\frac{d\phi}{dt} = 1 - \left(\frac{V_2 \phi}{d_c} \right) \tag{1.4}$$

where, ϕ is a state variable (ϕ can be described as the age of contacts), V_1 is the initial velocity and V_2 is the current velocity. In the steady-state condition, the right hand side of Equation (1.4) vanishes, thus, $\phi_{ss} = \frac{d_c}{V_2}$. Rate-and-state relations are best investigated by using velocity-steps as illustrated in Figure 1.2a. In these experiments, velocity is changed by a large ratio in a short displacement while other parameters are maintained unchanged. In this way, the independent effect of velocity on friction can be observed while the effect of other parameters such as slip distance on friction is eliminated.

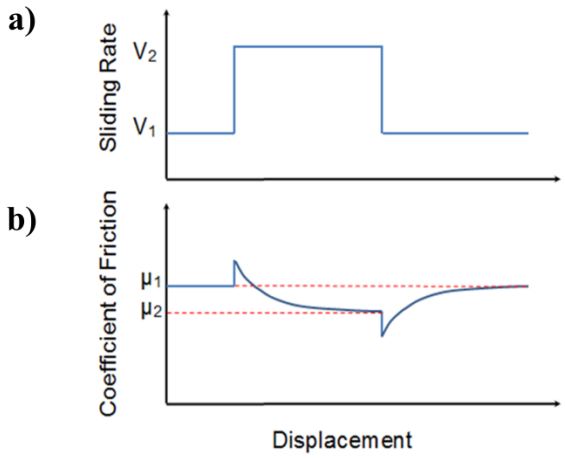

Figure 1.2: Velocity dependence of friction is best explored with velocity-steps.a) An example of a velocity-step from sliding rate of V_1 to V_2, and V_2 back to V_1, b) the transient friction for a general case of velocity-weakening at quasi-static sliding rates is shown.

As shown in Figure 1.2b, upon a jump in velocity, two phases can be recognized in the transient friction: 1) an instantaneous change in friction which mainly occurs due to an increase in shear-strength caused by the increase in the strain-rate, and 2) gradual reduction of friction with slip. The gradual change in friction occurs due to the evolution of contacts at micro-scale asperities (i.e. reduction of contact duration). When velocity is stepped down to V_2, the opposite of these processes occur resulting in an instantaneous weakening followed by gradual strengthening. At quasi-static sliding rates, after resuming velocity to the initial sliding rate (V_1), the steady-state friction is also resumed to the initial steady-state friction level (this process is called recovery or healing), and

the process is almost reversible. At quasi-static sliding rates, temperature of the contacts does not change much, and dependence of velocity on friction is low[6].

1. 4 Dynamic weakening of friction (at seismic slip rates)

While friction does not change significantly during velocity stepping experiments at quasi-static sliding rates, the majority of friction experiments done at seismic sliding-rates indicate a dramatic decay of friction force called dynamic weakening. High sliding-rate can generate significant increase in temperature of surface due to frictional heating. The temperature rise in a friction experiment depends on the rate of heat generation per unit of area ($\tau(t).V(t)$) which is controlled mainly by normal stress, sliding rate, and slip history. High temperature may activate a number of weakening mechanisms, such as phase transition [*Proctor et al*., 2014], chemical decomposition [*Tisato et al*., 2012], generation of pressurized fluids (which decreases the effective normal stress, P_e) [*Rice*, 2006], and melt lubrication (melt along the sliding surface can act like a lubricant and decreases the frictional strength of rock surfaces) [*Di Toro et al*., 2011]. As a result of dynamic weakening, the coefficient of friction[7] can undergo a fivefold decease to values as low as 0.1-0.2. Other proposed weakening mechanisms include moisture drainage, silica gel formation and nano powder lubrication [*Niemeijer et al*., 2012].

Dynamic weakening occurs upon a step to sliding-rates above ~0.1 $m.s^{-1}$ regardless of rock type and the weakening micro-mechanism [*Di Toro et al.,* 2011]. However, the characteristic parameters that define friction evolution vary between

[6] Generally, at quasi-static sliding rates, only a few percent of change in friction is observed when velocity is changed by a factor of 10.

[7] Quasi-static coefficient of friction magnitude is usually 0.6-0.8.

different experiments conducted under different conditions. The main characteristic parameters are: 1) friction peak, μ_p (which may be very close to quasi-static friction), 2) the steady-state fiction magnitude, μ_{ss}, and 3) a characteristic slip-weakening distance, D_c over which 90% of weakening occurs. Using these 3 parameters, dynamic weakening is generally estimated by an exponential decay as shown in Figure 1.3. D_c is also known as the weakening distance "D_w" and thermal slip distance "D_{th}" in the literature, but is different from the characteristic distance defined in friction evolution at quasi-static rates (d_c), which is a material property related to contact size and distribution of asperities.

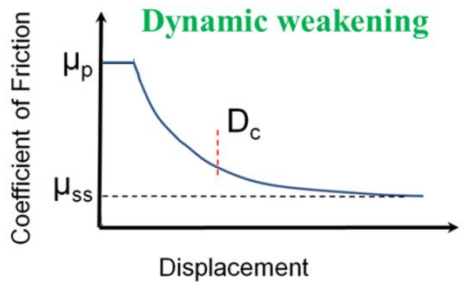

Figure 1.3: Dynamic weakening in rock. The coefficient of friction decreases dramatically (often modeled by an exponential decay) after onset of sliding at seismic rates. D_c is the distance, in which, 90% of the decay occurs.

In addition to the friction experiments conducted on bare surfaces of rock samples, experiments have been done on gouge layers to simulate debris and wear material at the fault slip zone (which can be the remaining products of the fault slip in the past). Gouge material may consist of fine granular material of a single mineral or a mixture of multiple minerals. Dynamic weakening may happen in a small weakening

distance for gouge materials as well when the shear deformation occurs in a very thin section of the gouge layer [*Goldsby and Tullis*, 2011]. This is called localization of slip; i.e. slip is localized in a thin layer called slip zone, where slip rate has a great gradient [*Kitajima et al*., 2011]. Figure 1.4 shows the difference of a localized slip to distributed slip in gouge layer.

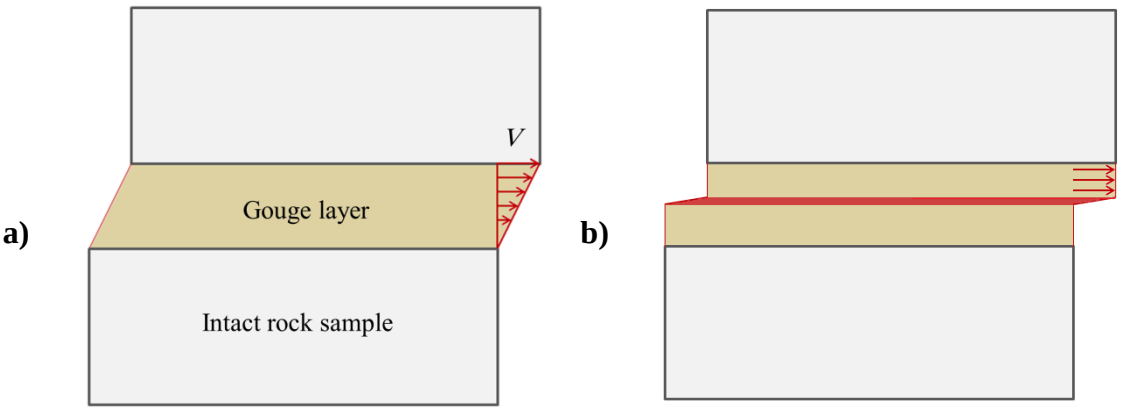

Figure 1.4: Localization of slip in gouge material. a) Strain is distributed in the entire gouge layer; b) slip is localized in a thin zone of gouge layer which can lead to a small weakening distance.

1.4.1 Flash heating and flash weakening (effect of velocity on weakening)

As discussed above, frictional heating at seismic sliding-rates can lead to thermal weakening of rock and cause a dramatic decay in the apparent friction. However, macroscopic weakening processes such as generation of bulk melt on the surface are not necessary for dynamic weakening. Experiments have shown that weakening can occur at micro-scale asperities before bulk surface temperature reaches melt temperature.

Theories of macroscopic friction behavior in brittle rock consider that the true contact area, at microscopic scale asperities, can be much smaller than the apparent, macroscopic area of contact as illustrated in Figure 1.5. Existence of microscopic contacts have been confirmed by imaging the sliding surface within transparent materials [*Dieterich and Kilgore*, 1996; *Hulikal et al.*, 2015] as well as analyzing the morphological features on slipped surfaces. Also, the local shear strength of asperity contacts, τ_c, is much higher than the macroscopic shear strength. τ_c is on order of ~10% of elastic shear modulus; i.e. several GPa [*Boitnott*, 1992]. It has been shown that the work done by friction during slip is mainly converted to heat, so at sufficiently high rates of sliding, the local temperature at micro-scale asperity contacts is raised rapidly. Elevated local temperatures at microscopic asperities may result in phase transition, chemical decomposition, and melt generation along the micrometer-scale contact interfaces. As a result of activation of these micro-mechanisms of weakening, τ_c and consequently the macroscopic friction reduce [*Rice*, 2006]. The sharp rise in temperature at high slip-rate and high local stress is called *Flash Heating* and the macroscopic weakening response resulting from flash heating is referred to as *Flash Weakening*.

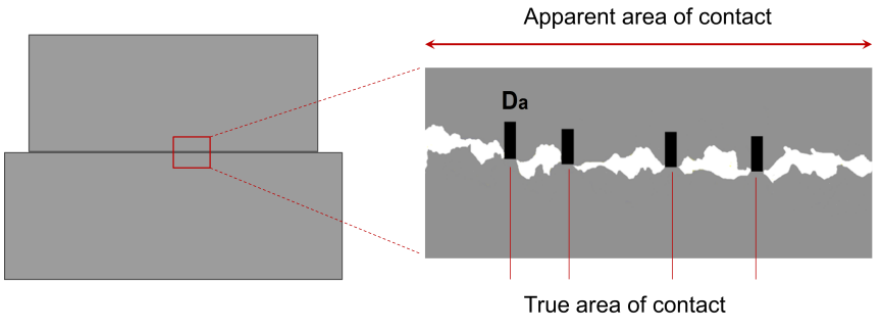

Figure 1.5: Comparison of the true and apparent areas of contact. The true area of contact is only a few percent of the apparent area of contact; D_a is the dimension of a micro-scale asperity which is on the order of several micro-meters. At the micro-scale of contacts, strength approaches the theoretical strength of material which is on order of several GPa.

Rice [2006] presented a model for flash weakening formulation for asperity contacts that describes the relation between velocity and friction. Frictional work mainly converts into heat, so, the heat generation rate per unit area of the asperity (on each side of the interface) is equal to $\tau_c \cdot V/2$ (Figure 1.6). By knowing the heat generation rate at each instance, the transient temperature of an asperity surface can be found as a function of slip during the contact lifetime. The basic model of flash weakening assumes that for sliding at velocity, V, asperities on opposing surfaces come into contact and exist for a slip distance of D_a (representative contact dimension), and for a characteristic time of $\theta = D_a / V$ before the contact is lost. Further, contact strength, τ_c, is assumed constant if temperature of the contact, T_c, is less than the temperature for weakening, T_w; and if $T_c \geq T_w$ then contact strength is dramatically reduced (Figure 1.6). The contact length can be as small as a few micrometers, so if the sliding velocity is small, the contact temperature

does not reach the weakening temperature, T_w, and no reduction in macroscopic friction would be observed (i.e. coefficient of friction maintains constant at $\mu_{0)}$.

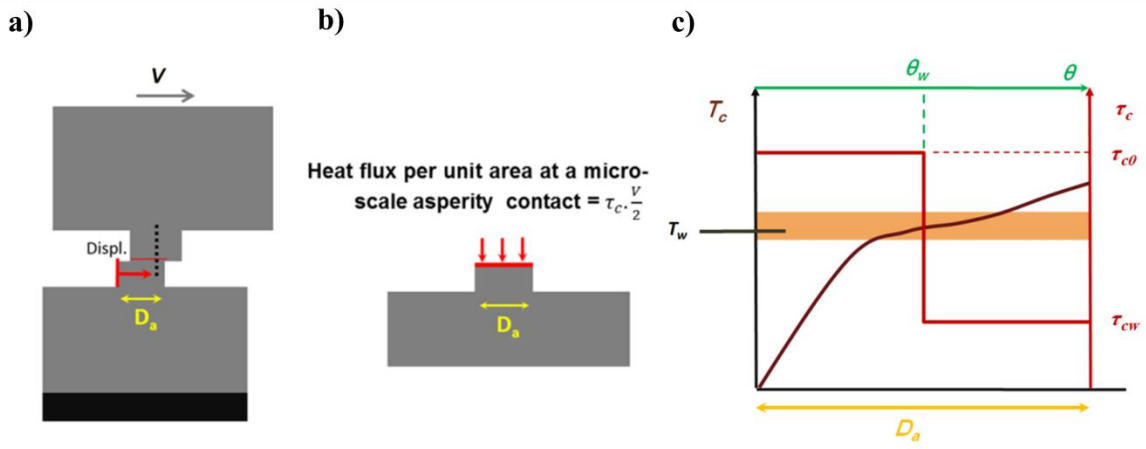

Figure 1.6: Modeling flash weakening at microscopic asperities. a) In the flash weakening model, micro-scale contacts are modeled as square asperities with length of D_a, b) the heat flux at the contact interface can be found based on velocity and shear stress, heat is split between the two surfaces, c) temperature rise during the lifetime of a contact (each point on the asperity is in contact for $\theta=D_a/V$ and is exposed to the above heat flux per unit of area during this time interval). If velocity is higher than a certain limit (V_w), temperature of the asperity surface reaches the weakening temperature (T_w) before the lifetime of the contact ends ($\theta_w < \theta$). In this case, the shear strength of the asperity drops from the initial value (τ_{c0}) to the weakened state (τ_{cw}) which causes a drop in macroscopic coefficient of friction.

In the flash-weakening model, the transient temperature is obtained based on equations of one-dimensional heat conduction in a semi-infinite plane exposed to a planar moving heat source [*Archard*, 1959]. At seismic slip-rates (~1 $m.s^{-1}$) the depth of heat diffusion is small relative to the dimension of a contact, and lateral or 2-D heat diffusion can be neglected to simplify the closed-form formulation [*Rice*, 2006; *Beeler et*

al., 2008; *Proctor*, 2014; *Yao et al*., 2016a, 2016b]. With this assumption, the temperature of the surface of a micro-scale asperity can be estimated as [*Archard*, 1959]:

$$T_C = 2q\sqrt{\frac{t}{\pi\rho K_{th} c_{th}}} + T_{c0} \tag{1.5}$$

where, K_{th} is heat conductivity coefficient, ρ is density of solid, c_{th} is specific heat capacity of material, q is the heat generation rate per unit of area, T_{c0} is the initial temperature of the surface and t is duration of exposure to the heat source. Equation 1.5 can also be written as follows:

$$T_C = \tau_c V\sqrt{\frac{t}{\pi\rho K_{th} c_{th}}} + T_{c0} \tag{1.6}$$

If θ_w is defined as the time, t, for the contact to reach T_w, θ_w can be found as follows:

$$\theta_w = \pi\rho K_{th} c_{th}\left(\frac{Tw - T_{c0}}{\tau_c V}\right)^2 \tag{1.7}$$

The lowest velocity, at which, the temperature of the surface of the asperity can reach T_w, may be found by considering the case where T_w is achieved just at the end of contact duration (i.e. $\theta_w = \theta$). Therefore, this velocity (which is called V_w) can be obtained by setting:

$$\theta_w = \frac{Da}{V_w} \tag{1.8}$$

hence:

$$V_w = \frac{\pi \rho K_{th} c_{th}}{D_a} \left(\frac{T_w - T_{c0}}{\tau_c} \right)^2 \tag{1.9}$$

The mean macroscopic coefficient of friction can be found by averaging the strength of the contacts over their lifetime. As illustrated in Figure 1.6, strength of the asperity is τ_{c0} until $t = \theta_w$. Beyond that point, τ_c drops to τ_{cw} for a duration of $\theta - \theta_w$. Since the coefficient of friction is proportional to τ_c, mean macroscopic friction can be obtained as:

$$\mu = \mu_0 \frac{\theta_w}{\theta} + \mu_w \frac{(\theta - \theta_w)}{\theta} \tag{1.10}$$

and based on definition of θ and Equation 1.8:

$$\frac{\theta}{\theta_w} = \frac{V}{V_w} \tag{1.11}$$

Therefore, Equation 1.10 can be written as [*Rice*, 2006; *Beeler et al*., 2008]:

$$\begin{aligned} &\mu(V) = \mu_w + (\mu_0 - \mu_w) \frac{V_w}{V} && \text{if } V > V_w \\ &\mu(V) = \mu_0 && \text{if } V \leq V_w \end{aligned} \tag{1.12}$$

where μ_0 is the quasi-static coefficient of friction, and μ_w is the lowest coefficient of friction in weakened state. Based on Equation 1.12, if $V >> V_w$, the asperities reach T_w in a small portion of the asperity lifetime and the coefficient of friction approaches μ_w.

The flash-weakening model is generally used to obtain the steady-state friction at a constant sliding-rate [*Goldsby and Tullis*, 2011]; however, it can be used to estimate

the transient friction as well because the changes in velocity are very small during the lifetime of a micro-scale contact. Lifetime of contacts, at seismic sliding rates, is on the order of a few micro-seconds while the changes in velocity in such a short time are negligible and V can be assumed constant. In other words, based on the micro-flash weakening model, the change in friction occurs instantaneously upon a change in velocity. Experiments have shown that in addition to velocity, friction may be changed with slip. This can be explained by including the effect of surface temperature in the model. It is known that macroscopic surface temperature changes with slip due to frictional work. In Equation 1.12, V_w changes with the surface temperature based on Equation 1.9 (the difference between T_w and T_{c0} evolves with slip) [*Proctor et al.*, 2014; *Elbanna et al.*, 2014; *Yao et al.*, 2016a, 2016b]. Thus, changes in T_{c0} with slip can produce a transient, slip-history dependent friction response, which can be observed in high-speed sliding experiments after a velocity-step to constant velocity.

1.4.2 Effect of normal stress on dynamic weakening

Experimental results of high-speed friction tests on rock samples have shown that, generally, the transient and steady-state friction can be affected by normal stress, and the effect of normal stress on the transient friction is mainly studied by investigating the dependence of D_c on normal stress. However, the relation between weakening and normal stress is not well-understood yet [*Niemeijer et al.*, 2012]. Most of the experimental work has been done to explore the effect of normal stress on melt generation which occurs over long slip distances (on the order of 1-10 m), e.g., [*Niemeijer et al.*, 2011; *Han et al.*, 2010; *Brantut et al.*, 2008; *De Paola et al.*, 2011; *Di*

Toro et al., 2011]. Generally, normal stress enhances weakening by decreasing D_c. Several relations have been proposed to indicate how D_c is controlled by normal stress [*Di Toro et al*., 2011; *Niemeijer et al*., 2011]. *Di Toro et al.* [2011] proposed that weakening distance decays as normal stress increases based on the following empirical relation:

$$D_c = a\sigma_n^{-b} \tag{1.13}$$

where *a*, and *b* are constants. *Niemeijer et al.* [2011] studied the dependence of D_c on normal stress and sliding velocity simultaneously. For this purpose, they developed a relation between normal stress and frictional stress based on a power law because the Byerlee's law[8] does not hold when dynamic weakening occurs. In order to obtain a relation between D_c, normal stress and slip rate, *Niemeijer et al.* [2011] calculated the required slip distance, in which, due to frictional work, temperature of the surface rises up to the melt temperature of material. However, theoretical models have not been very successful for three main reasons. Firstly, for weakening mechanisms other than melting, no relation has been postulated between normal stress and friction. Secondly, for the melt lubrication mechanism, the friction dependence on normal stress is very complex

[8] Byerlee's law states that frictional stress is proportional to normal stress regardless of the rock type (i.e. $\tau = \mu . \sigma_n$, and μ is constant; but high-speed friction experiments have shown that the steady-state μ changes with normal stress and the dependence of friction to normal stress is best described by a power law.

during melting and simplified theoretical relations do not hold[9]. Finally, the constant heat flow assumption (constant $\tau.V$) is not valid during the whole weakening process as τ decays with friction. As a result, the theoretical model by [*Niemeijer et al., 2011*] did not fit the experimental results accurately, and instead, they proposed an empirical relation for defining the dependence of D_c on normal stress and slip velocity as follows:

$$\log(D_c) \propto a \log(\sigma_n \sqrt{v}) \tag{1.14}$$

where $a = -1$. Since this relationship is not based on a microphysical model, there are uncertainties about the accuracy of such a relation at high normal stresses or when the weakening mechanism is not based on melt lubrication. For instance, *Han et al.* [2010] and *Brantut et al.* [2008] found a $1/\sigma_n^2$ dependence of D_c on normal stress, while *De Paola et al.* [2011] proposed $D_c = a\sigma_n^{-1.4}$. These three studies were done in presence of gouge layer, and melt lubrication was not the main weakening mechanism. Moreover, those experiments were conducted at low normal stress, and extrapolating the results to real earthquake conditions would not be accurate.

1. 5 Significance of the current work

Most of experiments that have investigated frictional behavior of rocks at high sliding-rates have been done using rotary shear configuration by conducting velocity-stepping experiments. These experiments are mostly done in unconfined configurations,

[9] Based on melt generation, theoretical models by *Nielsen et al.* [2008] indicated a power law with an exponent of 0.25 for relating friction to normal stress; however, *Niemeijer et al.* [2011] found that an exponent close to 0.5 provides better agreement with the experimental data.

so they cannot simulate all aspects of natural earthquake slip conditions (i.e. elevated temperatures, pressurized fluids in pore spaces, and high normal stress). Only few impact friction experiments have been done at high normal stress but conducted in absence of confining fluid and pore pressure. In addition, the acceleration that a rotary friction machine can achieve is normally less than 5g (due to limitations on high torque electrical motors), which is several orders of magnitude lower than that achieved in impact testing and in experiments with stick-slip instabilities. In conclusion, there is a need to develop a friction machine that allows confining pressure, pore fluid pressure, and can operate at velocities and accelerations close to those in real earthquakes. Figure 1.7 shows the range for peak slip acceleration and peak slip velocity for earthquakes, and compares the achievable range of the High-Speed Biaxial (HSB) apparatus (presented in this dissertation) with other existing testing machines. As illustrated in Figure 1.7, the HSB can investigate the transient and steady-state friction at velocities, accelerations, and normal stresses in the earthquake range that could not be investigated with other instruments (intermediate between typical rotary and impact-type testing instruments). For these reasons, we developed a prototype HSB to operate both in triaxial and double-direct configurations for conducting unconfined, dry friction experiments. The ultimate machine, which is under development, allows confined experiments in presence of pore fluid as well. Table 1.2 summarizes the important parameters in simulating earthquakes, the conditions that were achieved with the prototype HSB, and the ones that can be tested by the ultimate machine. Based on displacement range of the HSB, it is best suited for simulating the amount of seismic slip for moderate size earthquakes (M4).

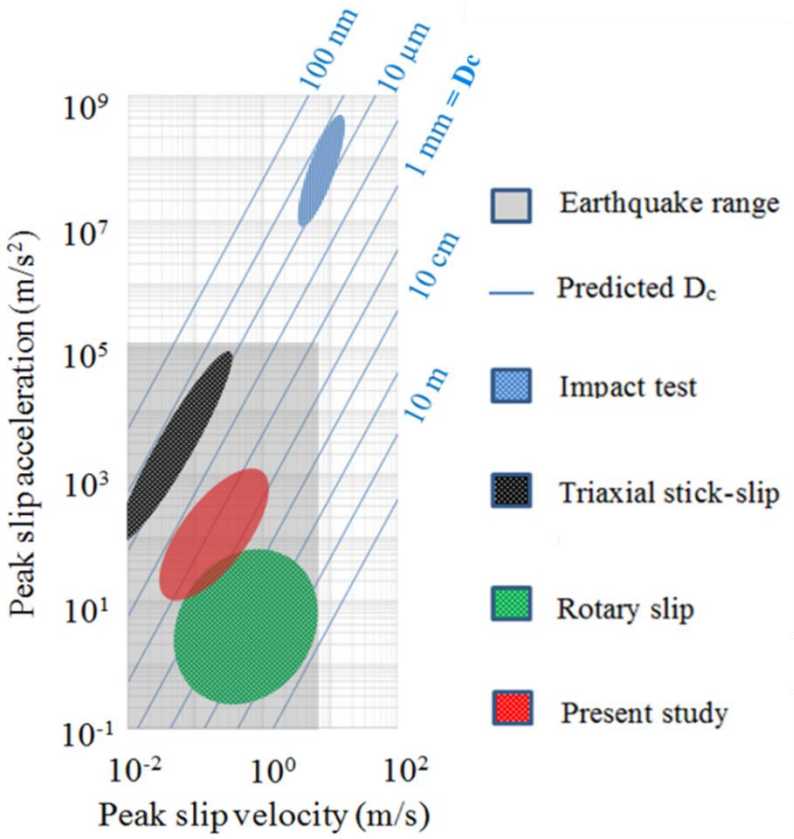

Figure 1.7: Experimental conditions of the HSB and other operational apparatus. The comparison is done in terms of peak slip acceleration and peak slip velocity [*Yuan and Prakash*, 2008; *Chang et al.*, 2012]. Contours of the critical slip distance for weakening, *Dc*, is based on a cohesive crack model and experimental data [*Ohnaka*, 2003]. The expected range of acceleration, normal stress and D_c for the new apparatus falls between those of existing rotary shear, stick-slip triaxial shear, and shear-plate impact experiments.

Table 1.3: List of important parameters in simulating shallow crustal earthquakes and their ranges compared to those of the prototype and ultimate versions of the HSB

	Earthquakes	**Prototyped HSB machine**	**Ultimate HSB machine**
Acceleration ($m.s^{-2}$)	$0.1 – 10^5$	0.1 – 500	$0.1 – 10^3$
Velocity ($m.s^{-1}$)	0-10	10^{-3} to 1	10^{-6} to 1
Temperature °C	25 – 350	25	25 –350
Pore Pressure (MPa)	0 – 100	0	0 – 100
Displacement (m) for M4 earthquake	~0.05	0.05	0.05
Normal stress (MPa)	0 – 250	0-30	0 – 150

To perform velocity-step friction experiments, the loading-system of the HSB needs to achieve high accelerations (up to 50g) with very small rise time during the velocity-steps (velocity should be changed from 0 to 1 $m.s^{-1}$ in only ~4 milliseconds), and maintain constant velocity for about 2 – 4 cm without requiring feedback control. Achieving velocity-steps under high loads (up to 0.5 MN) is challenging particularly when the load evolves dramatically during the experiment (due to dynamic weakening of rock samples). Standard commercial high-load hydraulic loading systems cannot achieve very high accelerations. Therefore, to attain high velocity in short displacements (i.e. small rise time), usually an impact type loading is used. In those experiments, the loading piston is brought to the desired velocity before touching the sample. Then, the piston hits the sample at the desired strain rate [*Bardenheier and Rogers*, 2003]. However, in our application, impact type loading is unacceptable because it can cause ringing, generate undesired stick-slips, and may affect the frictional behavior of rock

samples by inducing large elastic waves. Thus, we used a hydro-pneumatic system to be able to achieve high accelerations. For our application, the rise time of the velocity-step is desired to be below 4 milliseconds, whereas conventional servo systems exhibit time delays of several milliseconds or more because of the response time of valves and also due to control algorithms used in closed-loop controllers [*Schlotter and Plummer*, 2011]. As a result, without feedback control, the hydro-pneumatic system should be designed so that the target velocity path is achieved only by presetting a few adjustable mechanical settings such as orifice valves and the initial pressure in the pneumatic cylinder. Also, it is essential to fully characterize the dynamics of the machine to be able to find the appropriate values for the adjustable mechanical settings. In this dissertation, a mathematical model is developed to study dynamics and vibrations of the machine and investigate the feasibility of generating the desired step-wise velocity pattern. The analytical model is also used to optimize the design of key components of the prototype machine, so that the required load paths can be achieved with less vibration in the ultimate HSB. The prototype HSB was instrumented with several sensors and a high-speed DAQ, and software was developed in LabVIEW using FPGA programing to collect and store experimental data at 50 kHz. Furthermore, a set of experiments were designed and conducted to validate the mathematical model and model parameters were calibrated accordingly.

After validation of the mathematical model, the HSB was used to conduct double-direct friction experiments to investigate the physics of dynamic weakening by flash-heating and study the dependence of friction on normal stress, sliding rate and slip

history. Most of the previous studies have explored melt lubrication which is activated in meter-scale slip distances and may be a key weakening mechanism for large magnitude earthquakes. However, in this dissertation, we focus on the early stages of the transient friction which is important in nucleation and rupture propagation of fault slip. While, rotary shear configuration is best suited for conducting experiments with long slip distances, the high acceleration of the loading system used in the HSB allows studying the early stages of dynamic weakening upon a velocity-step. In the experiments done in this study, bulk melting was not observed. Based on the instantaneous change in friction with velocity at high accelerations, it was concluded that flash-weakening is the major weakening mechanism in our experiments.

In natural faults, the flash-heating mechanism may be the first weakening mechanism activated during high speed sliding, and thus could have a significant role in nucleation of earthquakes. The models of flash heating are sensitive to assumptions of contact geometries and stress at multiple length scales, but to date there is little direct confirmation of the assumptions made regarding high speed sliding in rock. For example, one of the assumptions made in the flash-weakening model is that normal stress at micro-scale asperities is equal to the theoretical strength of the material, which is independent of macroscopic normal stress. As a result, the effect of normal stress on flash weakening has not been investigated sufficiently. However, experimental data have shown that normal stress can have an influence on the magnitude of weakening and the rate of weakening. In this dissertation, the effect of normal stress on flash heating is

analyzed, to demonstrate how normal stress can impact flash weakening by affecting macroscopic temperature, contact stress and contact distribution.

Another major factor in the flash weakening model is the transient temperature of surface at the macroscopic scale, T_s (T_{c0} in Equation 1.9). However, to date, no direct measurements of temperature have been made in high-speed friction experiments to document the magnitude and profile of the transient temperature values on the sliding surface. Measurements of the surface temperature and the heat generated at sliding interfaces could be made by instrumenting a sample with thermocouples close to the contact interface [*Ozisik*, 1992]. Yet, it is very challenging to measure the flash transient temperature at the microscopic- to millimetric scale contacts because at these scales, the spatial and temporal variation of temperature is very high. As a result, measurements should be done at very high sampling rates and resolution. One promising approach is to estimate temperature at contact points based on direct measurements of the temperature of the sliding surface using an infrared camera. By using the double direct shear configuration in the HSB, IR images were directly taken from the surface of the sliding sample as it emerged out of contact using a high-speed infrared camera. The results show that, temperature and stress distribution is highly heterogeneous on the surface (based on the 2-D profile of temperature). Also, the IR images indicate that, in short slip distances (on the order of 10 mm), temperatures as high as 500 °C may be achieved at millimetric-scale contacts even under low to intermediate normal stresses, while the average temperature of surface (that was used in previous studies) would be only 50-150 °C. The observations disclosed new findings about important parameters in the physics

of weakening and led to development of an enhanced model of flash weakening, in which, weakening can be present in multiple time- and length-scales.

CHAPTER II

OBJECTIVES

In this research work, a material-testing machine (HSB) was designed and characterized for study of friction in rock. For this purpose, first, the following objectives were pursued:

- Develop an analytic model to study the dynamics of the high-speed hydro-pneumatic loading system of the HSB.
- Perform numerical model analysis to investigate the possibility of generating the desired velocity paths using the prototype loading-system.
- Study the effect of design parameters and test conditions on the transient velocity.
- Perform workspace analysis to find the range of feasible test conditions.
- Obtain the key design parameters of the machine to achieve the desired workspace.

Next, the prototype of the HSB was developed and tested for validation of the analysis. To test the prototype, it was instrumented with sensors and a DAQ system, and software was developed in LabVIEW to collect data at high sampling rates using FPGA programming. By testing the prototype the following objectives were achieved:

- Investigate the vibrations of the continuous loading system.
- Test the machine to assess its capability of achieving the desired velocity paths.
- Design experiments to calibrate and modify the model using experimental data.

- Perform analytical and experimental analysis to study the interaction of the test-specimen and the hydro-pneumatic loading system under dynamic loading conditions.
- Optimize the design of the HSB to reduce vibrations of the system.

After development and verification of the model of the HSB prototype, a series of sliding friction experiments were designed and conducted to accomplish the following objectives:

- Study dependence of the transient friction on velocity, slip history and normal stress in rock.
- Quantify flash heating by analyzing the temperature magnitude and distribution on the sliding surface.
- Characterize contact areas in millimetric and micrometric scales.
- Study stress localization on the sliding surface based on temperature measurements.
- Analyze the effect of normal stress on contact size, distribution and heterogeneity.
- Propose modification of flash weakening model to include the effects of normal stress on weakening.

Finally, the experimental results were used to develop a flash-weakening model that can represent the dependence of transient friction and dynamic weakening on sliding rate in rock. For this purpose, the following objectives were pursued:

- Incorporate the new findings about temperature and stress heterogeneity on the sliding surface, achieved by the infrared thermographs, to modify the flash weakening model.

- Study the effect of slip history and temperature on the transient friction.
- Present a flash heating model to include the coupled effects of temperature and friction.
- Develop and postulate a multi-scale model of flash weakening which accounts for the observed characteristics of contacts in different length- and time-scales.
- Study the recovery of frictional strength and healing processes during deceleration phase of a seismic slip.
- Study the transient friction under different velocity paths, specifically, velocity-steps and Earthquake-Like Slip Events (ELSE), and validate the proposed model of multi-scale flash-weakening behaviors.

CHAPTER III

DESIGN, DEVELOPMENT AND CHARACTERIZATION OF A MATERIAL-TESTING MACHINE FOR STUDY OF FRICTION[10]

3. 1 Introduction

In this chapter, first, the design analysis of the prototype testing-machine is presented. Next, the testing apparatus is described and an analytical model is developed to investigate the feasibility of achieving the desired step-wise velocity paths. In addition, the effects of different design parameters on the dynamics of the machine are analyzed, and a method of attaining optimum test settings for velocity-step experiments is presented. Finally, the workspace of the apparatus is specified by considering different test-sample behaviors, and the key design parameters are found through modeling so that the machine can operate successfully within the desired range of testing conditions.

3. 2 Design objective

As explained in Chapter I, the rate-and-state friction constitutive relations are best explored through velocity-stepping tests. In this chapter, the primary design

[10] Part of the data reported in this chapter is reprinted with permission from, 1) "Development of a Material-Testing Machine for Study of Friction: Experimental Analysis of Machine Dynamics and Friction of Rock." by O. Saber, F. M. Chester, and J. L. Alvarado, 2016, *Experimental Mechanics* 56.5 (2016): 813-831, Copyright 2016 by Society for Experimental Mechanics, and 2) "Dynamic Analysis of a High-Load, High-Speed Actuator for Rock Deformation Experimentation." by O. Saber, F. M. Chester, and J. L. Alvarado, 2014, ASME 2014 International Design Engineering Technical Conferences and Computers and Information in Engineering Conference. Copyright 2014 by the American Society of Mechanical Engineers.

objective is to develop a material-testing machine that can achieve high accelerations (up to 50g) and generate velocity-steps from quasi-static slip-rates (as low as 1 $mm.s^{-1}$) to seismic slip rates (up to 1 $m.s^{-1}$) in a few millimeters of slip under loads as high as 500 kN. Figure 3.1 illustrates a velocity-step from V_1 to V_2. Generally, the actual velocity response of a mechanical system deviates from the target velocity-step; e.g., it exhibits an overshoot and a delay. Here, we define d_r as the distance in which 80% of the velocity change (ΔV) occurs. Also, the time duration associated with d_r is defined as rise time, t_r. For the desired sliding friction tests, V_1 and V_2 are respectively in a range of 1-10 ($mm.s^{-1}$) and 100-1000 ($mm.s^{-1}$), and d_r is ideally < 2 mm. After the step, velocity needs to be maintained constant with less than 10% error from the target velocity. In this research work, the prototype of a testing-machine (HSB) incorporating a hydro-pneumatic high-speed loading system has been developed that can achieve these capabilities and operate in triaxial and biaxial double-direct shear sample configurations. As indicated above, biaxial and triaxial configurations (Figure 1.1) have been successfully used to test friction at low sliding rates [*Dieterich*, 1978; *Marone*, 1998; *Mair and Marone*, 1999]. The present loading system extends the application of those two configurations to high slip-rates and accelerations.

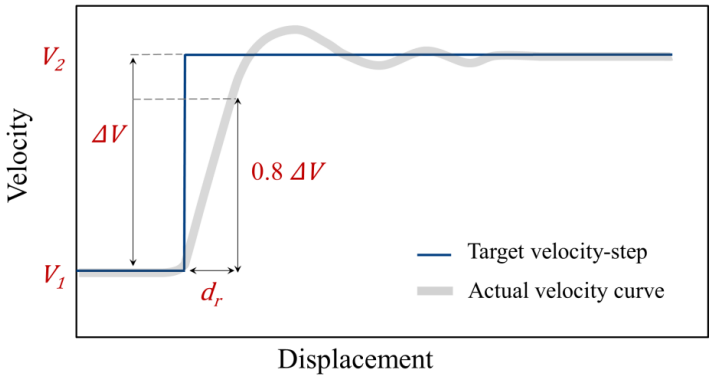

Figure 3.1: Target velocity-step and a typical velocity response. Once the sliding rate is stepped to the target value, velocity should maintain constant over the high-speed section of the stroke (2 – 4 cm) with less than 10% error from the target velocity-step.

3. 3 Design challenges

Achieving the desired step-wise velocity paths under loads up to 0.5 MN requires a loading system with a very short rise time; i.e., t_r should be only about a few milliseconds. It can be seen in Figure 3.1 that at a given acceleration, d_r decreases as ΔV reduces. Accordingly, at sliding rates < 10 mm.s^{-1}, servo-hydraulic systems can achieve velocity-steps quite well (d_r is short) using displacement feedback control. However, at high sliding rates (such as our application), the finite rise time of a servo-hydraulic (partly caused by response time of actuators and time delays of feedback control systems [*Schlotter and Plummer, 2011*]) would result in a major part of the stroke being used to achieve the target velocity[11]. In addition, if d_r is higher than a few millimeters, the instantaneous direct effect of sliding rate on the transient friction cannot be fully

[11] $d_r = t_r \times$ average velocity, and at seismic slip rates, both t_r and average velocity are higher than those at quasi-static sliding rates. Therefore, d_r can be several orders of magnitude larger than that at quasi-static sliding rates if the conventional hydraulic servo-system is used.

investigated. In other words, a slow change in sliding rate allows other parameters (such as slip distance) to interfere the independent effect of velocity on friction, which makes it difficult to understand the velocity-dependence of friction. This is one of the main limitations of most of the existing rotary machines used to study sliding friction due to the limitations on the acceleration of electrical motors. As a result, in the rotary configuration, seismic sliding rates generally can be achieved only after several cm of slip [*Ma et al., 2014*]. Such a long slip distance makes it challenging to decouple and distinguish the effects of sliding rate and slip distance on the transient friction [*Ma et al*., 2014].

In some existing material-testing machines working at high deformation rates, open-loop control or iterative strategies have been employed to control the deformation rate [*Yang et al*., 2014; *Schlotter and Plummer*, 2011]. In such machines, the hydraulic loading rod is activated to reach the desired velocity prior to engaging with the specimen and initiating deformation. If there are no open-loop controls, deformation rate would decrease after engaging the specimen, as it exerts a resistive force that is generally large compared to the driving force. Iterative strategies can be implemented to minimize the variations of velocity from the target deformation rate. However, impact-type engagement of the loading rod and the specimen still generates undesirable stress waves in the loading column that can cause ringing, signal distortion, and even can affect the mechanical behavior and response of the test samples. Several methods have been proposed in the literature to reduce ringing artifacts caused by impact type loading of such systems (e.g., employing a soft material between the specimen gripper and the

loading rod [*Bardenheier and Rogers*, 2003], using strain-gauges instead of load-cells, and optimizing the geometry of the specimen [*Yang et al*., 2014]). Yet, it remains difficult to achieve a constant target velocity over the stroke under high loads (> 100 kN) by using open-loop control strategies. These methods are more efficient for materials that do not show significant velocity-dependent behavior (e.g. 10% variation in deformation rate does not induce large strength changes). Friction in rock can be sensitive to velocity variations, and impact-type loading may result in ringing or may trigger undesirable stick-slip events.

The other technical challenge of attaining the desired velocity-step capability arises due to the load capacity requirements of the desired testing machine. The apparatus should be able to drive decimeter-sized samples under high normal stresses (up to 100 MPa). Friction force between the sliding sample and stationary side blocks of rock under such normal stresses (in double direct configuration) can be as high as 0.5 MN. Thus the load column must contain components with mass of tens of kilograms to have sufficiently high strength and stiffness. Therefore, for the required high accelerations (50g), the inertial forces will be large as well (tens of kN). Large inertial forces without closed-loop load control can lead to ringing and poor performance [*Yang et al*., 2014]. Moreover, the friction force of the sliding rock sample may undergo a dramatic decay (i.e. dynamic weakening) over the stroke, and such a behavior can greatly intensify the velocity overshoot and vibrations in the load column. Hence, the testing machine should be designed accordingly and be fully analyzed to verify if the target velocity-step can be achieved under the extreme conditions of testing.

3. 4 Prototype system

The HSB incorporates a loading system that is fully engaged with the test-sample throughout the entire loading cycle to avoid impact-type loading while maintaining the ability to achieve high accelerations at high loads. The HSB consists of two loading systems (horizontal and vertical loading systems). As shown in Figure 3.2 and 3.3, the horizontal loading system employs a stiff frame equipped with a hydraulic loading system to compress the sample assembly statically in the horizontal direction. Within the horizontal frame, the middle rock-block of the double-direct shear configuration is sandwiched between the stationary side rock-blocks under the target normal force (up to ~0.5 MN). The hydraulic cylinder is connected to a pneumatic accumulator so that lateral deformation of the sample assembly does not change the normal force[12]. The horizontal loading frame is instrumented with a strain-gauge load-cell to measure the normal force. After the sample is loaded to the desired normal stress (up to 100 MPa), the vertical loading system is engaged to slide the middle block of the sample. For the vertical loading system, the prototype HSB uses a hydro-pneumatic actuator originally designed to conduct fracture experiments at intermediate strain rates (10^{-2} –10^{2} s^{-1}) [*Green et al*., 1968; *Logan and Handin*, 1970]. The hydro-pneumatic High-Speed Loading System (HSLS) and vertical frame are shown in Figure 3.2. The friction force and sliding velocity of the sample can be recorded during the experiments and the dependency of friction on velocity can be studied directly. In order to use the machine in

[12] The rock sample may experience dilatation or compaction during slip.

the triaxial configuration, the horizontal frame can be removed and a pressure vessel is used to provide the lateral load (confining pressure as shown in Figure 1.1c).

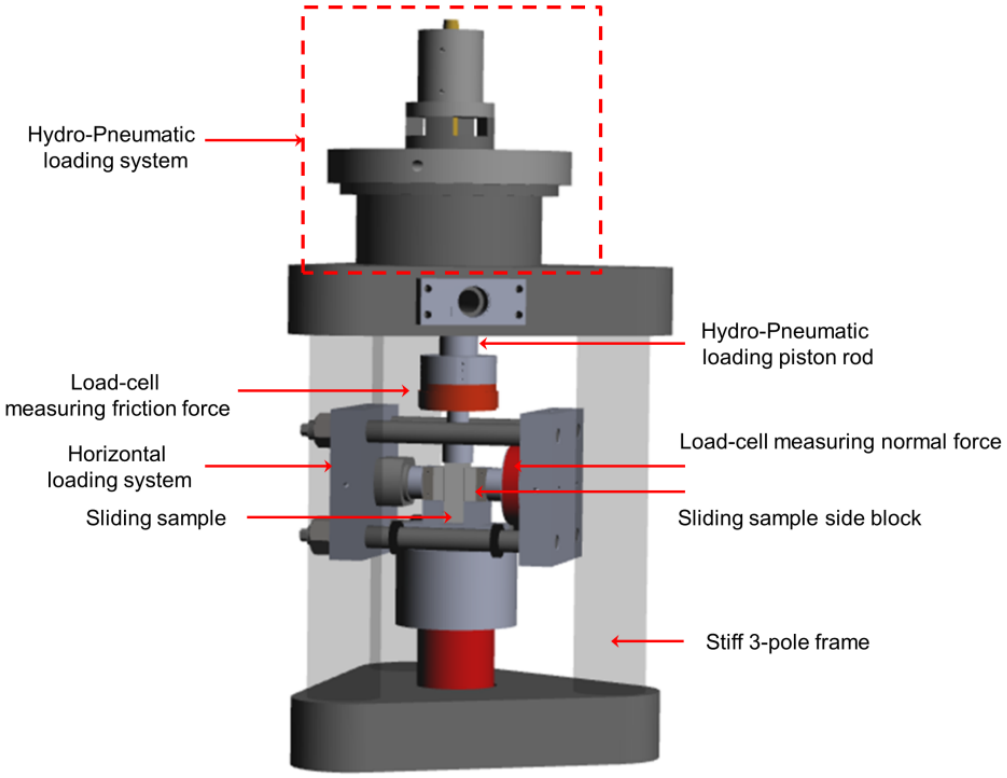

Figure 3.2: The prototype of the HSB in double direct configuration. The biaxial testing machine employs a stationary horizontal loading system, which statically compresses the sample laterally. For the vertical loading system, a hydro-pneumatic actuator is employed to generate the desired velocity-steps. Load cells are shown in red. Two load cells are employed along the vertical axis loading column; the lower one is stationary while the upper one moves with the the piston.

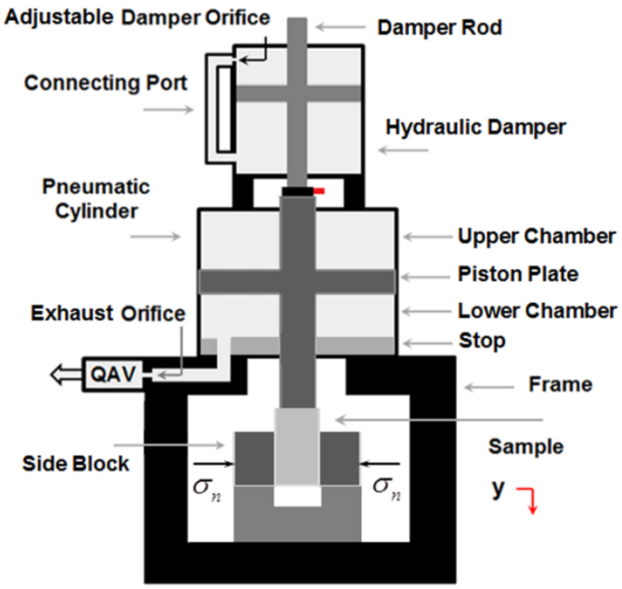

Figure 3.3: Schematic drawing of the HSB in double-direct configuration.

3. 5 Description of the high-speed hydro-pneumatic loading system

The pneumatic actuator of the HSLS employs a moving piston plate to separate the upper and lower chambers of the cylinder. Both chambers of the cylinder are initially pressurized with gas (Figure 3.3). The piston plate is 32 cm in diameter and the initial pressure of gas, P_0, can be increased to 20 MPa to achieve a load capacity of 1.5 MN. The pneumatic cylinder is fired by opening the large-diameter exhaust port of the lower gas chamber using a Quick Acting Valve (QAV). The QAV is triggered using a solenoid valve and is designed to open the 5 cm exhaust port rapidly. The reduction in gas pressure in the lower chamber creates a net force on the pneumatic piston plate that accelerates and displaces the piston rod downwards. The exhaust port employs exchangeable orifice plates with different orifice size to pre-set the mass flow rate of the

exhausting gas. For the friction tests, the experiment can begin by opening a small auxiliary vent to reduce the gas pressure in the lower chamber gradually until the sample initiates quasi-static frictional sliding at 1 $mm.s^{-1}$, and then the QAV is activated to make the jump in velocity for achieving typical seismic sliding-rates.

The pneumatic loading-system generates high accelerations during velocity steps to reach the target velocity within a few milliseconds; however, the acceleration must decrease to zero so that velocity is maintained constant after the velocity-step. A hydraulic damper is connected to the upper end of the pneumatic piston rod to generate a resistive force that increases with velocity. The damping coefficient, C_d, can be pre-adjusted before each experiment by changing the orifice size at the connecting port of the damper (Figure 3.3) so that the resistive force of the damper at the target velocity cancels out the net driving force of the system and a constant velocity can be achieved over the stroke. In absence of feedback control, the hydro-pneumatic actuator employs three adjustable mechanical settings, referred to as Preset Passive-Control Variables (PPCV), that dictate the actuator response. Two of the PPCVs include adjustable orifices that are set before each experiment, but cannot be varied during the experiment, to control the actuator behavior (C_d and A_t[13]). The other PPCV is the initial pressure in the pneumatic cylinder, P_0. The original hydro-pneumatic actuator was not designed for friction experiments, or used for generating velocity-steps [*Green et al*., 1968; *Logan and Handin*, 1970], so we assess the viability of the actuator for conducting velocity-stepping friction tests on rock. To achieve the desired velocity-step, fine selection of the

[13] A_t is the area size of the orifice used in the exhaust port of the pneumatic cylinder

PPCV is necessary. In the following sections, an analytical model is presented to analyze the effect of the PPCV on the system response and thus obtain optimum values for achieving a desired velocity-step. It will be shown how the PPCV can be adjusted to achieve a velocity-step in friction experiments for a wide range of test-sample responses.

3. 6 Model formulation of the HSLS assuming rigid-body motion

In this section, the equation of motion for the HSLS has been derived assuming rigid body motion of the moving piston [*Saber et al.*, 2014, 2016]:

$$(P_U - P_L)A_p - F_s - F_d = m_t \ddot{y} \tag{3.1}$$

where, m_t is the total mass of the moving parts, $\ddot{y}$ denotes the acceleration of the piston (y is shown in Figure 3.3), P_U and P_L are the pressures in the upper and lower chambers of the pneumatic cylinder, respectively (Figure 3.4), A_p is the effective area of the pneumatic piston plate, F_s is the resistive force of the sample, and F_d is the damping force estimated by $F_d = C_d \dot{y}^2$ (note: all the variables used in the model analysis are defined in the Nomenclature).

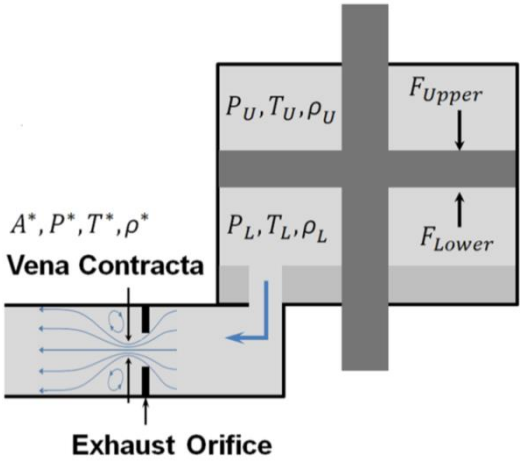

Figure 3.4: Schematic drawing of the pneumatic cylinder and vena contracta.

In order to solve Equation 3.1, P_U and P_L should be obtained as a function of time. Since the blow-down process is very quick, it can be assumed that no heat transfer takes place between the pneumatic cylinder and the surrounding during the high-speed slip, and based on isentropic expansion relations [*Rathakrishnan,* 2010], the pressure in the upper chamber of the pneumatic cylinder (P_U) can be obtained as follows:

$$P_U = P_0 \left(\frac{V_{U0}}{V_U} \right)^{\gamma} \tag{3.2}$$

where, γ is specific heat ratio of gas. The total volume of the pneumatic cylinder is constant, so the volume in the upper chamber is given by:

$$V_U = V_{U0} + V_{L0} - V_L \tag{3.3}$$

where, V_{U0} and V_{L0} are the initial volume of the upper and lower pneumatic chambers respectively, and:

$$V_L = A_p\left(h_L - y(t)\right) \tag{3.4}$$

where h_L is the initial height of the lower chamber of the pneumatic cylinder.

Substituting Equations 3.3-3.4 in Equation 3.2, P_U can be obtained as follows:

$$P_U = P_0\left(\frac{V_{U0}}{V_{U0}+V_{L0}-A_p\left(h_L - y(t)\right)}\right)^{\gamma} \tag{3.5}$$

The pressure in the lower chamber, P_L, should be found as a function of time. Using the ideal gas law, the mass of gas in the chamber can be determined:

$$m_g = A_p\left(h_L - y(t)\right)\frac{P_L}{RT_L} \tag{3.6}$$

Isentropic flow relations can be used to relate temperature and pressure [*Rathakrishnan,* 2010] as follows:

$$T_L = T_{L0}\left(\frac{P_L}{P_0}\right)^{\frac{\gamma-1}{\gamma}} \tag{3.7}$$

Substituting Equation 3.7 in Equation 3.6, the ideal gas law can be re-written as:

$$m_g = \frac{A_p P_0^{\left(\frac{\gamma-1}{\gamma}\right)}}{RT_{L0}}\left(h_L - y(t)\right)P_L^{\frac{1}{\gamma}} \tag{3.8}$$

By differentiating Equation 3.8, the mass flow-rate of the exhausting gas can be obtained as follows:

$$\dot{m}_g = \frac{A_P P_0^{\frac{\gamma-1}{\gamma}}}{RT_0}\left(\frac{\left(h_L - y(t)\right)}{\gamma}P_L^{\frac{1-\gamma}{\gamma}}\frac{dP_L}{dt} - P_L^{\frac{1}{\gamma}}\frac{dy}{dt}\right) \tag{3.9}$$

Based on mass conservation (i.e. continuity), the rate of change in mass inside the lower side of the pneumatic cylinder is equal to the mass flow rate of the exhausting gas:

$$\dot{m}_g = -\rho^* A^* v^* \tag{3.10}$$

where,

$$\rho^* = \rho_L\left(\frac{2}{\gamma+1}\right)^{\frac{1}{\gamma-1}} \tag{3.11}$$

$$\rho_L = \rho_0\left(\frac{P_L}{P_0}\right)^{\frac{1}{\gamma}} \tag{3.12}$$

In Equation 3.10, A^* is the area of vena contracta, which is the narrowest point of the fluid stream. Vena contracta forms at downstream of the orifice because of the compressibility effects and the flow contraction through the orifice. As illustrated in

Figure 3.4, when fluid approaches the orifice, flow streamlines converge toward it. Since an abrupt change in the direction of stream-lines is not possible, the stream-lines continue to converge after the orifice for a short distance where all stream-lines become parallel (i.e. vena contracta), before they diverge. A^* can be obtained as follows:

$$A^* = C_0 A_t \tag{3.13}$$

C_0 is the discharge coefficient, which has a value smaller than 1 (i.e., $C_0 = \dot{m}_{actual}/\dot{m}_{ideal}$). The values for C_0 are listed in the literature based on the flow properties and orifice geometry [*Cunningham*, 1951; *Ward-Smith*, 1979]. C_0 value can be as high as 1 when the downstream pressure is much lower than the P_L [*Baukal*, 2010]. Under this condition, the gas flowing through the orifice will be choked and the Mach number ($M = v_{fluid}/v_{sound}$) is equal to 1 at the vena contracta [*Rathakrishnan*, 2010]. This holds when the pressure ratio between the downstream and upstream sides is lower than $\left(\frac{2}{\gamma+1}\right)^{\gamma/\gamma-1}$ [*Rathakrishnan*, 2010]. This pressure ratio is about 0.5 for general types of gas. So, the gas velocity will be equal to sound speed as long as P_L is equal or greater than twice the downstream pressure, P_{ds}. For the HSLS, $P_0 >> 2P_{ds}$ so v^* in Equation 3.10 is equal to the speed of sound, which can be obtained as follows [*Rathakrishnan*, 2010]:

$$v^* = \sqrt{\gamma R T^*} \tag{3.14}$$

where,

$$T^* = \frac{2}{\gamma+1} T_L \tag{3.15}$$

$$T_L = T_0 \left(\frac{P_L}{P_0} \right)^{\frac{\gamma-1}{\gamma}} \tag{3.16}$$

By substituting Equations 3.11-3.12 and 3.14-3.16 into Equation 3.6, Equation 3.10 can be re-written as follows:

$$\dot{m}_g = -A^* \rho_0 \sqrt{\gamma R T_0} \left(\frac{2}{\gamma+1} \right)^{\frac{\gamma+1}{2(\gamma-1)}} \left(\frac{P_L}{P_0} \right)^{\frac{\gamma+1}{2\gamma}} \tag{3.17}$$

By equating Equations 3.9 and 3.17, the following equation can be obtained:

$$\frac{A_P P_0^{\frac{\gamma-1}{\gamma}}}{R T_0} \left(\frac{(h_L - y(t))}{\gamma} P_L^{\frac{1-\gamma}{\gamma}} \frac{dP_L}{dt} - P_L^{\frac{1}{\gamma}} \frac{dy}{dt} \right) - A^* \rho_0 \sqrt{\gamma R T_0} \left(\frac{2}{\gamma+1} \right)^{\frac{\gamma+1}{2(\gamma-1)}} \left(\frac{P_L}{P_0} \right)^{\frac{\gamma+1}{2\gamma}} = 0 \tag{3.18}$$

In summary, Equations 3.1, 3.5 and 3.18 are the governing equations of motion for the HSLS.

3. 7 Numerical simulation of HSLS dynamic response

To accurately model the dynamic response of the HSLS during a velocity-step experiment, specification of the resistive force of the test-sample, F_s should be known. Interfacial friction experiments on rock using a rotary shear apparatus typically show a marked drop in resistive force after initiation of high-speed sliding that is often modeled

as an exponential decay[14] [*Hirose and Shimamoto*, 2005; *Di Toro et al*., 2011]. For such behavior, the transient weakening of the sample can be defined using three parameters: 1) initial quasi-static sliding friction force (F_{s0}) upon initiation of high-speed sliding, 2) relative magnitude of the force drop during high-speed weakening ($\Delta F_s/F_{s0}$), 3) a characteristic displacement (D_c) in which 90% of the force-drop (ΔF_s) is achieved (as shown in Figure 3.5). Using these 3 parameters, F_s can be written as follows:

$$F_s = F_{s0} - \Delta F_s \left(1 - \exp\left(\ln(0.1)\frac{y}{D_c}\right)\right) \tag{3.19}$$

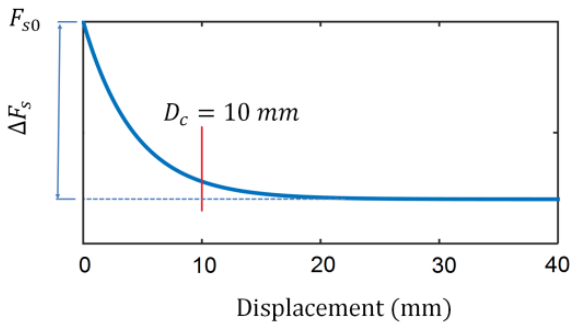

Figure 3.5: Friction force-drop modeled with an exponential decay using the 3 characteristic parameters identified in the plot.

In order to analyze the machine-sample interaction, a parametric study was carried out. For this purpose, Equation 3.19 was used and the magnitudes of the parameters F_{s0}, ΔF_s, and D_c were varied to represent the range of possible friction

[14] The exponential decay is also consistent with evolution laws in the rate- and state-variable constitutive equations [*Dieterich*, 1978].

behaviors expected for velocity-steps to seismic sliding-rates. For example, dynamic weakening at seismic slip-rates and high normal stress (>10 MPa) can be represented by small D_c (1-20 mm) and high $\Delta F_s/F_{s0}$ (10-70%). An example simulation of the HSLS dynamics for a test-sample response characterized by F_{s0} = 200 kN, D_c = 5 mm and $\Delta F_s/F_{s0}$ = 10% is presented in Figure 3.6; with PPCV values of P_0 = 9.4 MPa, A_t = 2.68 cm^2, and C_d = 52 $kN.s^2.m^{-2}$.

For the example case, the forces acting on the pneumatic piston are depicted as a function of time (QAV is opened at t= 0) in Figure 3.6b. The initial pressures in both chambers of the pneumatic cylinder are equal. The forces include those generated by the gas in the upper chamber (F_{upper}) and the lower chamber of the pneumatic cylinder (F_{lower}) and the resistive force of the damper. When the QAV is activated, the gas from the lower chamber exits at the speed of sound and P_L decreases quickly. However, during the first stage, Stage 1, the differential force $(P_U - P_L)A_p$ is less than the resistive force of the sample, and thus the rod is not displaced and P_U remains constant. For this specific example, Stage 2 starts at 5 milliseconds when the net downward force from the HSLS equals the sample force. During Stage 2 the sample slides, the piston moves downward, and the pressure in the upper chamber decreases as a result of volume expansion. In this example, the QAV was activated when the piston was stationary. The lower chamber of the pneumatic cylinder has an auxiliary exhaust that can vent gas through a small orifice in order to achieve steady-state sliding at 1 $mm.s^{-1}$ for a few mm before the velocity-step. In that case, the reference point (in terms of time, displacement, velocity and pressure) is set at the initiation of the velocity-step. During quasi-static

sliding (at 1 mm.s^{-1}) friction force is generally constant, $F_s = F_{s0}$, and F_s is assumed to undergo an exponential decay upon the initiation of high-speed slip at $t = 0$ which corresponds to the instant that the QAV operates.

a)

b)

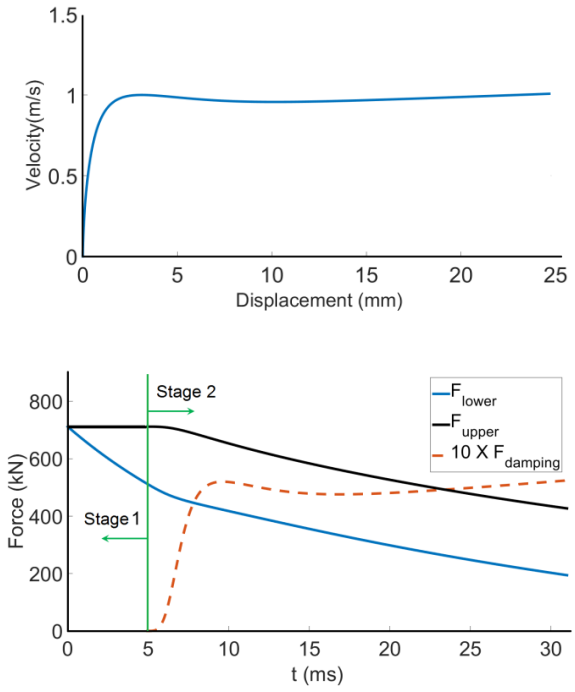

Figure 3.6: Model simulation of a high-speed friction experiment. a) Velocity of the piston as a function of displacement, b) forces exerted to the piston from the lower chamber, upper chamber and the damper versus time. (F_{s0} = 200 kN, D_c = 5 mm and $\Delta F_s/F_{s0}$ = 10%).

3. 8 Effects of different parameters on the velocity response of the HSLS

In the previous section, the response of the loading system for a specific case was presented. The response could follow the desired pattern with a very small error. However, it is not always possible to achieve the desired response. The ability to generate the desired velocity-step depends on both sample behavior and loading system characteristics. To explore this ability, in this section, effects of different parameters on the system behavior are investigated.

Figure 3.7 illustrates the response for three different values of F_{s0} (100 kN, 400 kN, 700 kN) while ΔF_s is set to zero so that the effect of the F_{s0} is explored more clearly. In all cases, the initial pressure (P_0) is equal to 15 MPa and C_d = 52 kN.s^2.m^{-2}. An ideal velocity curve can be achieved when F_{s0}=400 kN. However, velocity drops drastically for F_{s0}=700 kN. As the piston moves downward, pressure decreases in the upper chamber of the pneumatic cylinder due to volume expansion. For this reason, in this case (F_{s0}=700 kN), the driving force of the loading system becomes smaller than the resistive forces after 5 mm of displacement, and the pneumatic piston decelerates. Moreover, in this case, a large orifice size is necessary to achieve 1 m.s^{-1}, otherwise the maximum velocity will be too low when P_0 =15 MPa and F_{s0}= 700 kN. On the other hand, if the initial pressure is too high relative to F_{s0}, velocity increases slightly and deviates from the ideal curve. This can be seen in Figure 3.7 when F_{s0} = 100 kN. However, ideal responses can be achieved for both of the cases of F_{s0} equal to 100 and 700 kN by setting P_0 to 5 and 25 MPa, respectively. In conclusion, the maximum allowable pressure

determined by the design of the pneumatic cylinder must be sufficiently high for large values of F_{s0}.

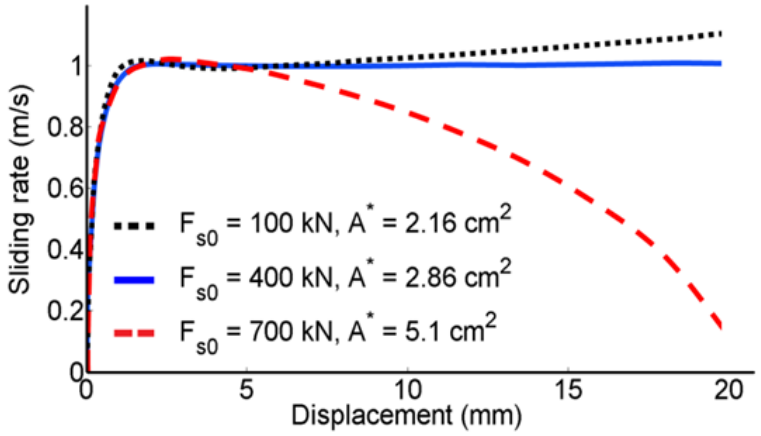

Figure 3.7: Velocity response of the pneumatic piston versus displacement. Velocity curves are shown for different values of F_{s0} when P_{01} = 15 MPa.

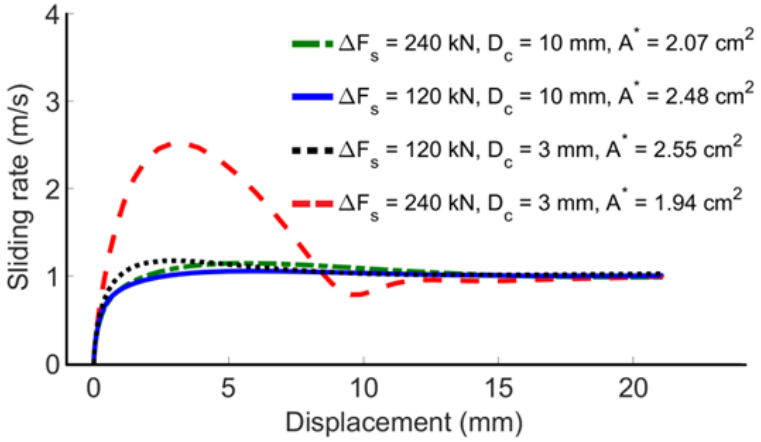

Figure 3.8: The effect of F_{s0} on velocity response of the pneumatic piston versus displacement for different weakening behaviors of a sample. To consider different weakening behaviors, ΔF_s and D_c are varied when F_{s0} = 400 kN, F_{dc} = 150 kN, and P_0 = 15MPa.

The other parameters that influence the velocity response are ΔF_s and D_c, which describe the weakening behavior of the sample. The main design parameter that controls the response during sample weakening is load capacity of the damper (F_{dc}). Figure 3.8 illustrates the velocity response of the system for 4 cases of sample weakening. In general, higher F_{dc} is required for samples with larger ΔF_s or smaller D_c, otherwise the response will exhibit an overshoot. As shown in Figure 3.8, for ΔF_s= 120 kN and D_c= 10 mm, a good response can be achieved when F_{dc}= 150 kN. The response is still acceptable when either D_c is decreased to 3 mm or ΔF_s is increased to 240 kN, which means that F_{dc} is high enough to provide the required damping force. However, if D_c is 3 mm and ΔF_s is 240 kN, the damper cannot provide enough resisting force and the response will depict a large overshoot as shown in Figure 3.8. Therefore, when D_c is small and ΔF_s is large, F_{dc} should be high enough in order to achieve the desired velocity-step.

3. 9 Workspace of the apparatus

As discussed in the previous section, control parameters can be adjusted for different sample behaviors to achieve the desired response. However, in practice, there are several design constraints that restrict these parameters. The constraints are the maximum allowable pressure in the pneumatic cylinder and the load capacity of the damper which impose limits on P_0 and C_d. The design constraint on A^* does not produce any restriction, in other words, the exhaust size can be built even larger than required. So, in this study, only restrictions introduced by maximum allowable pressure (P_{max}) and damping load capacity (F_{dc}) are considered and presented.

For any given P_{max} and F_{dc}, one can find in what range of F_{s0}, ΔF_s and D_c the apparatus is able to perform tests and achieve the desired velocity-step response. This range defines the workspace of the apparatus. In each case of the parametric search done for obtaining the workspace, a combination of sample parameters (F_{s0}, ΔF_s, D_c) were considered. For each of these combinations, a search should be done over different values of allowable PPCVs (P_0, A^*, C_d) to determine if there is at least one set of PPCVs that generate the desired velocity path. If such a set is identified, this point belongs to workspace. For this purpose, at each point of PPCV space, the velocity response is compared to the ideal velocity-step curve and the associated error is found as shown in Figure 3.9; the relative error is calculated as the area bounded between the ideal velocity curve and the actual curve divided by the total area under the ideal curve. In this study, the response is considered acceptable if the overall relative error is less than 10% for a 2 cm stroke. After completion of the search for the first set of (F_{s0}, ΔF_s, D_c), another search is started for the next set. For the next set of (F_{s0}, ΔF_s, D_c), we start the search for PPCV from a small neighborhood of (P_{01}, A^*, C_d) found for the previous set of sample properties. Because points of sample parameter space are close to each other, the new set of PPCV should not be much different. In this way, the PPCV can be found with smaller amount of search and the computational cost decreases considerably.

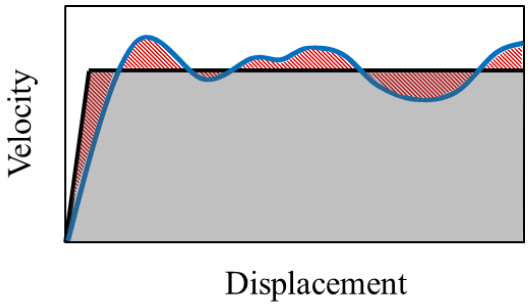

Figure 3.9: Ideal velocity pattern versus the actual velocity as a function of displacement. The red region denotes the difference between the curves and error is defined as the ratio between this area and the gray area under the ideal curve.

Figure 3.10 illustrate the results of the search done for four different combinations of F_{dc} and P_{max}. In each of a-d figures, workspace is obtained for three values of D_c. Workspace is the area to the left of curves. For each D_c, different combinations of F_s and $\Delta F_s/F_{s0}$ are considered where $0 \leq F_s \leq 1.5$ MN and $0 \leq \Delta F_s/F_{s0} \leq 0.9$. A non-dimensional parameter ($\Delta F_s/F_{s0}$) has been used for performing the search because the limit of ΔF_s changes with magnitude of F_s. It can be inferred from Figure 3.10 that two types of boundaries define workspace. A schematic diagram of these two boundaries and workspace (for a specific D_c) is shown in Figure 3.11. The first boundary defines the upper side of the curves which depends mainly on the damping capacity F_{dc}. For the area to the right of this boundary, overshoot produces errors larger than desired (similar to Figure 3.8, when ΔF_s = 240 kN, D_c = 3 mm). The second boundary defines the lower part of curves which mostly depends on P_{max}. The area to the right of this boundary corresponds to conditions at which P_{max} is not large enough relative to F_{s0}. In these cases, the piston velocity drops considerably (similar to Figure 3.7, when F_{s0} = 700 kN).

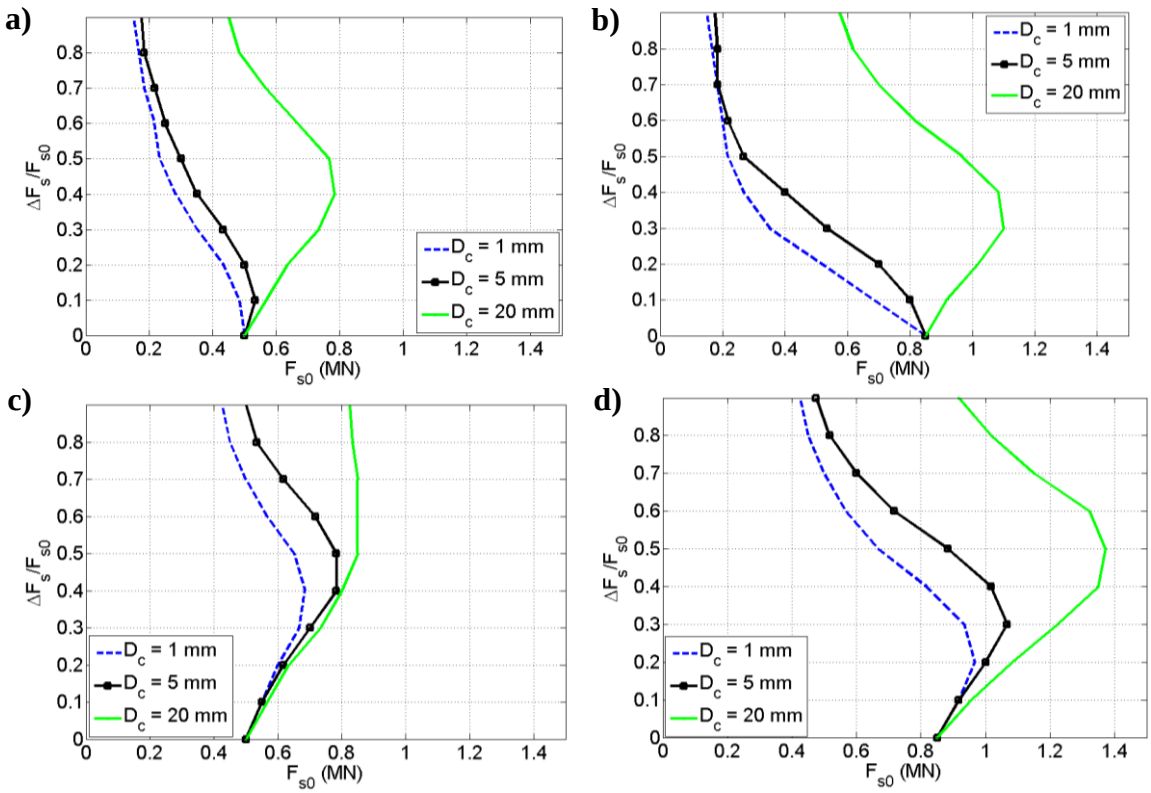

Figure 3.10: Boundaries of workspace (workspace is the region on the left of the lines). a) F_{dc} = 100 kN, P_{max} = 12 MPa, b) F_{dc} = 100 kN, P_{max}=20 MPa, c) F_{dc}= 300 kN, P_{max} = 12 MPa, d) F_{dc} = 300 kN, P_{max} = 20 MPa.

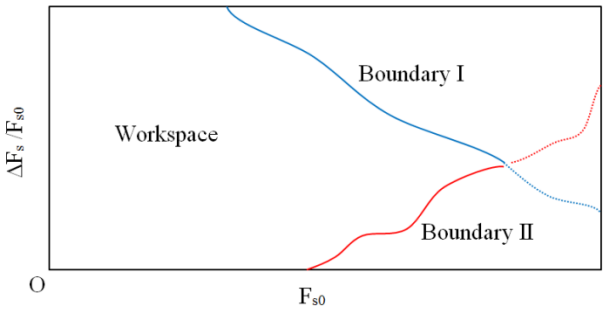

Figure 3.11: Schematic diagram of the workspace.

Figure 3.10 (a-d) implies that Boundary I moves to the right and the workspace expands as D_c increases. D_c increase means that ΔF_s occurs over a longer displacement and sample weakening is less abrupt. The other parameter that can move Boundary I is F_{dc}. In nutshell, increasing the damping capacity enlarges workspace by moving Boundary I to the right. Boundary II is mostly a function of P_{max}. Increasing P_{max} results in an expansion of the workspace by moving Boundary II to the right. P_{max} can move Boundary I as well when D_c is large enough. For example, when D_c is 20 mm, increasing P_{max} moves Boundary II to the right considerably. The reason is that the existence of higher pressure in the pneumatic cylinder gives the system more flexibility of adjustment to disturbances such as sample weakening. However, this is not the case when D_c is very small. For example, when D_c is 1 mm, increasing P_{max} does not move Boundary II significantly. That is because for small D_c, the sample weakening occurs so abruptly that even a higher pressure cannot make a significant difference.

3. 10 Design requirements

In order to find design requirements, minimum values of P_{max} and F_{dc} should be obtained such that workspace covers the range of expected sample behaviors. For our application, the apparatus needs to perform experiments on samples with F_{s0} (0-500 kN), $\Delta F_s/F_{s0}$ (0-70%) and D_c (1-20 mm). This range of F_{s0} means that large values of normal stress as high as 100 MPa can be achieved during friction experiments while samples have a contact dimensions of 5×7.5 cm^2. For this purpose, the maximum load capability of the damper should be 300 kN and the pneumatic cylinder must be able to hold pressures up to 12 MPa so that the workspace covers the expected range as shown in

Figure 3.10c. Based on these results, the design of the HSLS has been modified for the ultimate HSB machine to achieve the desired velocity-steps for the full range of rock-sample behaviors expected.

CHAPTER IV

EXPERIMENTAL CHARACTERIZATION OF THE HSB BEHAVIOR AND VALIDATION OF DYNAMICS AND VIBRATIONS MODEL[15]

4. 1 Introduction

Numerous machines with hydro-pneumatic loading-systems for conducting material-testing experiments at intermediate strain rates (10^{-1}-10^{2} s^{-1}), have been presented in the literature; however, stiffness analysis and vibrations of these systems have not been well-documented [*Senseny et al*., 1979; *Lindholm and Yeakley*, 1967; *Tarigopula et al*., 2009]. In general, the rods of the load column and fluid in the hydraulic damper may be assumed rigid and incompressible in comparison with the compressible gas in the pneumatic cylinder; however, our results show that under impulse-type loading (that can be induced by rock-sample weakening) the compressibility of the damping fluid and finite stiffness of the loading column can lead to vibrations of the loading rod in contact with the test-specimen. Large-amplitude vibrations appear as an overshoot in velocity-response followed by oscillations around the target velocity; the oscillations are real and not simply a reflection of measurement

[15] Part of the data reported in this chapter is reprinted with permission from "Development of a Material-Testing Machine for Study of Friction: Experimental Analysis of Machine Dynamics and Friction of Rock." by O. Saber, F. M. Chester, and J. L. Alvarado, 2016, Experimental Mechanics 56.5 (2016): 813-831, Copyright 2016 by Society for Experimental Mechanics.

distortion. Therefore, the oscillations have physical influence on the mechanical behavior of the sample and cannot be removed by improving measurement methods or signal filtration. In this chapter, an analytical model with three Degrees of Freedom (DoF) is presented to study dynamics and vibrations of the machine employing the prototype HSLS. In addition, the prototype apparatus is instrumented with a high-speed DAQ, and a set of experiments have been designed and conducted to characterize the machine, validate and calibrate the mathematical model, and evaluate the performance of the machine for conducting velocity-step experiments. Finally, a modified model is used to optimize the design of the hydro-pneumatic actuator for the ultimate HSB machine, including the reduction of unwanted vibrations.

4. 2 Instrumentation of the HSB

In Chapter III, the ability of the prototype loading system to generate the desired velocity-step was evaluated using an analytical model, but the analytical model must be validated by direct testing. To this end, the High-Speed Loading System (HSLS) is equipped with 8 sensors and it has been tested in uniaxial and biaxial configurations to characterize the high-speed system response. The location and type of sensors are specified in Table 4.1 and Figure 4.1. Pressure transducers have been installed in each chamber of the hydraulic damper cylinder (#2 and 3) and are used to determine the damping force by multiplying the effective area of the damper plate by the differential pressure between the two chambers. In addition, a load-cell is installed between the damper rod and the pneumatic piston rod to allow a direct measure of the resistive force of the damper (#4). By comparing this force to the one obtained from the pressure data

(using #2 and 3), one can find the friction force generated by the o-ring seals of the damper rod. Also, pressure transducers have been installed in each chamber of the pneumatic cylinder. The change in pressure recorded by the two sensors (#5 and 6) can be used to characterize the flow model developed in Chapter III. An accelerometer (#1) and a laser displacement transducer (#7) are used independently to determine the velocity of the rod at the sample, by integrating acceleration and differentiating displacement with respect to time. To record the resistive force of the sample, a load cell has been placed under the specimen (#8). In the double-direct configuration, load-cells are also employed in the vertical axis above the sample and in the horizontal axis. The load-cell in the horizontal axis measures the normal stress at the contact interface of sample and side blocks (Figure 4.2).

Table 4.1: List of the transducers used for system identification

No.	Transducer	Range of measurement	Frequency range	Accuracy
1	Accelerometer	±200g	0 – 10 kHz	±1.5% of span
2	Pressure transducer in the upper chamber of the damper	0 – 35 MPa	0 – 54 kHz	±0.25% of span
3	Pressure transducer in the lower chamber of the damper	0 – 35 MPa	0 – 54 kHz	±0.25% of span
4	Load cell between damper and the pneumatic cylinder	0 – 100 kN	0 – 10 kHz	±0.25% of span
5	Pressure transducer in the upper chamber of the pneumatic cylinder	0 – 35 MPa	0 – 54 kHz	±0.25% of span
6	Pressure transducer in the lower chamber of the pneumatic cylinder	0 – 35 MPa	0 – 54 kHz	±0.25% of span
7	Laser displacement transducer	0 – 5 cm	0 – 10 kHz	±0.03% of span
8	Load cell under the sample	0 – 500 kN	0 – 15 kHz	±0.25% of span

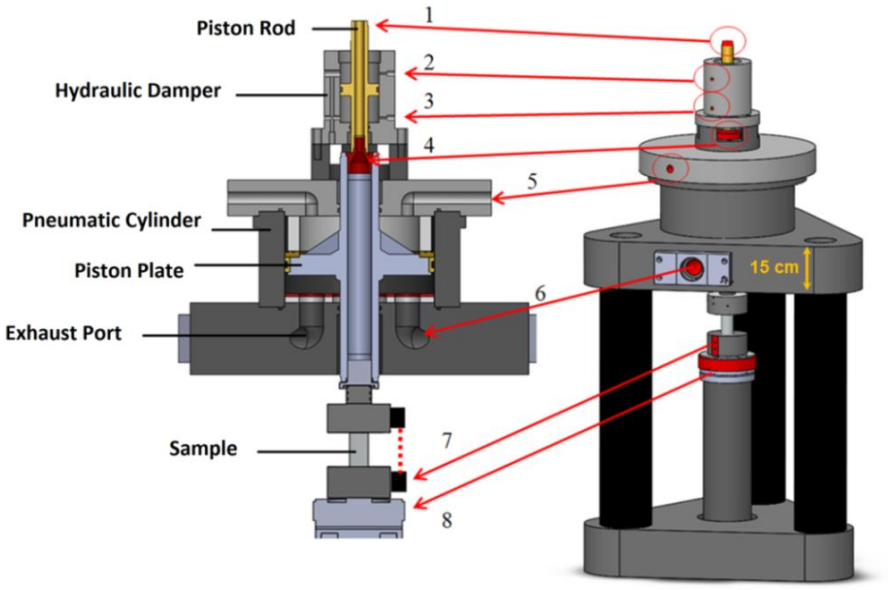

Figure 4.1: The prototype high speed loading system. The system is equipped with 8 sensors in uniaxial configuration for characterization and model validation; each number corresponds to a transducer as listed in Table 4.1 #1: accelerometer, #2, 3, 5, 6: pressure transducers, #4, 8: load-cells, #7: laser displacement transducer.

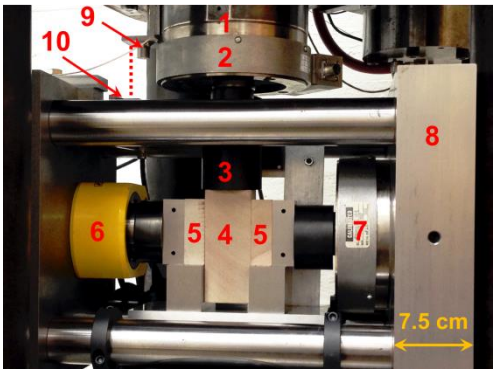

Figure 4.2: The experimental setup for conducting sliding friction experiments in the double-direct shear configuration. #1: adapter between the pneumatic piston rod and the moving load-cell, #2: moving load-cell, #3: adapter between load-cell and the sliding rock sample, #4 sliding rock sample (Tennessee sandstone), #5 stationary side blocks, #6: hydraulic loading system used to generate the normal force, #7: load-cell used to measure the normal force, #8: horizontal frame, #9: accelerometer, #10: laser displacement transducer.

To collect and store data, custom data acquisition software was developed in LabVIEW®, which is able to work at 50 kHz sampling-rate using FPGA programming. Data post-processing is done in MATLAB ®. Raw data can be noisy, and the noise is significantly amplified when the signal is differentiated, e.g. calculating velocity by differentiation of displacement measurements. Accordingly, a digital Butterworth filter (a low-pass filter with custom cut-off frequency) in MATLAB ® is used to eliminate high frequency noise. Velocity is also calculated by integrating accelerometer measurements to ensure that real oscillations in velocity (system vibrations) are not filtered. Using the digital filter can induce time shifts (i.e. delays) in the signal. To eliminate delays, the raw signal is filtered (a positive delay is induced), then it is reversed and filtered again to cancel the delay, and then it is reversed again [*Briers III, 2015*].

The dynamics of the components of the loading system and the test-sample are coupled, so experiments were designed and conducted to test isolated components as well as the entire system with and without deforming test-samples. The first experiments done were simple blow-down tests of the lower pneumatic chamber while not allowing movement of the piston; in which P_L is recorded while activating the Quick-Acting Valve (QAV). This procedure decoupled the gas dynamics from the dynamics of the moving components, so that the model of the exhausting gas could be examined more directly (i.e., Equation 3.18 was decoupled from Equation 3.1 and 3.5). For the second series of experiments, the piston was free to move with no sample present while the QAV was activated allowing measurement and evaluation of the dynamic response of

the loading system and comparison with the model simulations. Finally, a series of experiments were designed and undertaken to simulate and evaluate system-sample interactions for a wide range of test-sample behaviors (i.e. different load-path scenarios).

4. 3 Model of gas exhaust for a fixed piston position

The analytical model developed in Chapter III is based on the assumptions of isentropic expansion and ideal gas behavior, which are valid only if the process is adiabatic and fully reversible. Indeed, the gas exhaust is very fast so there is relatively little time for heat transfer to take place; however, the amount of heat transfer is not zero, and the process cannot be reversible because of the fluid viscosity and friction within the system. Therefore, a polytropic model was considered; i.e., $PV^n = c$, where P is pressure, V is volume, n is the polytropic index and c is a constant. For an isentropic expansion, n is equal to the specific heat ratio of the gas, γ, and for an isothermal expansion n is equal to 1. Thus, gas exhaust in the HSLS should have an n value between 1 and γ, which has been confirmed by experiments over a wide range of P_0. The value of n was found to be 1.55 (n = 1.55), which demonstrates the polytropic nature of the expansion process. For a complete isentropic process, the n value would approach the ideal behavior (or γ of 1.67).

Helium was selected for operation of the pneumatic cylinder because it has a large specific gas constant, R. Based on Equation 3.14 and 3.18, large values for R result in higher sound speed in gas, and consequently the sonic flow passing through the orifice achieves a greater mass flow rate. Therefore, by using helium, pressure can decrease in the lower chamber more quickly than for air. The pressure records for the case of a fixed

piston are compared to the model predictions; for example, the experimental record of P_L is shown in Figure 4.3 for the case P_0 = 5.4 MPa and A_t = 0.6 cm^2. Assuming ideal behavior (n =1.67), the model predicts a sharper pressure change than observed, whereas the model with n = 1.55 fits with the experimental record very well.

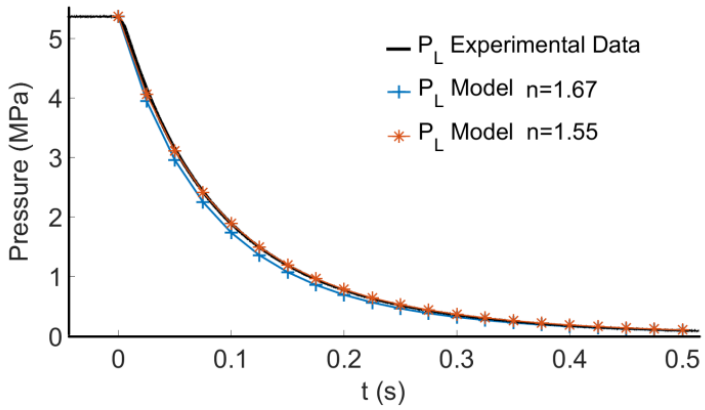

Figure 4.3: Pressure change in the lower chamber of the pneumatic cylinder. The piston is fixed in place and gas exhausts from the QAV. Experimental data is compared to the model prediction for two values of *n*.

4. 4 Velocity-step dynamics for a freely moving piston

A set of experiments were conducted without a test-sample to evaluate the machine response with a freely moving piston (F_s = 0). The results of one of these experiments are shown in Figure 4.4; for this case the PPCV are P_0= 200 kPa, A_t= 0.23 cm^2 , and C_d= 100 kN.s^2.m^{-2}. The experimental results show the apparatus is able to achieve high accelerations and decelerations even if the initial pressure is relatively low. Also, velocity does not change much over the relatively long stroke of the pneumatic

piston and the desired velocity-steps could be achieved. The target velocity of the piston can be controlled simply by changing the size of the orifice at the exhaust port of the pneumatic cylinder; leading to velocities from 0.001 $m.s^{-1}$ to 1 $m.s^{-1}$.

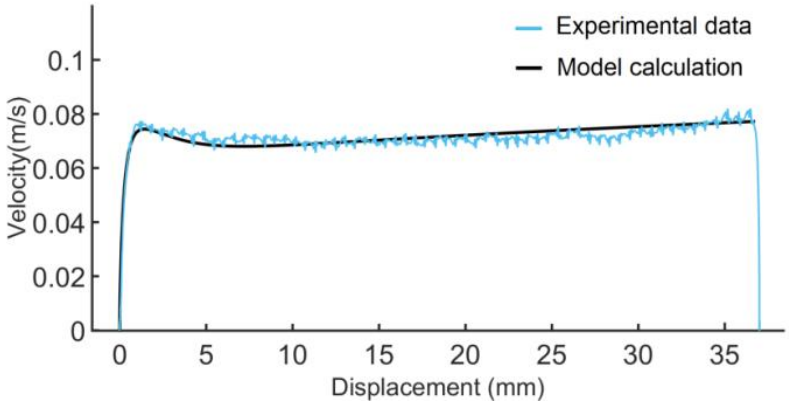

Figure 4.4: Velocity response versus displacement. The model prediction is compared with experimental data for an experiment in which the piston displaces for 37 mm with no test-specimen load ($F_s = 0$)

4. 5 Velocity-step dynamics with test-sample loads

A series of experiments were conducted to investigate machine and sample interactions ($F_s \neq 0$); the focus here is the mechanical behavior of the machine rather than that of the rock test-samples. The experiments on rock samples included frictional sliding in triaxial and double-direct shear configurations, and uniaxial compression tests (Figure 4.1). The selected samples produced the spectrum of behaviors from work-hardening after yield, to abrupt and large-magnitude weakening after yield. Rock-sample behavior is not completely known before the experiments, so an approximate sample

behavior was assumed (F_{s0}, $\Delta F_s/F_{s0}$, D_c) in the model to determine the optimum PPCV (P_0, A^*, C_d) necessary for a velocity-step response. During the actual tests, the resistive force of each sample, F_s, the corresponding sample displacement, y, and the velocity of the piston were measured directly by sensors. After the experiment, the observed force-displacement record for the sample (i.e., the true sample response) was used with equations 3.1, 3.5 and 3.18 to verify that the model-calculated velocity path matches the measured velocity path (i.e., validation of the model). If the F_s assumed before the experiment is significantly different from the force that is measured, an ideal velocity-step may not be achieved. In this case, the experiment can be repeated on the same type of rock-sample using a refined set of PPCV. By using the recorded force-displacement data as the input of the model, the appropriate PPCV for a velocity step are found generally after one or two iterations.

The preliminary velocity-step friction experiments (rock-on-rock) demonstrated varying magnitudes of dynamic weakening in both triaxial and double-direct shear configurations; the maximum weakening observed was $\Delta F_s/F_{s0}$ of 50%. The results indicate that dynamic weakening can occur over a very small displacement, D_c, as low as 1 mm. In these experiments, the 37 mm stroke during high-speed operation is sufficient to observe the entire weakening process and subsequent steady-state sliding behavior. Therefore, the tests show that frictional dynamic weakening can be studied successfully using the HSB despite the stroke limitations of the biaxial machines (compared to rotary machines).

4.5.1 Experiments on test-samples with frictional dynamic weakening behavior

Friction tests were conducted at normal stresses from 1 to 25 MPa to evaluate the machine behavior for different values of F_{s0} (up to 150 kN). An example experiment on a Granite sample in a double-direct configuration is shown in Figure 4.5. The normal stress was 3.5 MPa and apparent contact area was 5×7.5 cm^2; the PPCV were set to: P_0= 2 MPa, A_t= 7.9 cm^2, C_d= 140 $kN.s^2.m^{-2}$. For this test, F_s can be modeled as an exponential decay (Figure 4.5a) based on Equation 3.19, with values of F_{s0}, $\Delta F_s/F_{s0}$ and D_c equal to 18 kN, 30% and 1.2 mm, respectively. As shown in Figure 4.5b, the velocity step is achieved in 1 mm of displacement and velocity is maintained nearly constant (0.7 $m.s^{-1}$) over the remaining 26 mm stroke. The velocity curve obtained by the model using the observed force-displacement record for the sample fits very well with the experimental data.

For the friction experiments, the HSLS was able to achieve velocity-steps and the model represented the actual system response accurately. However, in future friction experiments, more extreme sample behaviors can be expected for some rock materials and test conditions. For example, a pressure vessel might be employed in the ultimate machine to conduct friction experiments on confined samples at higher normal stress and with pressurized pore fluids, so more dramatic weakening events may occur. For this reason, additional experiments were conducted in uniaxial compression (Figure 4.1) to further test the prototype loading system and identify its limitations. For illustration, the results of experiments on test-samples with two end-member behaviors are shown: strengthening after the yield point, and dramatic weakening after the yield point.

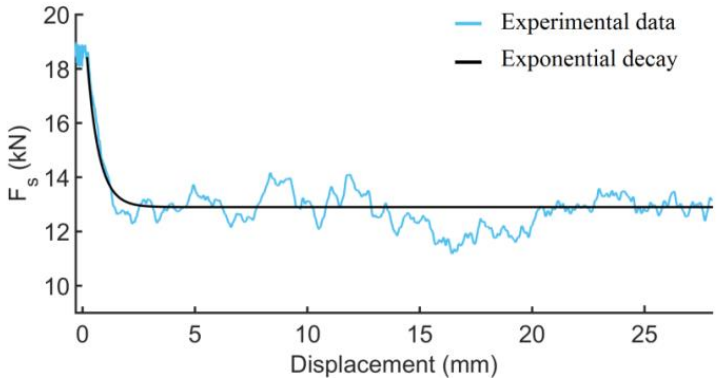

(a)

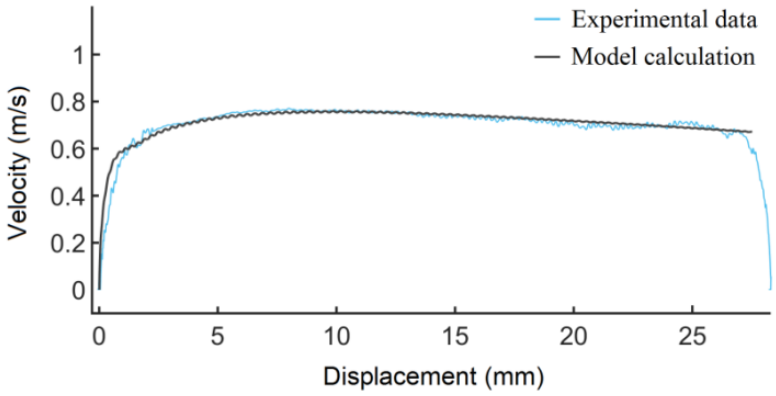

(b)

Figure 4.5: A high-speed friction test exhibiting dynamic weakening. a) sample frictional resistive force, F_s as a function of displacement; F_{s0}=18.4 kN, $\Delta F_s/F_{s0}$=30%, D_c=1.2 mm, b) velocity as a function of displacement; experimental data is compared to the model calculation.

4.5.2 Experiments on test-samples with strengthening behavior

Experiments on samples that displayed strengthening after yield are represented by a uniaxial compression test of a cylinder of Austin Chalk (diameter and length of 4.6

cm and 7 cm, respectively). The sample contained pre-existing fractures, and was wrapped in polyolefin heat-shrink tubing to provide a small lateral confinement (~1 MPa) during the high-speed deformation test. During shortening, the confinement helps generate a resistive frictional force from sliding along the pre-existing fractures, which leads to additional compound fracturing in the sample; the PPCV were set as P_0= 1 MPa, A_t = 2.2 cm^2, and C_d= 80 kN.s^2/m^2. For this experiment, the pre-fractured sample was loaded statically to a resistive force of 12 kN, and then the high-speed deformation test was initiated. Yielding occurred at F_s = 15 kN, and then strength increased about 45% (to 22 kN) over 13 mm of shortening (Figure 4.6a). The velocity of the loading rod increased from 0 to 0.40 m.s^{-1} in less than 2 mm of displacement and subsequently maintained a velocity of about 0.48 m.s^{-1} with less than 5% variation over the major portion of the stroke (Figure 4.6b). The overall error between the model prediction (equations 3.1, 3.5 and 3.18) and the experimental result is less than 2%.

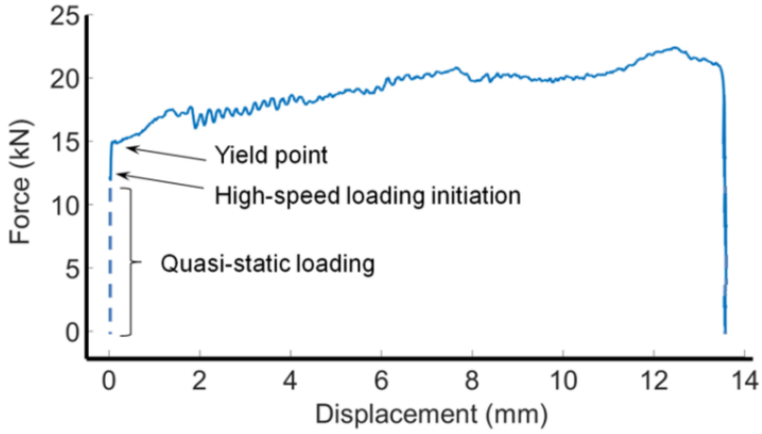

(a)

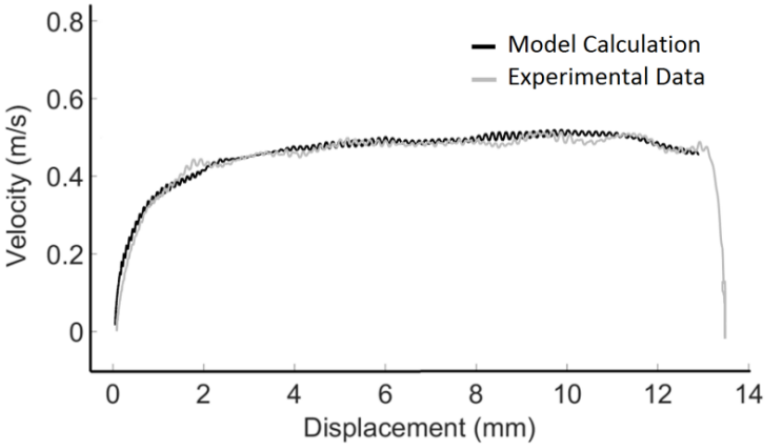

(b)

Figure 4.6: Test-specimen strengthening, and the corresponding velocity response. a) specimen resistive force, F_s, as a function of displacement; first the sample is loaded statically and then the high-speed loading intiated at F_s =12 kN, b) velocity as a function of displacement; experimental data is compared to the model calculation.

4.5.3 Experiments on test-samples with extreme weakening behavior

Experiments on samples that displayed marked weakening after yield are represented by a uniaxial compression test of an intact (i.e., no pre-existing fractures

present) cylindrical sample (diameter and length of 4.48 cm and 7 cm, respectively) of Austin Chalk. In this high-speed experiment, the cylinder failed abruptly by a brittle shear fracture and was shortened by approximately 15 mm (i.e. an axial strain of 21%). The fracture resulted in a nearly complete drop in F_s, but because the sample was wrapped inside polyolefin heat-shrink tubing that provided a small lateral confinement (~1 MPa), a small resistive force from sliding along the fracture was maintained over the stroke. The sample was initially loaded statically to F_s = 45 kN, and then the high-speed shortening was initiated; in which the PPCV were set to P_0 = 3 MPa, A_t = 2.2 cm ^{2}, and C_d = 90 kN.s^2/m^2. The sample fractured at F_s =90 kN, and F_s decreased (~75%) to 20 kN in 0.5 mm of displacement.

As shown in Figure 4.7a, the mechanical response during fracture and subsequent shortening of the sample is similar to an extreme case of dramatic force-drop during frictional dynamic weakening. Using Equation 3.19, post yield behavior of the sample can be modeled with an exponential decay, in which, F_{s0} = 90 kN, $\Delta F_s/F_{s0}$ = 75%, and D_c= 0.5 mm. As shown in Figure 4.7b large vibrations are present in the velocity response, which could not be explained by the model that was derived in Chapter III.

a)

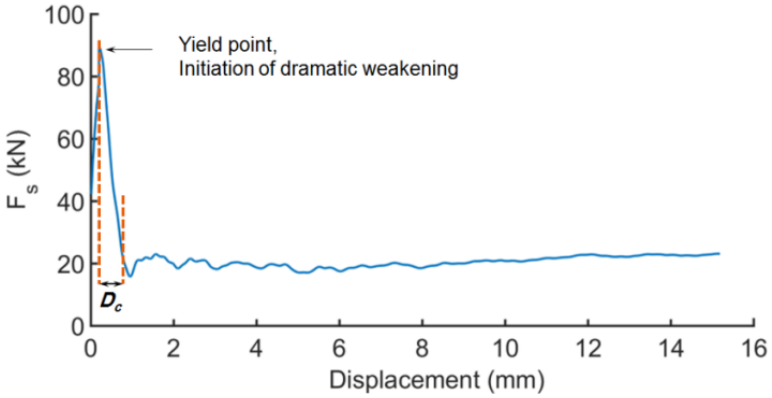

b)

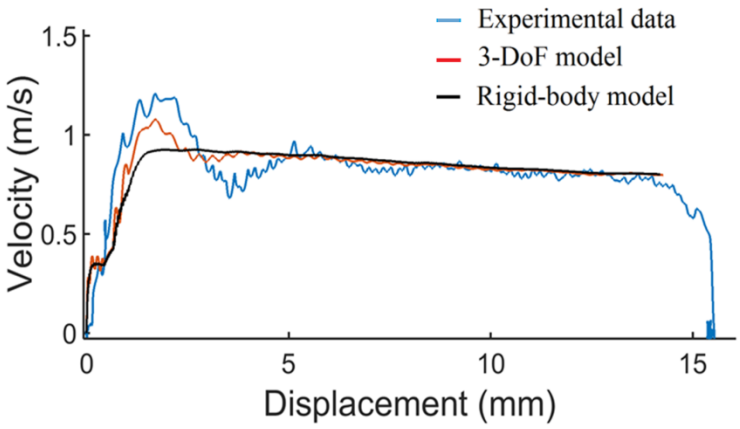

Figure 4.7: An example of dramatic weakening. a) specimen resistive force, F_s as a function of displacement; F_{s0}=90 kN, $\Delta F_s/F_{s0}$=75%, D_c=0.5 mm, b) velocity as a function of displacement; experimental data is compared to the model calculations considering: 1) rigid loading column, 2) elastic loading column.

4. 6 Vibrations of the HSLS

The model developed in Chapter III assuming rigid components in the loading column is computationally efficient and is fast for exploring the bulk behavior of the system for different conditions. However, to have an accurate model that shows the details of the transient velocity, we need to consider the elasticity of the loading column.

For this purpose, the continuous structure is modeled as a discrete system with 3 DoF as shown in Figure 4.8. The stiffness of the frame ($2 \times 10^{10}\ N.m^{-1}$) is very high relative to the loading column and it can be assumed rigid. A continuous loading column can be modeled using finite lumped masses and springs for simplification. Each continuous rod can be replaced with a spring and its mass may be split equally on the end points of the rod (Figure 4.8) because the relative velocity of the two ends of each rod is much smaller than the rigid translation velocity of the component. In the prototype system, the stiffness of the rod connecting the damper and pneumatic plates is $k_1 = 3 \times 10^8\ N.m^{-1}$ and the stiffness of the rod between the pneumatic piston plate and sample is $k_2 = 2 \times 10^9\ N.m^{-1}$. Stiffness of a rod can be calculated as $k = EA/L$, where E is Young's modulus of elasticity, L is the length of the rod and A is the cross section area of the rod.

Using the 3-DoF model shown in Figure 4.8, Equation 3.1 can be written as following:

$$\begin{aligned} &m_1\ddot{z}_1 + k_1(z_1 - z_2) + F_d = 0 \\ &m_2\ddot{z}_2 + k_1(z_2 - z_1) + k_2(z_2 - z_3) = (P_U - P_L)A_p \\ &m_3\ddot{z}_3 + k_2(z_3 - z_2) = -F_s \end{aligned} \tag{4.1}$$

where, F_s is the test sample force, $F_d = C_d\dot{z}_1^2$. m_1, m_2, m_3, z_1, z_2 and z_3 are illustrated in Figure 4.8. The sample can be pre-loaded to $F_s = F_0$ just before high-speed slip initiates at $t = 0$ which corresponds to the instant that the QAV operates. The initial conditions associated with Equation 4.1 are as follows: $z_1 = z_2 = F_0/k_2$, $z_3 = 0$, $\dot{z}_1 = \dot{z}_2 = \dot{z}_3 = 0$. In addition to stiffness, every component has a structural damping coefficient that can be determined based on the type of joints and the intrinsic damping property of its

material. The structural damping coefficient can be represented by an equivalent viscous damping coefficient ζ based on dissipated energy, which is generally very small for steel structures (≤ 0.04).

Equations 3.2 to 3.19, presented in Chapter III, can still be used with the following variable changes: y is replaced with z_3 in Equation 3.19, and it is replaced with z_2 in Equations 3.4 to 3.9. The velocity curve obtained using the 3 DoF model is shown in Figure 4.7b. Although some vibrations have been predicted by the model, the amplitude of vibrations is smaller than what was observed in the experiment. In the following section, the vibration of the HSLS is investigated further.

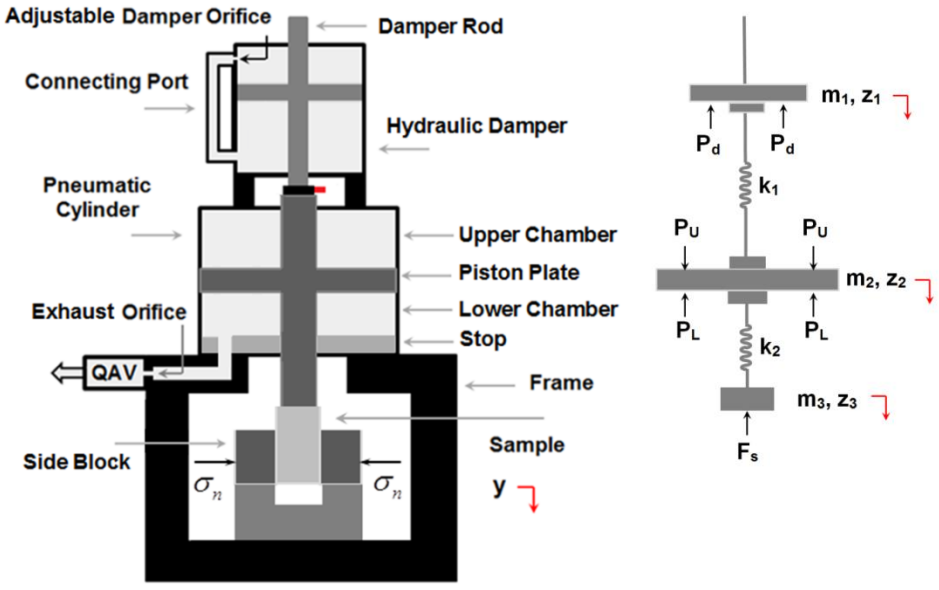

Figure 4.8: Schematic of the 3-DoF model for the loading column. m_i denotes the discretized mass associated with ith DoF (other symbols are defined in Nomenclature).

4. 7 Modification and enhancement of the vibration model

As shown by the experiments, some cases of system-sample interaction produce vibrations that are not well-modeled with the 3-DoF model. For cases with an abrupt loss in sample strength, the HSLS undergoes an impulse-type load. In such conditions, the compressibility of hydraulic fluid can have a significant influence on the velocity response, which is not treated in the 3-DoF model. In general, as the damping piston moves downward, the hydraulic fluid flows from the lower to the upper chamber through the connecting tube (Figure 4.8). As a result of the flow, a differential pressure is generated between the chambers due to the pressure drop at the damper orifice and the connecting port. In the case of an impulse, the compressibility of the fluid leads to pressure oscillations in the lower chamber of the damper. This effect appears largely responsible for the observed vibrations. Accordingly, the effect of fluid compressibility in the damper is added to the model, which not only improves accuracy but also allows parametric study of damper behavior, leading to an improved design for the damper.

For the model, the compressibility of the fluid in the connecting tube can be neglected because tube volume is very small relative to the volume of the chambers. Therefore, based on continuity, the rate of change in mass of hydraulic fluid in the lower chamber is equal to the mass flow rate of the fluid entering the upper chamber through the adjustable orifice (Figure 4.8), and the following relation holds,

$$\frac{dm_d}{dt} = -\rho_d A_{do} V_{do} \tag{4.2}$$

where, A_{do} and V_{do} are respectively the area and velocity of flow at the damper orifice, and ρ_d is the density of hydraulic fluid in the lower side (uniform conditions are assumed for the fluid). Mass of the hydraulic fluid in the lower side can be obtained as:

$$m_d = \rho_d h_d A_d \tag{4.3}$$

By differentiating Equation 4.3 with respect to time, the rate of change in mass of the fluid in the lower side can be calculated as:

$$\frac{dm_d}{dt} = \frac{d\rho_d}{dt} h_d A_d - \rho_d \dot{z}_1 A_d + \rho_d h_d \frac{dA_d}{dt} \tag{4.4}$$

Combining equations 4.2-4.4 leads to:

$$-\rho_d A_{do} V_{do} = \frac{d\rho_d}{dt} h_d A_d - \rho_d \dot{z}_1 A_d + \rho_d h_d \frac{dA_d}{dt} \tag{4.5}$$

The hydraulic cylinder has a thick wall and its stiffness is very high, so the change in the inner diameter of the hydraulic cylinder is very small; therefore, it is assumed that $\frac{dA_d}{dt} = 0$. In Equation 4.5, the rate of change in density can be related to the rate of change in pressure of the lower side, as follows:

$$\frac{d\rho_d}{dt} = \beta\rho_d \frac{dP_d}{dt} \tag{4.6}$$

where β is the fluid compressibility (~5×10^{-10} Pa^{-1} for the hydraulic fluid).

The differential pressure between the lower and upper chambers of the damper is due to fluid-wall friction in the connecting port plus the pressure drops at the entrance to the connecting tube, elbows, orifice, and the entrance of the upper chamber. The pressure drop at each of these sections is proportional to the square of fluid velocity at that section ($\Delta P_i \propto V_i^2$). Based on continuity, velocity in the damper port, V_{dp}, can be found as follows:

$$V_{dp} = \frac{A_{do}}{A_{dp}} V_{do} \tag{4.7}$$

where, A_{dp} is the flow area in the damper port and V_{do} is the flow velocity at the adjustable damper orifice. Pressure is zero in the upper chamber so the differential pressure is equal to the pressure in the lower chamber, P_d, which can be calculated based on the pressure drops as follows:

$$P_d = k_{do} V_{do}^2 + \sum k_i \left(\frac{A_{do}}{A_{dp}} V_{do} \right)^2 \tag{4.8}$$

$$P_d = k_d V_{do}^2, \quad k_d = k_{do} + \sum k_i \left(\frac{A_{do}}{A_{dp}} \right)^2 \tag{4.9}$$

By using Equations 4.9, 4.6, and 4.5, the following relation can be written:

$$\frac{A_{do}}{A_d \sqrt{k_d}} \sqrt{P_d} + h_d \beta \frac{dP_d}{dt} - \dot{z}_1 = 0 \tag{4.10}$$

Under the steady state condition, the damping force (P_dA_d) is equal to $C_d\dot{z}_1^2$, so:

$$\sqrt{P_d} = \sqrt{\frac{C_d}{A_d}}\dot{z}_1 \tag{4.11}$$

Also, for the steady state condition, $\frac{dP_d}{dt} = 0$, and by using Equations 4.10 and 4.11:

$$\frac{A_{do}}{A_d\sqrt{k_d}} = \sqrt{\frac{A_d}{C_d}} \tag{4.12}$$

Finally, the equation describing the change in pressure in the damper can be written as follows:

$$\frac{dP_d}{dt} + \frac{1}{(h_{d\,0} - z_1)\beta}\left(\sqrt{\frac{A_d}{C_d}P_d} - \dot{z}_1\right) = 0 \tag{4.13}$$

where h_{d0} is the initial height of the lower chamber of the damper. The damping force can be recorded as mentioned before, and by having constant velocity over the stroke (steady-state condition) C_d can be obtained experimentally as a function of damper orifice size. Now, instead of using $F_d = C_d\dot{z}_1^2$ in Equation 4.1 (which corresponds to the steady-state conditions), the following equation can be used:

$$F_d = P_dA_d \tag{4.14}$$

where, Equation 4.13 is used to obtain the transient P_d. Figure 4.9 illustrates the velocity curve that is obtained by the modified model for the example fracture-experiment on Austin Chalk, which compares very well with the observed velocity curve.

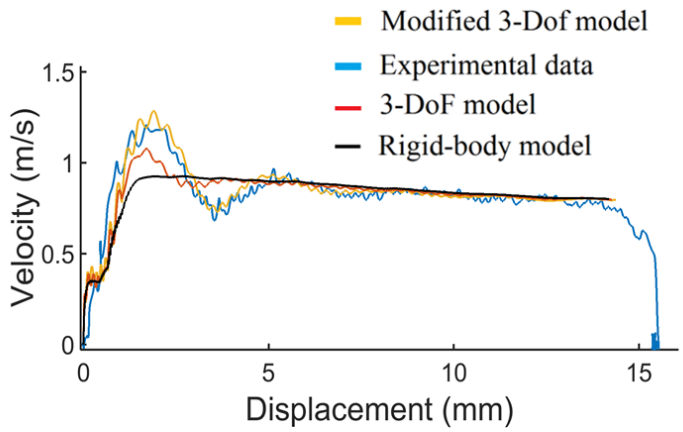

Figure 4.9: Velocity as a function of displacement. Experimental data is compared to the model calculations; the sample force-displacement curve was presented in Figure 4.7.

4. 8 Improvements in loading system design

Having developed a model that can accurately represent the transient velocity response and the vibrations of the system, and inspection of the governing equations, one can identify the important design parameters that play a key role in the system behavior and optimized the design to reduce vibrations. For example, model analysis shows that the overshoot and vibrations can be reduced by increasing the stiffness of the damper rod (k_1) and by reducing the effect of the compressibility of the damper fluid. To increase k_1, a stiffer material (e.g. steel) can be used instead of the aluminum alloy in the prototype HSLS, and the cross section area of the damper rod can be increased such that k_1 is raised to $3 \times 10^9\, N.m^{-1}$. Based on Equation 4.13, the effective hydraulic fluid compressibility can be decreased by decreasing h_{d0} and enlarging the damper piston plate, A_d. For an improved design of the HSLS, it is feasible to make A_d three times larger than the current area. In this way, not only are the vibrations of the HSLS reduced,

but the damping capacity is increased by a factor of 3 such that the HSLS is able to achieve velocity steps for a wider range of conditions and sample behaviors (as discussed in Chapter III). The velocity curve calculated for the Austin Chalk fracture-experiment using the modified 3-DoF model for the improved design is shown in Figure 4.10. In that case, the target velocity is achieved in less than 2 mm of displacement without a large overshoot. In fact, the velocity curve is very close to the curve plotted for a system with rigid components, which indicates that the improved design is very robust to vibrations. Using the improved design, velocity-steps to terminal velocities of 0.01 to 1 $m.s^{-1}$ can be generated under higher loads (resulting from increasing normal stresses up to 100 MPa).

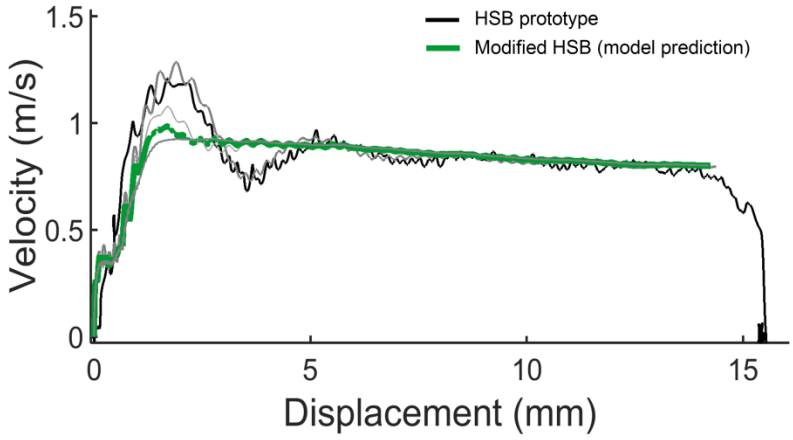

Figure 4.10: Velocity response of the modified system. Experimental data is compared to the model calculations; the sample force-displacement curve was presented in Figure 4.7; and model calculations for the existing prototype HSLS were shown in Figure 4.9. The green curve represents the velocity response of the modified system. Using the modified design for the new testing machine, vibrations are reduced significantly and a step-wise velocity pattern can be achieved even under impulse-type loads.

CHAPTER V

EXPERIMENTAL ANALYSIS OF DYNAMIC WEAKENING IN ROCK BY CHARACTERIZATION OF CONTACTS AND FRICTIONAL FLASH HEATING

5. 1 Introduction

As explained in Chapter I, sliding rock-samples at slip-rates > 1 mm.s^{-1} can lead to a significant reduction of friction, often referred to as dynamic weakening. Thermal effects are understood to be the cause of dynamic weakening, and flash weakening is one of the main weakening mechanisms that can be activated at the initial stages of seismic slip due to flash heating of sliding-surface contact junctions. Flash-weakening can play a key role in transient friction weakening during nucleation and propagation of earthquake ruptures. As discussed in Chapter I, the flash-weakening model explicitly explains the velocity dependence of friction. However, in the classic flash-weakening model, the effect of macroscopic Normal Stress (NS) is neglected as the micro-asperities are assumed to be all at the theoretical yield stress of material, σ_c, measured by micro-indentation hardness tests [e.g. *Rice*, 2006; *Dieterich and Kilgore*, 1994, 1996]. The relation between frictional weakening and velocity, presented by the flash-weakening model, is well demonstrated by previous studies [e.g., *Rice*, 2006; *Beeler et al.*, 2008; *Goldsby and Tullis*, 2011], but the effect of NS on flash-weakening has not been

investigated sufficiently. One of the effects of NS on flash-weakening can be explained based on the sliding surface transient temperature. In the previous works by [*Proctor et al., 2014*; *Yao et al*., 2016a, 2016b; *Elbanna et al.*, 2014], it is suggested that a rise in the bulk surface temperature (T_s) enhances flash-weakening by decreasing $T_w - T_{c0}$ in Equation 1.9 and 1.12 ($T_{c0} = T_s$). The surface temperature rise is directly influenced by NS, however, in those studies, the stress and temperature on the sliding surface was assumed to be uniform.

In this chapter, flash-heating in granite (Westerly)[16] is studied by conducting sliding experiments using the HSB testing-machine. The effects of sliding-rate and NS on weakening were investigated and classic flash-weakening model assumptions were assessed using stress and temperature distribution on the sliding surface. For this purpose, a thermal imaging technique is presented to document magnitude and distribution of flash temperatures on the sliding surface. The results show that the temperature distribution is highly heterogeneous on the surface due to stress localization in millimetric areas, and local temperatures are dramatically higher than those calculated in the previous modeling studies (assuming a uniform stress distribution on the surface [e.g., *Proctor et al*., 2014; *Yao et al*., 2016a, 2016b; *Elbanna and Carlson*, 2014]). Moreover, natural faults surfaces generally display anisotropic roughness over a range of length scales [e.g., *Power and Tullis*, 1991], with elongated quasi-elliptical bumps and

[16] Westerly granite has been used in many previous studies and is well described [e.g., *Tullis and Yund*, 1977]. Westerly granite is light-gray, fine-grained (the average grain size is 0.75 mm [*Tullis and Yund*, 1977]), and is isotropically textured. Westerly granite is composed of the following minerals: ~30% quartz, ~30% K-feldspar, ~30% of oligoclase or albite, and about 5-10% biotite.

depressions aligned in the slip direction [e.g., *Sagy et al*., 2007]. Thus, the size-distribution of contacts formed during slip is likely different from the assumptions used to describe flash-weakening. For this reason, the thermal images have been analyzed to characterize the contacts formed in different length- and time- scales, and the effects of multi-scale flash-heating on weakening have been investigated. Also, the 2-D thermographic maps of temperature on the sliding surface can be used to identify and quantify the magnitude and distribution of local stress on the surface, which is used to understand elastic and plastic deformation at contacts.

5. 2 Experimental procedures

Sliding friction experiments were done in the double-direct shear configuration using the prototype of High-Speed Biaxial (HSB) apparatus described in Chapters III and IV. The experiments were done on rectangular blocks of granite (Westerly) with 50×75 mm^2 contact area. The dimensions of the sample and the stationary side-blocks were 125 × 50 × 50 mm (height × width × depth) and 75 × 50 × 25 mm, respectively. A precision grinding wheel (#60 grit size) was used to prepare flat and parallel contact surfaces. The grinding marks on the surface were removed by conducting a few sliding friction runs to allow the surface to evolve towards a steady-state condition in terms of roughness. To achieve reproducibility in mechanical behavior and flash heating characteristics, between each successive experiment, the surface of the contacting faces was brushed and the samples were re-used. Experiments were then conducted by applying the desired normal load on the sample assembly using the horizontal loading system. After reaching the desired NS, the vertical loading system was used to slide the

sample center-block initially at 1 $mm.s^{-1}$ for several millimeters and then impose a jump in velocity to a sustained seismic slip-rate in a range of (100-1000 $mm.s^{-1}$). The experiments were done at wide range of NS (1-25 MPa), and the maximum stroke of the high-speed slip was ~ 4 cm.

After each experiment, striations are developed on the rock surface by ploughing and abrasion, which suggests that shear stress is localized along the surface sufficient to induced permanent deformation. To investigate the characteristics of true contacts and stress localization, the temperature distribution on the sliding surface was measured using an infrared (IR) camera. Figure 5.1, illustrates the arrangement of the IR camera and the sample assembly. The side-blocks of granite were supported by steel side-blocks and two cylindrical spacers were used to fill the space between the sample assembly, load-cell and horizontal hydraulic loading system. A pass through hole was drilled into the granite and steel side-blocks so that a circular window (22 mm in diameter) of the sliding surface of the sample was exposed to the IR camera. Also, a groove was made in the cylindrical steel spacer to accommodate a mirror in front of the hole with 45° angle relative to the rock surface. The mirror had a gold coating suitable for reflecting IR emissions (referred to as hot-mirror). The IR camera was FLIR SC7650 equipped with a 50 mm lens (SC7000), which can take IR thermographs at a rate of 300 frames/sec and at a resolution of 75 μm. The full temperature range of the IR camera is 20-300 °C, which was extended to 550 °C using a neutral density IR filter[17]. The effect of the hot-

[17] The resolution of the images are 320 × 256 pixels, and the accuracy of the camera is ±1% of the range.

mirror, IR filter, emissivity of rock sample, and distance of the camera to surface were calibrated by imaging the surface of an independently-heated block of granite with the IR camera, and comparing thermographs with temperature measurements obtained using a surface mount thermocouple. The difference in the temperatures measured for different minerals in the granite sample (due to different IR emissivity) was negligible. The camera could not provide measurements in the full range of 20-550 °C in one single experiment. To overcome this technical limitation, experiments (at identical conditions) were repeated with different camera settings to characterize the full temperature distribution.

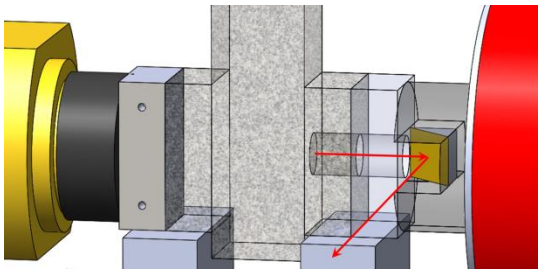

Figure 5.1: Experimental setup for taking IR images. The middle block of rock is sandwiched between the stationary side blocks using a hydraulic loading-system and is slid downward by using the HSLS. A hot mirror was used to reflect the IR emissions from the circular window on the sliding rock surface towards the IR camera. The angle of the mirror surface relative to the rock surface was 45°.

5. 3 Mechanical behavior

5.3.1 Effect of velocity on dynamic weakening

The sliding friction experiments showed that friction can decrease dramatically at sliding-rates higher than 1 $cm.s^{-1}$. At seismic slip-rates and under moderate NS, the transient weakening process was generally initiated by an abrupt friction force-drop (concurrent with velocity-step) followed by gradual weakening at constant sliding-rate. An example velocity-step and the subsequent weakening under a constant NS of 8 MPa is shown in Figure 5.2. First, the sample is slid for ~4 mm at 1 $mm.s^{-1}$ where quasi-static friction is ~0.7, then velocity is jumped to 300 $mm.s^{-1}$ in less than 1 mm of slip. Sliding-rate is maintained in a range of 300-350 $mm.s^{-1}$ for ~27 mm, and at the end of the high-speed slip, friction is 0.47.

As the results show, dynamic weakening is enhanced with velocity. As sliding rate increases, the frictional heat generation rate rises at the contacts leading to higher flash temperatures (Equation 1.6). Therefore, flash-weakening of microscopic contacts may explain the relation between magnitude of weakening and sliding-rate. The concurrent (instantaneous) changes in friction with small changes in velocity (Figure 5.2 and 5.3) further confirm the nature of the velocity dependent friction weakening mechanism. Three examples of the velocity-step experiments done at the same NS (~8.5 MPa) but to three different target velocities of 100, 350, and 800 $mm.s^{-1}$ are illustrated in Figure 5.3.

To investigate the effects of velocity on dynamic weakening and friction further, a series of experiments were done over a wide range of target sliding-rates. The results

showed that the magnitude of weakening increases with sliding-rate, and at moderate to high NS, the relation between velocity and weakening may be explained by the weakening model primarily. Figure 5.4 illustrates friction and dynamic weakening as a function of velocity for those experiments done at sliding rates of 20-1000 $mm.s^{-1}$ and NS of 8-20 MPa. In Figure 5.4, the magnitude of friction is normalized by the initial quasi-static friction (sliding at 1 $mm.s^{-1}$) and is plotted versus velocity for 3 intervals of normal stress. Also, in this figure, the experimental data is compared with flash-weakening model (Equation 1.12) assuming μ_w=0.4, μ_0=0.7, and V_w=100 $mm.s^{-1}$. The effect of velocity of the sliding surface on the transient friction is presented and discussed in a greater depth in Chapter VI.

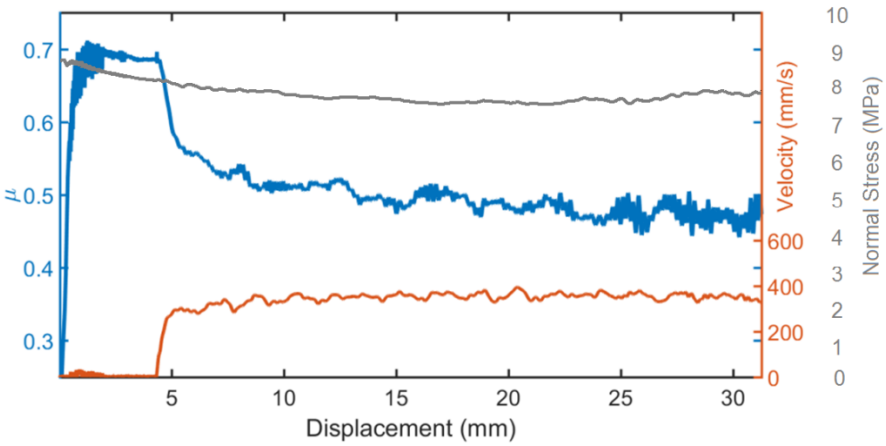

Figure 5.2: An example velocity-step and the consequent dynamic weakening of friction (#HSB-WG-62). Friction decreases concurrently with sliding rate during the rise time and gradual weakening continues at constant sliding rate. The target NS was 8 MPa; however, NS variations were caused by compaction and dilation of the rock samples during frictional sliding. The NS variation was reduced by connecting a pneumatic-hydraulic accumulator to the horizontal hydraulic loading-system.

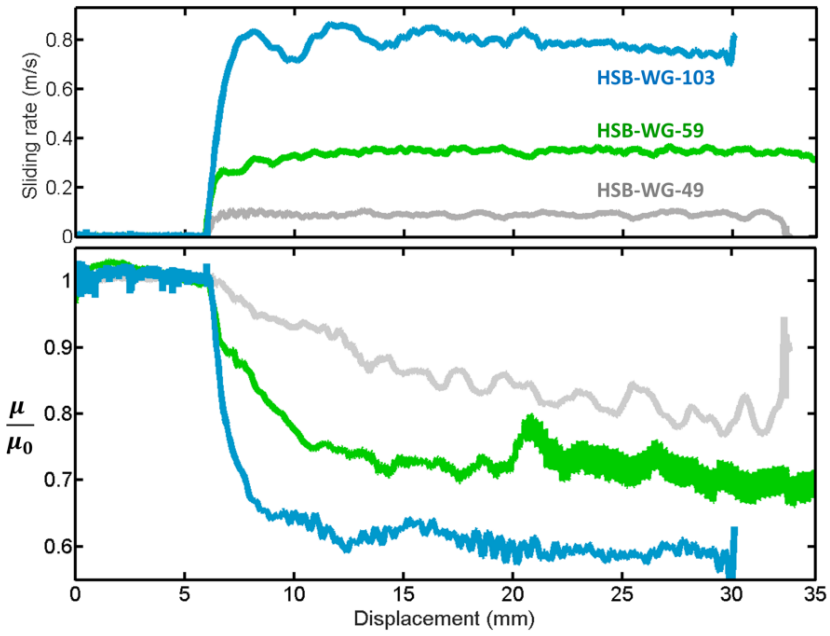

Figure 5.3: The effect of sliding rate on dynamic weakening. The transient friction (normalized by the initial quasi-static friction) is shown for three velocity steps conducted at the same NS (~8.5 MPa); dynamic weakening enhances with sliding rate.

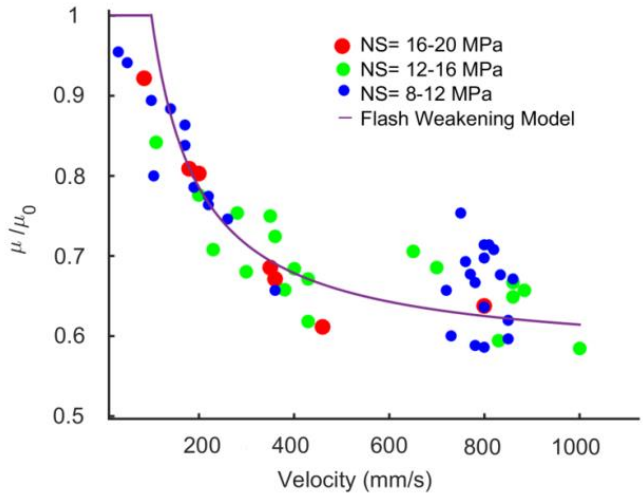

Figure 5.4: Coefficient of friction versus velocity for 3 intervals of normal stress. Friction coefficient is normalized by the initial quasi-static friction, μ_0 (each point in the figure represents one experiment). μ_0 is measured at sliding rate of 1 mm.s^{-1} (μ_0~0.7), and μ is the coefficient of friction measured within 5 mm of slip from the velocity peak. Classic flash-weakening model fits well with experimental data for high NS.

5.3.2 Effect of normal stress on dynamic weakening

The experimental results reveal that the flash-weakening model fits well with experimental data for high NS (Figure 5.4). However, for NS lower than 8 MPa, weakening is considerably less than what the flash-weakening model predicts. For low NS, not only the magnitude of weakening is smaller, but also the weakening process is much slower (long D_c). As NS increases, the amount of weakening increases and D_c becomes smaller. At intermediate to high NS, the weakening process consists of an instantaneous weakening phase (concurrent with the velocity rise) followed by a gradual weakening at constant sliding-rate. As an example, results from two sets of experiments are shown in Figure 5.5. The velocity paths are similar for the experiments in each set, but the NS is varied. In Figure 5.5a, the three velocity-steps were done at 0.1 $m.s^{-1}$ under NS of 1.5 (#HSB-WG-50), 7.5 (#HSB-WG-45), 10.5 MPa (#HSB-WG-147), respectively. At 1.5 MPa, the change in friction is very slow and its amount is only ~7%. When a NS of 7.5 MPa is applied, the amount of weakening increases, but the weakening distance (D_c) is still long. However, at 10.5 MPa, an abrupt drop in friction is observed, which is consistent with classic micro-scale flash-weakening model (i.e. weakening is instantaneous with respect to change in velocity). Figure 5.5b show similar trends in weakening as a function of NS for a target velocity of 800 $mm.s^{-1}$.

In addition to the velocity-step load-paths, self-generated stick-slip events can occur under quasi-static loading before initiation of the dynamic velocity-steps. In contrary to velocity-steps, which are imposed by the pneumatic loading-system, these stick-slip events are triggered by frictional weakening of the rock-sample and continue

due to the stored energy in the pneumatic loading-system. Therefore, stick-slip events may represent fault slip-instabilities very well. An example of the self-generated stick-slips is shown in Figure 5.5b. The stick-slips are initially small (with maximum velocity of 3-5 cm.s^{-1} leading to 5-10% change in friction); however, the last stick-slip is relatively large, where a peak velocity of ~200 mm.s^{-1} is achieved and friction drops by 25%. The amount of weakening during this stick-slip event is higher than weakening in the experiment with much higher velocity (750 mm.s^{-1}) but under lower NS=1.8 MPa (test #HSB-WG-34 in Figure 5.5b). Therefore, NS can play a significant role in dynamic weakening.

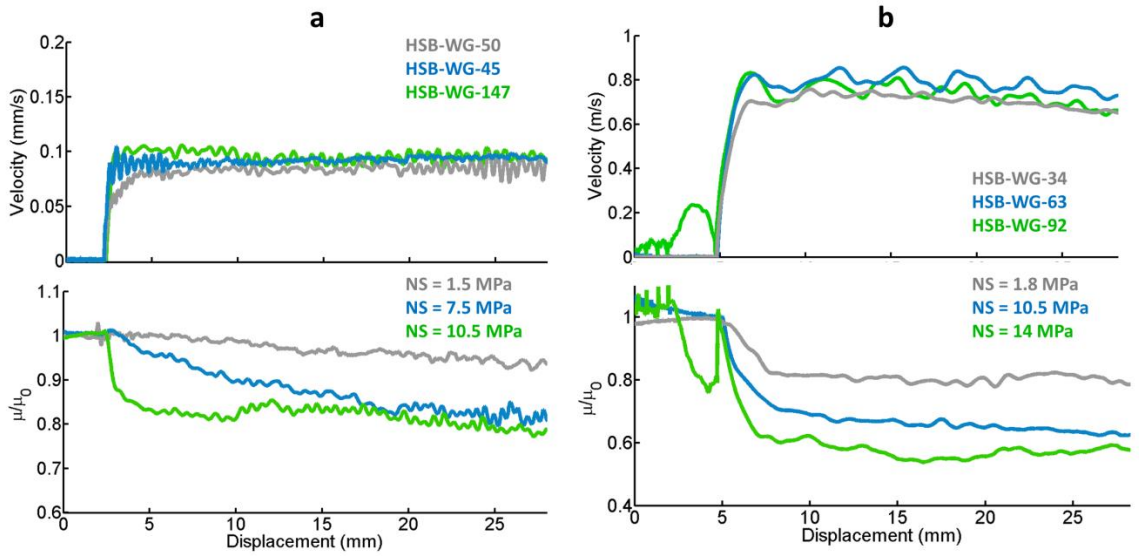

Figure 5.5: The effect of NS on dynamic weakening. Each set of experiments consists of similar velocity-steps done at different NS. The amount of weakening and the weakening distance is affected by NS. Friction is normalized by the magnitude of quasi-static friction. a) 3 velocity-steps to 0.1 m.s^{-1} under NS of 1.5 (#HSB-WG-50), 7.5 (#HSB-WG-45), 10.5 MPa (#HSB-WG-147) respectively, b) 3 velocity-steps to 0.75-0.8 mm.s^{-1} under NS of 1.8 (#HSB-WG-34), 10.5 (#HSB-WG-63), 14 MPa (#HSB-WG-92).

The results indicate that regardless of the sliding rate, the magnitude of weakening increases with NS. However, NS can have a higher degree of influence on weakening at lower sliding-rates. In other words, if sliding-rate is sufficiently high, dynamic weakening can occur even at low NS, whereas at low sliding-rates, dramatic weakening occurs only if NS is high enough. The effect of NS on weakening for a series of experiments conducted under NS of 1-20 MPa and velocity of 100-800 $mm.s^{-1}$ is illustrated in Figure 5.6. Experiments are categorized in three groups based on the sliding-rate. The dependence of weakening on the NS is higher at low NS (<8 MPa), and the magnitude of weakening reaches an upper limit (i.e., saturates) as NS increases. Saturation is reached at lower NS for higher velocity of sliding.

For comparison purposes, the amount of normalized weakening based on the classic flash-weakening model is shown for each range of velocities (Figure 5.6). The classic flash-weakening model ignores the dependence of weakening on NS. Therefore, the amount of weakening can be described by a flat line based on velocity (using the average velocity in each range, and employing Equation 1.12 with parameters that were found empirically in Figure 5.4). Figure 5.6 demonstrates that, at low NS (< 8 MPa), the amount of weakening is highly dependent on NS, which is in an apparent contrast with the flash-weakening model assumptions.

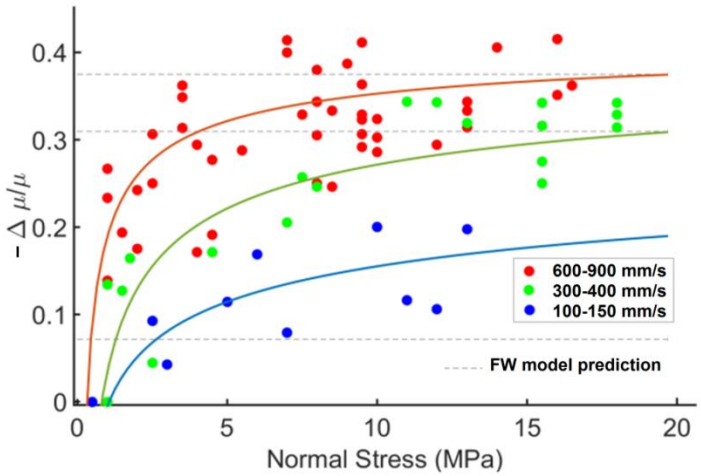

Figure 5.6: Normalized magnitude of weakening versus normal stress for 3 ranges of velocities. $\Delta\mu$ is the change of coefficient of friction from the quasi-static magnitude (each data point represents one experiment). The model parameters are the same as the ones used in Figure 5.4, and for each range of sliding rate, the average sliding rate is used in the model. Weakening is highly dependent on NS for NS < 8 MPa, and the amount of weakening is significantly lower than the prediction of the classic flash-weakening model. The curves are shown for illustration only and do not present an explicit relation between NS and weakening.

5. 4 Sliding surface deformation and flash-heating

5.4.1 Wear and deformation of the sliding surfaces

Due to shear stress during sliding friction experiments, striations develop on the surface of the rock samples by ploughing and abrasion. The amount of wear products formed on the rock surface during each experiment increased with sliding-rate and NS, which is consistent with previous studies [e.g. *Hirose et al.*, 2012; *Boneh et al.*, 2013]. The striations are extended linearly along the slip direction and are spaced evenly and parallel relative to each other (Figure 5.7). The width of the striations increased with slip in the first few millimeters of slip (due to accumulation of wear material and forcing the

wear material to the sides of striations) and then maintained almost constant for the rest of the stroke. The width of the striations varied from several micrometers to 2.5 mm (the maximum width increased with NS). The length of the striations was comparable to the total slip distance. The linear-extended shape of the striations suggests that generally when a millimetric area is engaged in contact, it stays engaged for slip distances greater than the dimension of the contact (e.g. 10-30 mm of contact duration compared to 1 mm dimension of the contact). The thickness of the wear product layers within the striations (after 30 mm of slip) is on the order of 100-200 μm (Figure 5.8).

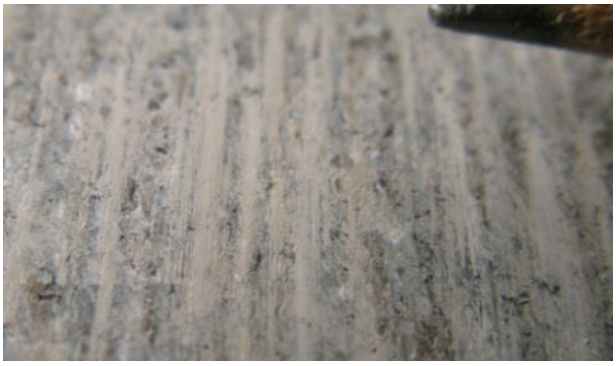

Figure 5.7: An example of striations on the sliding surface. The striations are linearly extended in the slip direction.

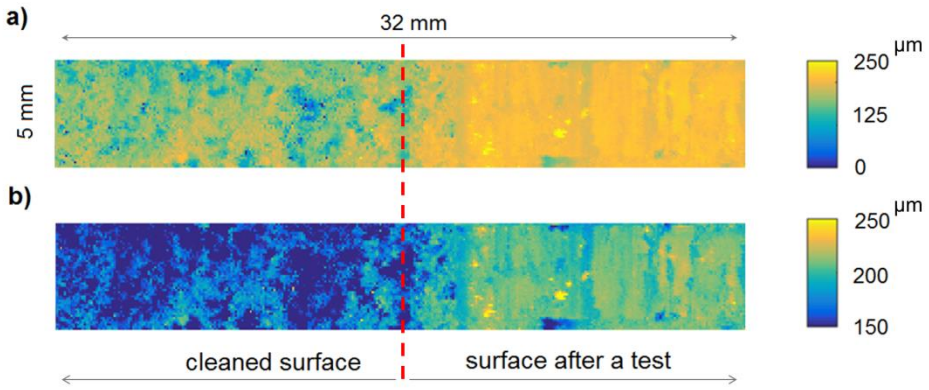

Figure 5.8: Sliding surface deformation and the thickness of the wear products within the striations. A section of the sliding surface is scanned with an optical profilometer after a sliding friction test done at 0.1 $m.s^{-1}$ under low normal stress. The wear products on the half of the section (left side) are cleaned after the experiment to compare the bare surface of the rock with the sliding surface covered with wear products (right half). Parallel linear striations can be seen in the right half of the surface while roughness of the bare surface (left side) is random and heterogeneous. Parts a and b show the same surface with different spans. The thickness of the wear material is on the order of 100-200 µm.

5.4.2 Characteristics of frictional flash heating

In order to document frictional flash heating and characterize the millimetric contact areas further, IR thermographs were captured from the sliding surface. Based on the thermographs, linear arrays of high temperature spots formed during sliding were imaged, which show high temperature streaks extended parallel to the slip direction (Figure 5.9). The IR images reflect the heating associated with frictional sliding (work done by friction, which converts to heat or thermal energy) up to the instant that the contact area is exposed to the circular window through which IR images are captured (Figure 5.9a-b). The sequential frames of the IR images represent the thermographs of the sliding surface at the emergence instant and during the cooling phase thereafter. The measurable range of temperatures using the IR camera is limited, and temperatures

higher than the Upper Limit of Measurable Temperatures (ULMT) are shown in pink, and temperatures below the Lower Limit of Measurable Temperatures (LLMT) of the IR camera are shown in dark blue. The maximum temperature in pink areas can be estimated by extrapolating temperature inside the high temperature spots based on gradient of temperature on the boundaries of the pink regions. The extrapolation method was validated by recording temperatures using different camera settings (i.e. adjusting the IR camera temperature range) of span for experiments at identical conditions.

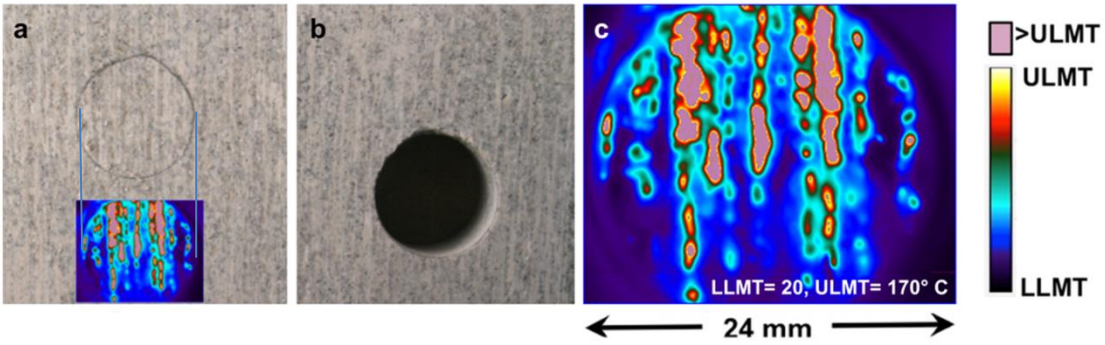

Figure 5.9: Striations and temperature distribution on the sliding surface. a) A circular area of the surface is exposed to the IR camera, b) a hollow side block is used to allow IR imaging from the sliding surface of the sample, c) an IR image captured after ~30 mm of slip at ~750 $mm.s^{-1}$ and NS of 10 MPa (#HSB-WG-129). The pink color represents areas where the contact temperature exceeds the Upper Limit of Measurable Temperatures (ULMT), and the dark blue relates to temperatures below the Lower Limit of Measurable Temperatures (LLMT) of the IR camera. The maximum T_{mm} is estimated to be 330 °C by extrapolation of temperature inside the high temperature spots based on the gradient of temperature on the boundaries of the pink areas.

The temperature distribution at millimetric scale (T_{mm}) is clearly non-uniform and the maximum temperature observed on the surface is significantly higher than the average temperature (Figure 5.9). The evident heterogeneity of temperature on the

surface demonstrates that the stress distribution on the surface is also highly non-uniform; i.e. normal and shear stresses are localized to a small portion of the sliding surface. The level of localization depends on multiple factors some of which are random and not controllable; e.g., the size and location of initial contact points at which ploughing of wear material initiates. As a result, level of localization of stress can be different from experiment to experiment, which is consistent with observations reported for meter-sized samples using strain gauges along the sample [*Yamashita et al.*, 2015].

Temperature measurements were done previously to find temperature of a sliding surface [*Han et al*., 2007; *Tisato et al*., 2012]; however, those measurements were made at the edge of rock samples and not directly on the sliding surface. Such measurements can be accurate for determining temperature after long displacements (i.e. after meters of displacement when the bulk temperature of the surface reaches to a uniform steady-state value), but cannot provide information about magnitude and distribution of transient temperature on the interface. Our IR images are directly taken from the contact surface before the mm-scale areas cool down significantly. So, a 2-D map of transient temperature, and the local NS magnitude and distribution could be indirectly obtained during initial stages of slip. In a few other studies [e.g., *Mair et al*., 2006; *Renard et al.*, 2012], IR images were taken from contact surface through a transparent halite (NaCl) sample sliding across a coarse substrate; however, sliding-rates and NS were very small (< 2 mm.s^{-1} and < 0.2 MPa respectively) and consequently temperature elevations were smaller than 0.5 °C).

5.4.3 Correlation of flash heating and sliding surface deformation

The geometric characteristics and spatial distribution of the heated areas are similar to the striations formed on the sliding surfaces. For example, dimensions of high temperature streaks are comparable to the striations. Furthermore, T_{mm} increases with slip, sliding-rate, and normal stress similar to length of the striations. Also, the high temperature streaks and striations are both spatially formed parallel to the slip direction. The correlation between the heated spots and the deformed areas was documented by mapping the high temperature regions (from the IR images) on the sliding surface exposed to the IR camera (Figure 5.10). Inspection of the sliding surface after high-speed friction tests suggests that in addition to direct contact of the bare surfaces of the intact rock sample, hot millimetric areas may be formed by bands of wear material. Accordingly, 2-D localization of contact areas can occur even when a layer of gouge material is present in between the sliding rock surfaces.

Under static loading, roughness of the surface is an important factor for defining the contact properties, but in dynamic cases, the structure of the surface changes in a few millimeter of slip and becomes less dependent on the initial roughness of the bare surface (Figure 5.8). During high-speed sliding, bands of wear material are formed, which determine the characteristics of contacts. Upon formation of a small band of wear products, local normal stress may increase and wear material can be accumulated in that area [*Yamashita et al.*, 2015] resulting in the width growth of the striations. Under high pressure and temperature, the mico- and nano- sized wear particles may weld and form cohesive regions (Figure 5.10).

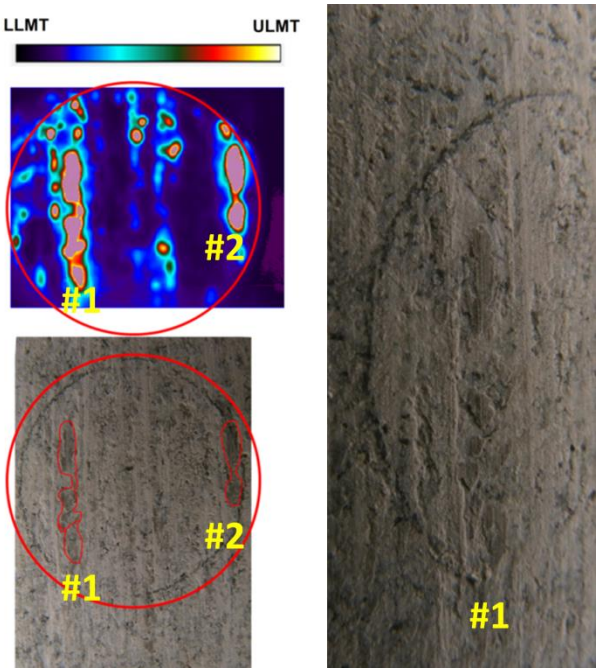

Figure 5.10: Correlation between hot areas and sliding surface structure. The IR image was captured after ~31 mm of slip at 9 MPa of NS and an average sliding rate of ~750 mm.s^{-1}; the maximum T_{mm} is estimated to be ~400 °C (LLMT= 20 °C and ULMT= 170 °C). The area with high T_{mm} has changed color and formed a semi-cohesive wear band, which can be as a result of phase transition. In the figure on the right, details of the streak #1 is shown.

5.4.4 Effect of normal stress and sliding-rate on flash heating

The thermographs show that for NS lower than 8 MPa, the millimetric temperature increases with NS significantly (Figure 5.11a-c). However, for higher NS, the maximum T_{mm} reaches a maximum limit and does not increase considerably (Figure 5.11c-d); instead, the total area of localized contact points increases (mostly due to formation of a larger number of contact points). The maximum T_{mm} also increases with the sliding-rate (Figure 5.12). The maximum millimetric temperatures observed within the first 3 cm of high-speed slip for a set of experiments done at 0.1-0.9 m.s^{-1} sliding-rate

and under NS of 0.5 to 24 MPa are shown in Figure 5.12. Data points are categorized based on sliding rate in 3 ranges of 0.1-0.15, 0.3-0.5, and 0.7-0.9 $m.s^{-1}$. The change of T_{mm} with sliding rate can be clearly observed in Figure 5.12. For example, at the NS range of 5-10 MPa, maximum T_{mm} is in average ~210, 310, and 380 °C respectively for the 3 velocity ranges of 0.1-0.15, 0.3-0.5, and 0.7-0.9 $m.s^{-1}$. Also, for the same sliding-rate, the maximum T_{mm} increases with NS; however, the rate of change reduces with NS (Figures 5.11 and 5.12). The results indicate that at moderate NS, and sliding rates of 700-900 $m.s^{-1}$, temperatures up to 500 °C are established on the surface only in ~25 mm of slip. For similar conditions, the calculated temperature in previous studies was reported to be only ~100 °C. The remarkably higher T_{mm} documented in our experiments, which is close to the weakening temperature of the material, may explain the strong dependence of weakening on NS from the initial stages of slip (Fig. 5.6). In the next sections, this is discussed further.

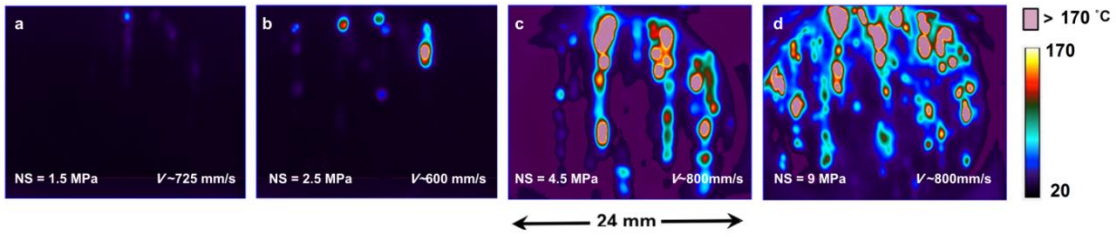

Figure 5.11: Effect of NS on temperature and contact distribution for sliding rates of 600-800 $mm.s^{-1}$. The thermographs are captured after ~25 mm of slip in 4 experiments done at 1.5 to 9 MPa of NS, respectively. At low NS, T_{max} and local NS_{max} increase significantly with NS. At higher NS, T_{max} maintains relatively unchanged, while number of contacts increase with NS. a) #HSB-WG-130, T_{max}= 70 °C, b) #HSB-WG-134, T_{max}= 280 °C (estimated), c) #HSB-WG-134, T_{max}= 380 °C (estimated), d) #HSB-WG-125, T_{max}= 400 °C (estimated).

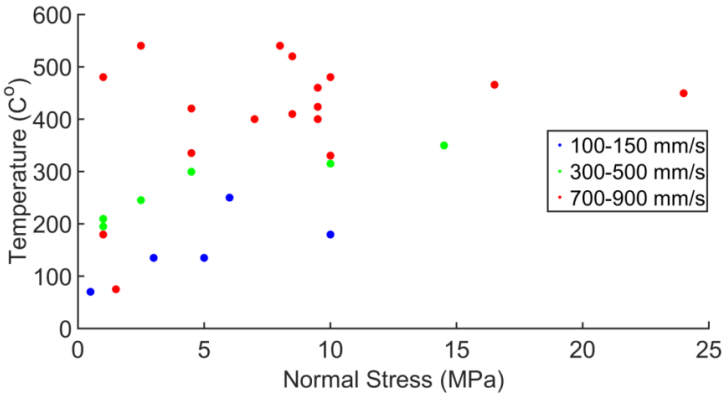

Figure 5.12: Maximum macroscopic temperatures as a function of NS. The temperatures are measured within ~3 cm of high-speed slip for experiments done at 0.5 to 24 MPa of NS and sliding-rates of 100 to 900 mm/s. Maximum T_{mm} increases with velocity and NS.

5.4.5 Flash heating at multi-scale contacts

The flash-heating of mm-scale contacts presented and described in this study, indicate that contacts are formed at multiple scales during frictional sliding. The µm-scale contacts with µsec-lifetimes support GPa normal stresses as commonly inferred in the conventional friction-contact and flash-heating models [*Rice*, 2006; *Beeler et al.*, 2008]. The mm-scale contacts with msec-lifetimes supporting MPa normal stress presumably are comprised of clusters of these µm-scale contacts. Similarly, our decimetric test-sample surfaces comprised of clusters of mm-scale contacts may well represent larger contacts on natural fault surfaces (Figure 5.13) consistent with scale-dependent roughness [*Brodsky et al.*, 2016; *Candela and Brodsky*, 2016; *Yamashita et al.*, 2015]. Characterization of natural slip-surface morphology indicates that fault roughness is scale-dependent and that load-bearing contact junctions form over a range of length scales during earthquake slip [*Power and Tullis*, 1991; *Sagy et al.*, 2007;

Brodsky et al., 2016; *Candela and Brodsky*, 2016]. Lower roughness at larger length scales can make the life-time of mm-sized contact areas several orders of magnitude longer than micro-scale contacts, which can explain the high temperature observed at mm-scale despite the lower heat generation rate (heat generation is lower due to smaller shear strength at larger length scales) compared to that in micro-scale.

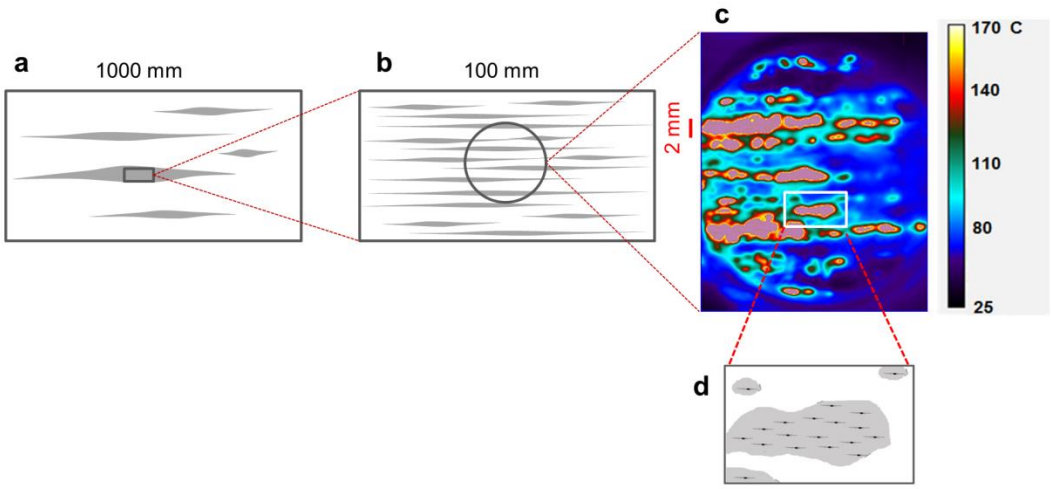

Figure 5.13: Multi-scale of contacts for rock material. a) large striations are observed on meter-sized rock samples [*Yamashita et al.*, 2015]; heterogeneity of contacts increases with size of the sliding rock, b) striations with millimetric width cover the surface of our decimetric samples, the larger striations on meter-sized samples can be formed from these millimetric striations [*Yamashita et al*., 2015], c) an IR image of the rock sliding surface, the areas with pink color have temperatures higher than 170 °C, d) millimetric striations are formed from a cluster of micro asperities. The micro-asperities themselves can be formed by cluster of nono-particles (extrapolating the observations to smaller length scales).

The heterogeneity of contact areas is higher at larger scales based on friction experiments done on meter-sized samples [*Yamashita et al.,* 2015], i.e. lower number of major striations are present, but their width can be on the order of several cm with decimetric lengths (Figure 5.13a). Each of these major striations can be formed by several smaller striations with millimetric width. Such narrow striations are seen on cm-sized samples, which may cover the whole surface of the sample (Figures 5.7, 5.9a-b and 5.13b-c). Although heterogeneity is less at cm-scale compared to meter-sized samples, still localization of normal and shear stress can be clearly observed from the IR temperature measurements. The millimetric contact areas are formed from a cluster of microscopic contacts (Figure 5.13d). By extrapolating these observations to smaller length scales, it can be expected that the micro-asperities themselves may be formed by clusters of nano-particles. Presence of nanoparticles on the sliding surface after high-speed experiments has been reported in numerous studies, some of which have ruled out flash-heating as the cause of dynamic weakening based on this observation. The reason for ruling out flash weakening as primary friction weakening mechanism is that D_a is very small for nano-particles. The temperature rise based on classic flash weakening model for such a short duration of contact is very low, i.e. very high sliding rates are required to initiate weakening (Equation 1.9). However, based on our observation, micro- and nano- scale asperities can form clusters in millimetric areas, where temperature stays high for milliseconds (compared to micro- or nano-seconds life time of asperities). As a result, based on the presented multi-scale flash-heating, flash-

weakening can still be the dominant weakening mechanism, even when the surface is covered with nano-particles.

5. 5 Millimetric contact characterization and normal stress

5.5.1 Local normal stress at contacts

Temperature measurements are used to estimate the Local Normal Stress (LNS) at the millimetric scale. Maximum T_{mm} in each experiment (Figure 5.12) is an indication of the maximum local NS in mm-scale, and since the thermal properties of rock and the magnitude of high-speed slip distance were the same for the experiments, the maximum T_{mm} is controlled by the heat generation-rate per unit of area ($\mathrm{LNS}\times\mu\times V$). For a fast moving heat source, the maximum local NS can be estimated by considering a 1-D heat transfer relation [*Jaeger*, 1942; *Archard*, 1959; *Greenwood*, 1991]. For high sliding rates, a 1-D model provides accurate estimations because the depth of diffusion is much smaller than the dimensions of the contact area that is heated [*Jaeger*, 1942; *Archard*, 1959; *Greenwood*, 1991]. As a result, lateral diffusion is negligible compared to heat diffusion into the solid. Based on the 1-D heat conduction model, the normal stress can be calculated as follows [*Jaeger*, 1942; *Archard*, 1959; *Greenwood*, 1991]:

$$\mathrm{LNS}_{\max} = \frac{K_{th}\Delta T_{max}\sqrt{\pi/\alpha t}}{\mu V} \tag{5.1}$$

where, t is duration of actively being in contact, and μ is the average friction during t. Similar to micro-scale asperities, a characteristic length of in-contact slip can be defined for millimetric localized areas. However, contrary to microscopic contacts, for which

distance of contact duration is assumed equal to contact dimension (D_a), the contact duration for millimetric areas is not necessarily equal to the dimension of the contact and can be longer (e.g. ~10-30 mm based on the surface striations and the IR images). Defining D_{mm} as the average length of slip for which contact exists, the life-time of a millimetric contact can be obtained as:

$$t = \frac{D_{mm}}{V} \tag{5.2}$$

Assuming that the thermal properties of rock and D_{mm} are independent of temperature, NS and V; and by substituting Equation 5.2 in 5.1, LNS_{max} is found to be proportional to $\Delta T_{max}/(\mu.\sqrt{V})$. The maximum millimetric LNS is proportional to NS at low NS (< 8 MPa); but that LNS_{max} does not change noticeably with further increase in macroscopic NS (Figure 5.14). The LNS_{max} magnitudes were obtained based on maximum T_{mm} measurements for many experiments (Figure 5.12) assuming D_{mm} = 20 mm, K_{th} = 2.64 J.(s.K.m)$^{-1}$, α = 1.25 $\times 10^{-6}$ m^2.s^{-1} (Figure 5.14). Existence of an upper limit for maximum temperature suggests that the maximum millimetric LNS is bounded. This is consistent with the finding that the magnitude of weakening is controlled by NS more significantly at low NS (Figure 5.6). Also, comparing Figure 5.12 and 5.14 indicates that the LNS is independent of sliding-rate. The upper limit for the LNS may be related to the strength of the granite contacts at the millimetric scale.

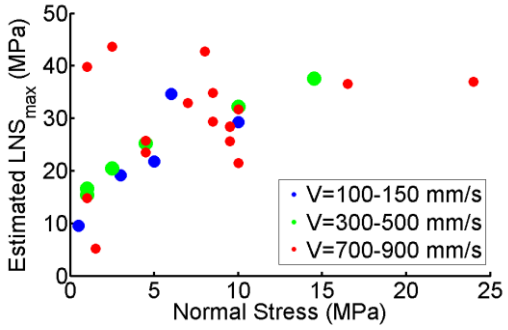

Figure 5.14: Maximum Local-NS (LNS) versus NS. LNS_{max} is estimated from the maximum temperature recorded during the full stroke of the experiments in three velocity intervals (maximum temperatures were presented in Figure 5.12).

5.5.2 Contact distributions with normal stress

A maximum LNS limit suggests that, for cm sized unconfined granite rock samples, plastic yielding occurs locally in some of the millimetric contact areas. Therefore, if macroscopic NS is increased further, a greater number of contact points and/or larger size contacts should develop to carry the extra load. The effect of NS on size and distribution of millimetric contacts is determined for the sliding experiments conducted at 600-800 mm.s^{-1} by image analysis of the thermographs. For this purpose, a reference temperature (T_{ref}) is defined to distinguish the area of contacts (i.e. each pixel was considered to be in contact only if $T > T_{ref}$). The maximum temperature observed in the experiments was ~500° C, and a reference temperature of T_{ref} = 180±10 °C was selected in order to best compare results from low to high NS tests. In order to minimize temperature measurement errors associated with cooling of the contact once the surface emerges and becomes exposed to the IR camera, image sequences from each experiment were post-processed frame by frame analyzing only the portion the sliding surface in

each thermograph exposed from the preceding thermograph, i.e., the portion of the surface exposed each 3.3 msec of high-speed slip.

The distribution of contact areas with $T > T_{ref}$ for all the experiments conducted at NS of 1-10 MPa were analyzed (Figure 5.15). Velocity and slip distance are similar for the different experiments, and sizes of areas are found by averaging the values during the last 4 frames of IR images (i.e. during final ~10 mm of high-speed slip). The results indicate that, overall, the number of millimetric contact increases as macroscopic NS is increased (Figure 5.15a), which is consistent with the existence of an upper limit on millimetric LNS. As macroscopic NS is increased, contact areas yield to form larger contact areas. The growth of contact areas as a function of NS is determined also by comparing the width of the largest striation (thermal streak) observed in the images during each experiment. The width of striations grows with NS at low NS, and a maximum width of a single striation of 2.5 mm is developed in ~25 mm of high-speed slip (Figure 5.15b). These data show that the total area of contact on the surface increases with NS, due to the increase in number of millimetric contact areas and also growth of striations with NS (Figure 5.15c). Heterogeneity in the size of contact areas also is controlled by NS. Herein, heterogeneity of contact areas is defined as $HTG = \sum(S_i)^2/(\sum S_i)^2$, where S_i is size of ith contact area. With this definition, if there is a significant difference in size of contact areas, *HTG* will be determined primarily by the area with the maximum S_i; e.g. if there is a very large contact area and several small areas, *HTG* would then approach 1. On the other hand, if the total area of contact consists of many isometric contact areas, *HTG* then approaches zero. The decrease in

heterogeneity of contacts shown in Figure 5.15d indicates that the rate of increase in number of contacts is higher than the rate of growth of contacts with NS. This suggests that the stress distribution becomes more homogenous with NS because increasingly more area is yielding at the LNS_{max} value.

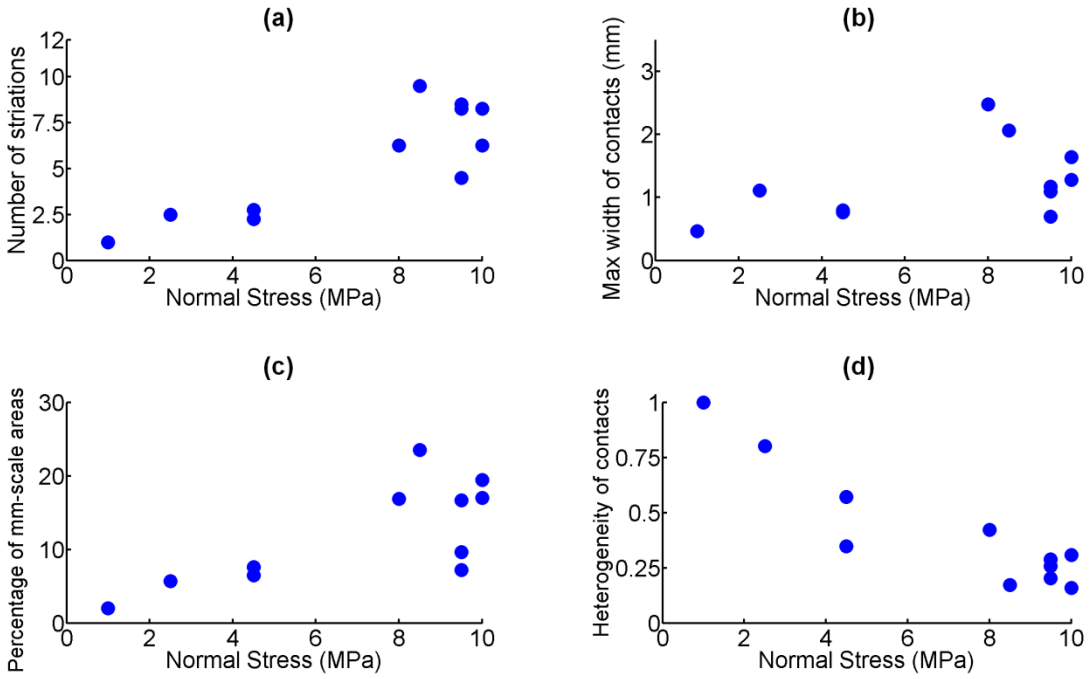

Figure 5.15: The effects of NS on millimetric contact areas. The results are based on experiments conducted at sliding rates of 600-800 $mm.s^{-1}$ and NS of 1-10 MPa. The mm-scale areas with T > 180 °C are counted as contact areas. The reported values are measured and averaged during the last 10 mm of high-speed slip. Data points are scattered partly because the images are taken from a small portion of the sliding surface (22 mm wide window); a) number of striations versus NS; b) width of the largest striations versus NS; c) percentage of areas with T > 180 ° C relative to total area of contact versus NS; d) Heterogeneity of contact areas (*HTG*) as a function of NS.

5.5.3 Characteristics of dynamic millimetric contacts relative to static microscopic contacts

Employing special imaging techniques, the geometry of micro-scale contacts has been investigated for some transparent solids (analogous to rock) [*Dieterich and Kilgore*, 1994, 1996]. These observations are mostly done under static normal loading, or at quasi-static sliding rates. An example of an image of microscopic-scale contact presented in [*Dieterich and Kilgore*, 1994] shows that the total true area of contact is a very small portion of the apparent contact area, and the contact area consists of numerous individual microscopic contacts (Figure 5.16). If normal force is carried only by the microscopic contacts spread over the apparent area of contact, as typically assumed in models of rock friction, then NS is uniform over cm-sized rock samples in the laboratory experiments. Although, it appears this assumption may be valid for static loading of laboratory rock samples, the thermographic imaging demonstrates that contact characteristics can be different at dynamic sliding-rates. The size and number of microscopic contacts increase with NS (Figure 5.17) similar to millimetric contacts (Figure 5.15). However, the rate of growth of contacts is lower than the rate of increase in number of contacts (Figure 5.17). As a result, similar to mm-scale contacts, heterogeneity of contacts reduces with NS due to formation of new contacts (Figure 5.17d).

At high-sliding rates, wear rate is high and accumulation of wear material can redefine the characteristics of contacts and surface structure at larger length. Nonetheless, the dynamic and static contacts are similar in that the number of contacts

increases with NS (Figure 5.17). The contacts cannot carry a load higher than the strength of material at that scale, and new contacts are made to carry the extra load. For microscopic contacts (micrometer diameter), strength is on order of several GPa, but at the millimetric scale, the yield strength of contact is on the order of tens of MPa, consistent with a dependence of strength on scale.

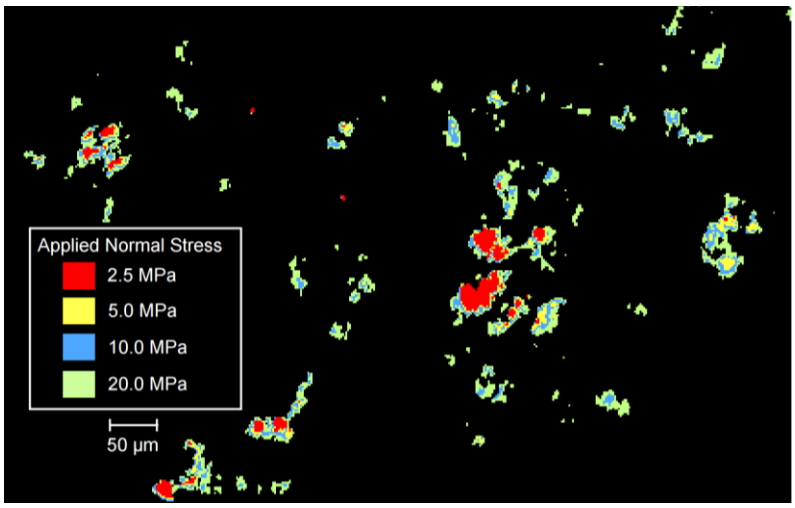

Figure 5.16: Effect of NS on size and distribution of microscopic contact areas.The figure is reprinted with permission from "Direct observation of frictional contacts: New insights for state-dependent properties" by Dieterich, J. H., and B. D. Kilgore, 1994. *Pure and Applied Geophysics, 143*(1-3), 283-302, Copyright [1994] by Springer.

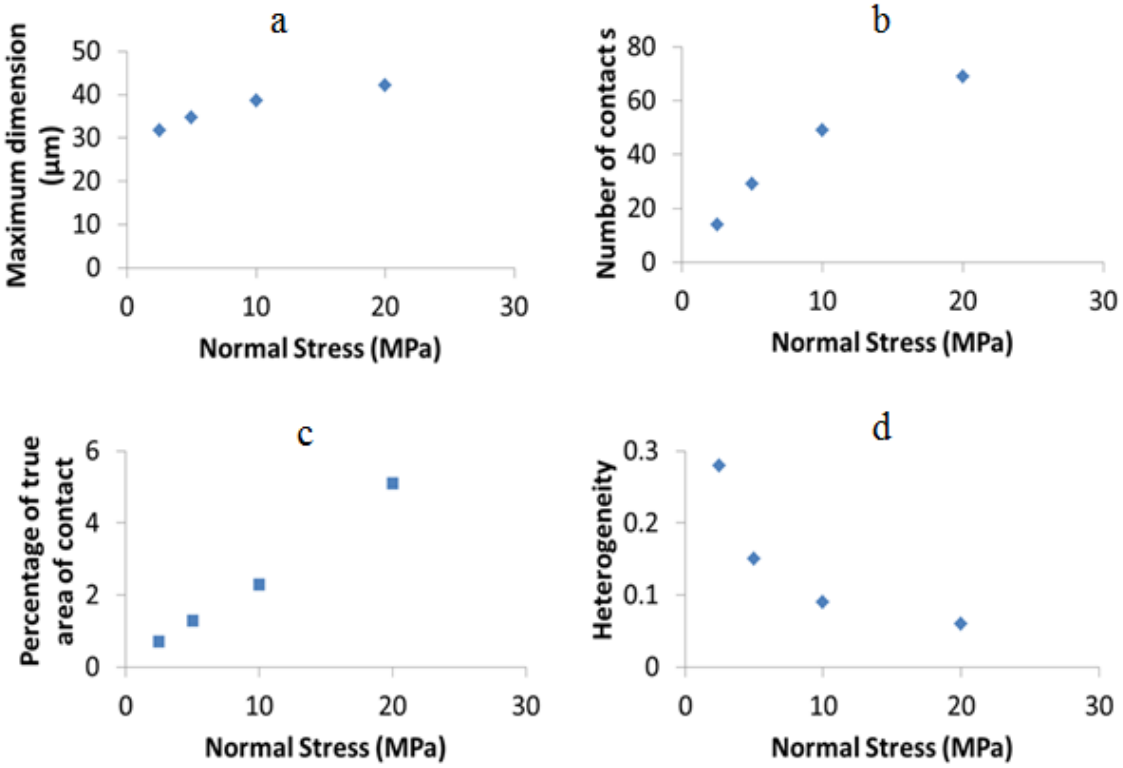

Figure 5.17: Effect of NS on characteristics of microscopic contact areas. a) Number of microscopic contact areas versus NS, b) maximum size of microscopic contact areas versus NS, c) true area of contact versus NS, d) heterogeneity of contacts decreases with NS.

5. 6 Investigation of NS effect on multi-scale contacts and weakening

Yao et al. [2016a, 2016b] showed that dynamic weakening is mainly controlled thermally by flash heating, and other mechanisms such as nano-powder lubrication, which cannot cause dramatic weakening alone. Since the HSB can achieve high accelerations, it could be observed that a major part of weakening occurs in distances as low as 1 mm (concurrently with the rise in velocity) at high normal stresses (Figures 5.2, 5.3, and 5.5). Such an instantaneous weakening suggests that the weakening mechanism

is flash weakening. Furthermore, the flash-weakening curve fits well with the experimental data for NS > 8 MPa (Figure 5.4). However, at low NS, the amount of instantaneous weakening was significantly below what the flash-weakening model predicts (Figure 5.5 and 5.6), and the weakening distance was remarkably longer compared to the experiments with high NS (Figure 5.5). Therefore, in contradiction with the classic flash-weakening model, NS was found to be an important parameter in weakening in our experiments. The question that arises is: How can the influence of NS be taken into account in the flash-weakening model?

The effect of macroscopic NS on microscopic flash-heating is often studied by assuming a constant number of microscopic contacts, for which, the area of contact increases with NS [e.g., *Brantut and Platt,* 2016]. Based on this assumption, dimension of microscopic contacts, D_a, increases with NS, which reduces V_w (Equation 1.9) and consequently enhances flash weakening (Equation 1.12). Currently, we cannot measure the size of microscopic contacts from IR images because: (1) the resolution of our IR images is 75 μm ($> D_a$), (2) the maximum frame rate is 300 frames/sec and images are captured each 3.3 msec. Although temperature does not change dramatically in millimetric areas in 3.3 msec, micro-scale flash temperature of contacts decays quickly due to small volume of microscopic contacts. Therefore, temperature cannot be measured at micro-scale contacts with our instruments. Herein, to investigate the effect of NS on D_a, we analyze Figure 5.16 which was presented by *Dieterich and Kilgore* [1994]. The effect of NS on size and number of contacts was analyzed using Figure 5.17. Figure 5.17c shows that when NS is 2.5 MPa, the true area of contact is 0.7% of the

apparent area. As NS is increased to 20 MPa, the total contact area is increased to 5.1%; however, the increase is not only due to the growth of the contacts, but new contacts are also formed (Figure 5.17a). Comparing contact areas at 2.5 and 20 MPa, one can conclude that a large portion of the new contacts (formed at 20 MPa) have smaller dimensions than the initial average D_a at 2.5 MPa. Therefore, it should be investigated if D_a, on average, increases with NS at all. To study flash-weakening for a group of contacts with different dimensions, first, the effective average dimension of microscopic contacts that it is used in Equation 1.9 should be obtained. In general, the average friction can be obtained as follows:

$$\mu_{avg} = \frac{F_{shear}}{F_{normal}} \tag{5.3}$$

where, F_{shear} is the shear force on the sliding surface and F_{norm} is the normal force,

$$F_{shear} = \sum \left(\mu_i \times \sigma_n \times S_i \right) \tag{5.4}$$

In Equation 5.4, σ_n is the NS, S_i is the contact area size of the ith contact and S_T is the total true area of contact. Since, D_a is different for different contacts, each asperity has its local coefficient of friction, μ_i. The normal force can also be written as:

$$F_{normal} = \sigma_n S_T \tag{5.5}$$

Substituting Equation 5.4-5.5 in Equation 5.3, we may write:

$$\mu_{avg} = \sum\left(\mu_i \times \frac{S_i}{S_T} \right) \tag{5.6}$$

Coefficient of friction in each contact area can be found using Equation 1.12, as follows:

$$\mu_i = \mu_w + (\mu_s - \mu_w)\frac{V_{wi}}{V} \tag{5.7}$$

where, V_{wi} is the weakening velocity for ith contact. Assuming all the conditions are identical for the contacts except for the dimension, V_{wi} can be found as follows:

$$V_{wi} = \frac{\phi(T)}{D_{ai}} \tag{5.8}$$

Substituting Equation 5.7 and 5.8 in Equation 5.6, we obtain:

$$\mu_{avg} = \mu_w \sum\frac{S_i}{S_T} + (\mu_s - \mu_w)\frac{\phi(T)}{V}\sum\frac{1}{D_{ai}} \times \frac{S_i}{S_T} \tag{5.9}$$

The flash weakening formulation is derived assuming square contacts, therefore, $S_i = D_{ai}^2$; accordingly, μ_{avg} can be found as follows:

$$\mu_{avg} = \mu_w + (\mu_s - \mu_w)\frac{\phi(T)}{V}\sum\frac{\sqrt{S_i}}{S_T} \tag{5.10}$$

By comparing Equation 5.10 with Equation 1.9 and 1.12, the average effective contact dimension can be found as follows:

$$D_{a-eff} = \frac{S_T}{\sum\sqrt{S_i}} \tag{5.11}$$

To study the effect of NS on $D_{a\text{-}eff}$, the contact areas in Figure 5.16 were analyzed. As shown in Figure 5.18, the growth of contact areas observed in static normal loading does not have a significant net effect on $D_{a\text{-}eff}$, and may not be the reason for enhancement of flash weakening with NS.

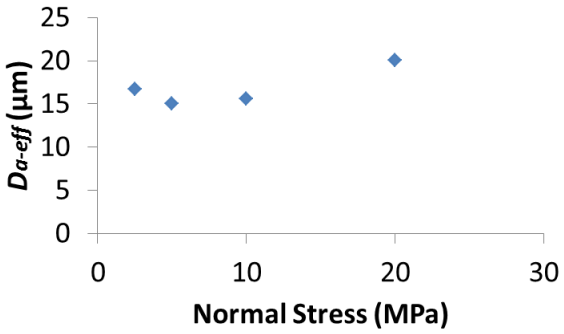

Figure 5.18: Effective average dimension of microscopic contacts as a function of macroscopic NS.

Therefore, if the increase in D_a does not explain the dependence of weakening on NS, how can it be explained? Our thermal measurements showed that, NS can control T_{mm}. On the other hand, in a few mm of slip, T_{mm} can rise to temperatures comparable to weakening temperature of rock. Such a sharp rise in T_{mm} can enhance weakening by: (1) enhancement of microscopic flash weakening, (2) activation of parallel weakening mechanisms in the millimetric scale. These two phenomena are elaborated and investigated in Chapter VI. In addition to direct effect of temperature on weakening, localization of stress in millimetric areas may also influence flash-weakening. A large portion of contact points (at mm- and micro-scales) may not undergo pure plastic

deformation at low NS. However, in the flash weakening model, it is assumed that all the microscopic contacts are under yield stress. In numerous studies, the deformation at micro-contacts is proposed to be elastic-plastic and/or visco-elastic rather than pure plastic [e.g., *Greenwood and Williamson*, 1966; *Hulikal, et al*., 2015]. Also, a lower finite limit may exist for the minimum possible contact area during slip [*Bar-Sinai et al*., 2015] and such area will be completely in contact even at very low NS (elastic deformation). As NS increases, the assumptions of flash weakening model become valid since the contact points undergo plastic deformation and micro-contacts can reach the full material strength. This is observed for mm-scale contact areas in our experiments. For NS < 8 MPa, maximum T_{mm} increases with NS, which shows that local NS has not reached its maximum value (Figure 5.14), and deformation is a combination of elastic and plastic deformation of the contacts. Similarly, at low NS, shear stress at microscopic contacts (τ_c in Equation 1.9) can be lower than the yield stress of material. Therefore, shear stress and heat generation rate in flash weakening model can increase with NS for low to moderate NS. Based on Figure 5.14, at NS of ~10 MPa, LNS reaches a maximum cap of ~ 40 MPa which can be analogous to the mm-scale yield strength of the rock material in unconfined condition. For higher NS (> 10 MPa), new mm contacts are made, but maximum local NS does not increase further with NS. As a result, for high NS, the results are consistent with the flash weakening model assumption stating that the NS at the microscopic contacts is constant and independent of the average macro-scale NS (consistent with Figure 5.6). However, even for NS > 10 MPa, weakening continues

to be enhanced with NS (at lower rate compared to NS < 10 MPa), as mean surface temperature increases and a higher portion of contact areas reaches saturated condition.

5. 7 Scale dependence of contacts

By conducting experiments on meter-sized rock samples under moderate NS (~7 MPa), *Yamashita et al*. [2015] showed that stress localization enhances with scale (stress localization was found to be one order of magnitude higher than that in cm-sized samples). On the other hand, our results show that heterogeneity of contacts decreases with NS due to reaching the maximum local strength of material in millimetric areas and formation of new contacts. Therefore, size and NS have opposite effects on localization of stress and heterogeneity of contacts. Since in natural faults, both size and NS are higher than the experiments done in the laboratory experiments, one question that requires further investigation is how the level of heterogeneity in natural faults differs from the observations made in the laboratory. Based on Mohr Coulomb criteria, due to high confining pressure at 10 km depth (P_c = 250 MPa), the maximum strength in millimetic scale may be ~600-800 MPa. This implies that the localization of stress may result in local NS of ~3 times higher than the macroscopic NS (600-800 MPa versus 250 MPa). This level of stress heterogeneity is close to what was observed at NS of 8-10 MPa on 50 × 75 mm^2 samples.

CHAPTER VI

MULTISCALE FLASH WEAKENING IN ROCK; EXPERIMENTAL AND MODEL ANALYSIS

6. 1 Introduction

In Chapter V, it was shown that during high-speed frictional slip, contacts are formed in multiple time- and length- scales. The thermographs showed that temperature distribution is remarkably heterogeneous on the sliding surface, and temperatures significantly higher than the average temperature of surface (up to 500 °C in ~25 mm of slip) can be achieved due to localization of stress in millimetric sized areas. The rapid rise of temperature in millimetric scale (~200 °C in the first 2-3 mm of slip) can enhance flash weakening from early stages of the transient friction in two ways: (1) enhancement of microscopic flash weakening, (2) initiation of a parallel weakening mechanism in millimetric scale. In this chapter, the effect of multi-scale flash heating on the transient friction is studied, and a model is developed to predict the transient weakening and healing behavior of rock material under different velocity paths. The model represents the slip- and velocity- dependence of the transient friction and provides a powerful tool for understanding nucleation and propagation of earthquake ruptures and recovery of strength during and after deceleration of seismic slips.

6. 2 Models of frictional flash weakening

6.2.1 Classic flash weakening model

It is widely recognized that rapid frictional heating (flash-heating) of faults during earthquakes can initiate dramatic weakening by several different processes, and of these, melt-lubrication and flash-weakening have been well documented through experimentation [e.g., *Goldsby and Tullis*, 2011; *Passelègue et al.*, 2014; *Di Tor. et al*., 2011; *Proctor et al.*, 2014; *Spagnuolo, et al.*, 2015; *Yao et al.*, 2015a, 2015b; *Niemeijer et al.*, 2011; *Di Toro et al*., 2004]. Flash heating can activate weakening mechanisms (e.g., micro-scale melting, phase transition, and chemical decomposition [*Proctor et al*., 2014; *Green II et al*., 2015; *Tisato et al*., 2012; *Niemeijer et al*., 2012; *Brantut et al.*, 2016]) at very small displacements once slip velocity V exceeds the weakening velocity, $Vw \approx 0.1$ m.s^{-1}, and thus has particular significance in the early stages of seismic slip. The classic model of flash weakening at microscopic asperities was presented in Chapter I. The two main governing equations of flash-weakening are re-stated below:

$$\begin{aligned} \mu(V) &= \mu_w + (\mu_0 - \mu_w)\frac{V_w}{V} && \text{if } V > V_w \\ \mu(V) &= \mu_0 && \text{if } V \le V_w \end{aligned} \tag{6.1}$$

where,

$$V_w = \frac{\pi K_{th} \rho c_{th}}{D_a}\left(\frac{T_w - T_{c0}}{\tau_c}\right)^2 \tag{6.2}$$

6.2.2 Flash weakening model with evolving average surface temperature

In the original flash weakening model, the slip-dependence of friction is not included. However, it is known that the temperature of surface (T_s) evolves with slip, which changes the initial temperature of the microscopic asperities (i.e., T_{c0} in Equation 6.2 is equal to T_s). As the surface temperature increases, $\Delta T=T_w-T_s$ decreases and consequently V_w reduces. Based on Equation 6.1, flash weakening enhances as V_w decreases. Enhancement of flash weakening of microscopic asperities with surface bulk temperature was proposed by [*Proctor et al.*, 2014; *Yao et al.*, 2016a and 2016b; *Elbanna and Carlson*, 2014]. Given the velocity and shear stress history, T_s can be calculated using a 1-D heat conduction formulation. The governing equation of heat transfer for 1-D conduction (for a semi-infinite plate) is [*Carslaw and Jaeger*, 1959] as follows:

$$\frac{\partial T}{\partial t}=\alpha\frac{\partial^2 T}{\partial x^2},\quad \alpha=\frac{K_{th}}{\rho c_{th}} \tag{6.3}$$

where, $T(x,t)$ is the transient temperature, x is distance from the surface into the solid, and α is heat diffusivity of the solid which is defined as a function of K_{th} (heat conductivity, c_{th} (specific heat capacity), and ρ (density of solid). Assuming that the changes of the thermal properties of material (K_{th}, c_{th}, ρ) with temperature (T) do not affect the solution significantly, the closed-form analytic solution of Equation 6.3 has been developed for certain boundary conditions [*Carslaw and Jaeger*, 1959]. For

example, for a semi-infinite domain if the heat source is uniform and the heat generation rate, f*(t)*, is only a function of time (but not *T*), i.e.:

$$\frac{\partial T(0,t)}{\partial x} = -K_{th}\, \mathrm{f}(t) \tag{6.4}$$

then the following solution can be used to calculate temperature at $x = 0$, T_s [*Carslaw and Jaeger*, 1959; *Proctor et al.*, 2014]:

$$T_{surface} = \sqrt{\frac{1}{\pi K_{th} \rho c_{th}}} \int_0^t \left(\frac{\mathrm{f}(t')}{t - t'} \right) dt' \tag{6.5}$$

$$\mathrm{f}(t) = \frac{\tau(t) V(t)}{2} \tag{6.6}$$

6.2.3 Forward model with coupled heterogeneous temperature and friction

In the previous studies, temperature distribution was assumed to be uniform on the sliding surface. Our results, presented in Chapter V, showed that due to the non-uniform stress distribution on the surface, temperature in millimetric contact areas can be remarkably higher than the average temperature of surface. The thermographs show that at V = 800 mm.s^{-1} and moderate NS (~8 MPa), the maximum temperature of contact areas may rise by 400-500 °C in a short displacement (~10-30 mm), whereas the average temperature of surface is calculated to rise only by ~100 °C over the 30 mm of high-speed slip assuming a uniform stress distribution. The micro-asperities nested in hot millimetric spots may go in contact periodically, or as the flash weakening model suggests, may exist for only one lifetime (i.e. new asperities replace them). Regardless,

the important finding is that micro-asperities within a millimetric contact may engage while their initial temperature is significantly higher than the average surface temperature. Although, still the average temperature of the surface would be the same as calculated for a uniform stress distribution, the millimetric areas with higher temperature are under higher shear stress (i.e. carry a relatively larger portion of the total load), and thus, have a higher influence on the average coefficient of friction. As a result, based on Equation 6.2, V_w can be much lower in the hot millimetric contact areas, and consequently, the transient friction can be different from what has been predicted by the previous models assuming uniform stress distribution.

Moreover, the solution to the heat conduction problem (Equation 6.5 and Equation 6.6), used in previous works, is valid if $\tau(t)$ is only a function of time and not temperature. Therefore, in previous models, shear stress measurements during the experiment, $\tau(t)$, were used as an input of Equations 6.5-6.6 to calculate T_s [e.g., *Proctor et al.*, 2014; *Yao et al.*, 2016a, 2016b; *Elbanna and Carlson*, 2014]. However, the purpose of calculating T_s is to eventually obtain the transient friction. In such a method, first, friction is measured during the experiment; next, friction data is used to find the transient temperature of the surface, and then the temperature calculation is used as an input to the model to estimate friction; i.e., measured friction is indirectly used to estimate friction.

In this study, a forward model is developed that does not require experimental data of friction as an input, and is able to predict the transient friction and temperature only by inputting the velocity history as boundary condition. For this purpose, we

consider the solution of Equation 6.3 for a more general boundary condition, where heat generation rate can be a function of both time and temperature, ($\tau(T,t)\cdot V(t)/2$). In this way, the coupled effects of temperature and friction are embedded in the model. The solution for the Partial Differential Equations (PDE) of heat transfer (Equation 6.3) with a temperature-dependent boundary condition can be found numerically using the MATLAB PDE solver, *pdepe*. The *pdepe* solver converts the PDEs to Ordinary Differential Equations (ODEs) by spatial discretization of the region using the user-specified nodes [*Skeel and Berzins*, 1990], and solves the heat transfer equation with the following boundary condition:

$$\frac{\partial T(0,t)}{\partial x} = -K_{th}.\mathrm{g}(T,t) \tag{6.7}$$

$$\mathrm{g}(T,t) = \frac{\tau(T,t)\cdot V(t)}{2} \tag{6.8}$$

The forward method, presented herein, not only does not require friction measurement data as an input, but also, can take into account the effect of heterogeneity of stress on friction. Due to heterogeneity of stress on the surface, the heat generation rate is not uniform on the sliding surfaces. In addition, areas with different temperatures exhibit different transient friction behavior, and heat generation rate cannot be scaled linearly with the average friction measured during the experiment. The coupled relation between temperature and friction is included in the forward model to address this problem.

6. 3 Implementing the multiscale flash heating model

6.3.1 Method

The thermographs clearly demonstrate that a non-uniform temperature distribution develops on the surfaces during high-speed sliding (Figure 6.1). In general, the distribution is characterized by large temperature rise within 1-2 mm diameter spots that are often organized in spaced, linear-arrays parallel to the sliding direction. IR images reveal that heating at high velocity is very rapid by which temperatures above 170 °C are established after the first 2-3 mm slip (equivalent to the spot size), and clearly representing flash-heating at the mm-scale (Figure 6.1a). Based on the IR images, temperature of the millimetric areas increases with slip (Figure 6.1a). After ~30 mm of slip at 800 $mm.s^{-1}$ and moderate NS, the sliding surface is covered with areas that have temperatures from 20 to 500 °C. This range of temperature was divided into 6 intervals with mean temperatures of: 37, 70, 140, 250, 350, 450 °C. Using these temperature intervals, the contact areas are discretized to sub-areas. In each sub-area, temperature is estimated by a uniform temperature equal to the mean value of temperature in that interval. The temperature history in i^{th} sub-area is referred to as T_i. The local NS associated with each sub-area can be estimated based on the temperature rise in the sub-area. Normal Stress Ratio (NSRi) is defined and used to determine the ratio between local NS of i^{th} sub-area to the average macroscopic NS. Area Portion (AP) is another characteristic parameter of each sub-area. AP_i indicates what percentage of the surface is under Local-NS_i ($LNS_i = NSR_i \times NS$). AP_i is obtained based on the above representative temperatures (T_i) for a number of experiments done at 0.8 $m.s^{-1}$ slip rate under moderate

NS (~8 MPa). Figure 6.1b shows three experiments conducted at similar conditions using several different camera settings of span, and with and without the neutral density filter to measure percentage of areas corresponding to each interval of temperature from 20 to 500 °C. For the 6 sub-areas mentioned above with mean temperatures of 37, 70, 140, 250, 350, 450 °C, AP_i was estimated as 37, 24, 18, 13.5, 5, and 2.5% of the total contact surface, respectively.

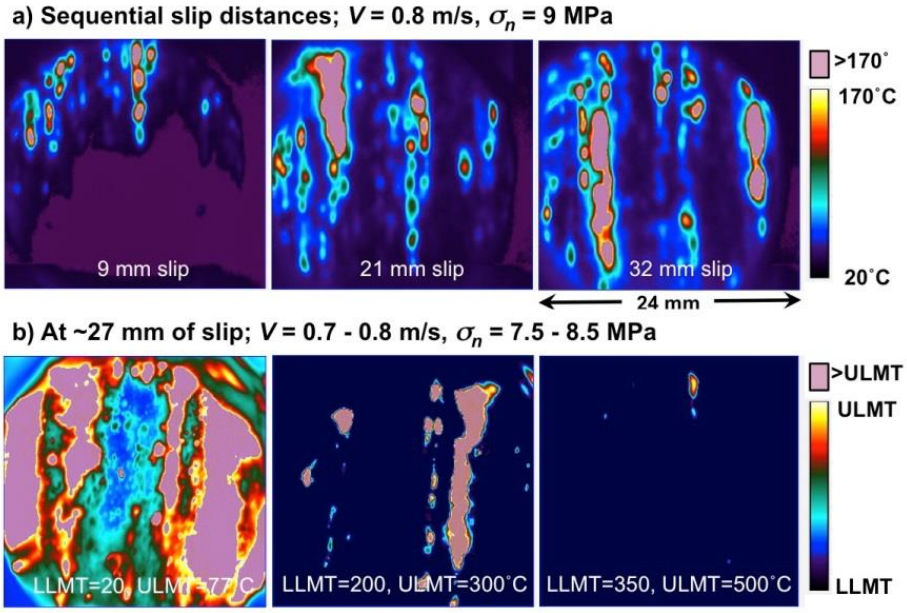

Figure 6.1: Examples of IR thermographs. The images show the distribution of temperature on sliding surfaces as a function of slip distance for sliding at high velocity and moderate NS. a) Images captured at slip distances of 9, 21, and 32 mm during high-speed sliding in a single experiment. Maximum temperature of millimetric areas increases with slip. Camera was set to measure temperatures over the range 20-170 °C. b) IR images captured at 27 mm of high-speed slip from three different experiments on the same sample blocks. The three experiments were conducted at similar conditions of velocity and NS, but at different camera settings to record temperature conditions over the ranges of 20-77 °C, 200-300 °C, and 350-500 °C. Temperature is represented by the color within the range LLMT (Lower Limit of Measurable Temperatures) to ULMT (Upper Limit of Measurable Temperature) as indicated in the color scale on the right side of the image sequences; areas that exceed the ULMT are shown by the pink color.

To calculate the average macroscopic friction magnitude, first, we need to find friction in each sub-area (μ_i). Figure 6.2 illustrates how the temperature rise in each sub-area (T_i) enhances flash weakening at microscopic contacts by decreasing T_w-T_i (T_w-T_{c0} in Equation 6.2). Based on the micro-scale flash weakening model, if $V > V_w$, temperature at microscopic contacts reaches T_w before the end of micro-asperity engagement (4 μm), and micro-scale shear strength (τ_c) drops from τ_{c0} to τ_{cw} leading to a decrease in the average friction. The earlier τ_{c0} drops to τ_{cw} in the lifetime of the asperities, the lower the average friction is (a larger portion of the lifetime is at the weakened state). Therefore, in addition to instantaneous velocity, slip history of the contact area can have a significant influence on weakening by the direct effect of velocity on T_i.

The average value of macroscopic friction (μ_{avg}) is equal to the summation of shear loads acting on individual sub-areas divided by the total normal force acting on the surface:

$$\mu_{avg} = \sum_{i=1}^{i=6} \frac{\mu_i \times (AP_i \times A_{interface}) \times NSR_i \times NS(t)}{NS(t) \times A_{interface}} \tag{6.9}$$

$$\mu_{avg} = \sum_{i=1}^{i=6} \mu_i \times AP_i \times NSR_i \tag{6.10}$$

Therefore, in addition to relative size of the sub-areas (AP_i), the NSR_i determines how the average friction is affected by local friction in i^{th} sub-area.

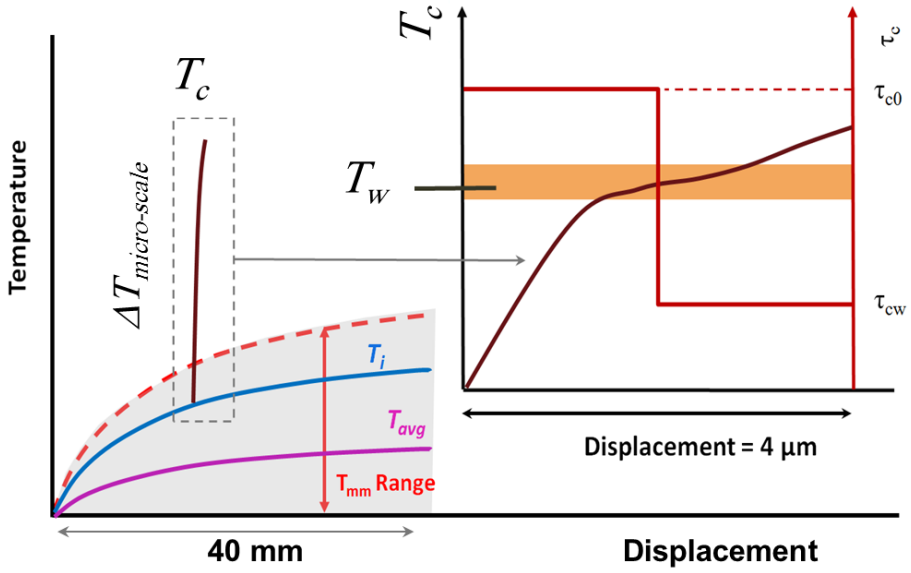

Figure 6.2: Schematic diagram of multi-scale flash-heating and weakening. Temperature is found by considering flash-heating both in millimetric and microscopic scales. Depending on in which sub-area the micro-asperity is located, its initial temperature can be determined. By obtaining T_i, μ_i in each sub-area can also be found. T_i can be as low as ambient temperature and as high as 500 °C (after 30 mm of slip at slip rate of 0.8 m.s^{-1} and under normal stress of 8 MPa). In sub-areas with high NSR, T_i is high and V_w is low, therefore, the asperity reaches weakening quicker, and experiences lower mean friction. T_{avg} is much smaller than maximum T_i, and since areas with higher temperatures carry higher normal loads, friction on a surface with non-uniform temperature and stress would be lower than the surface with the same average temperature but with uniform stress distribution.

T_i can be found directly from the IR images; however, our objective is to develop a numeric model which enables the estimation of T_i and coefficient of friction only by knowing the sliding rate history. To develop such a forward model, first, the model needs to be calibrated using experimental measurements of friction and temperature. Based on Equation 6.8, temperature rise in each sub-area (T_i) is a function of velocity and local shear stress. Shear stress is the product of local-NS and coefficient of friction (μ_i), and friction itself is a function of T_i. Since T_i and μ_i are coupled, an iterative

algorithm should be used to find both of the variables. After calibrating the model, the values of NSR_i and weakening model parameters (e.g. μ_w, T_w, $\Delta\mu_{mm}$) are found, so that the calculated temperatures (T_i) and average macroscopic friction obtained from the model analysis match with experimental measurements. Herein, the heat transfer equations for a fast-moving heat source are used to calculate NSR_i based on the thermographs [*Jaeger*, 1942; *Archard*, 1959; *Greenwood*, 1991]. Figure 6.3 summarizes the proposed algorithm for obtaining the transient temperature and friction. Once the model parameters are calibrated, the NSR_i and model can be used to determine macroscopic friction for any experiment at the same NS with arbitrary velocity history *V(t)*. Accordingly, the model can be tested using other experiments having different *V(t)* by comparing observed $\mu(t)$ with that calculated from *V(t)* without requiring temperature and shear stress measurements as input.

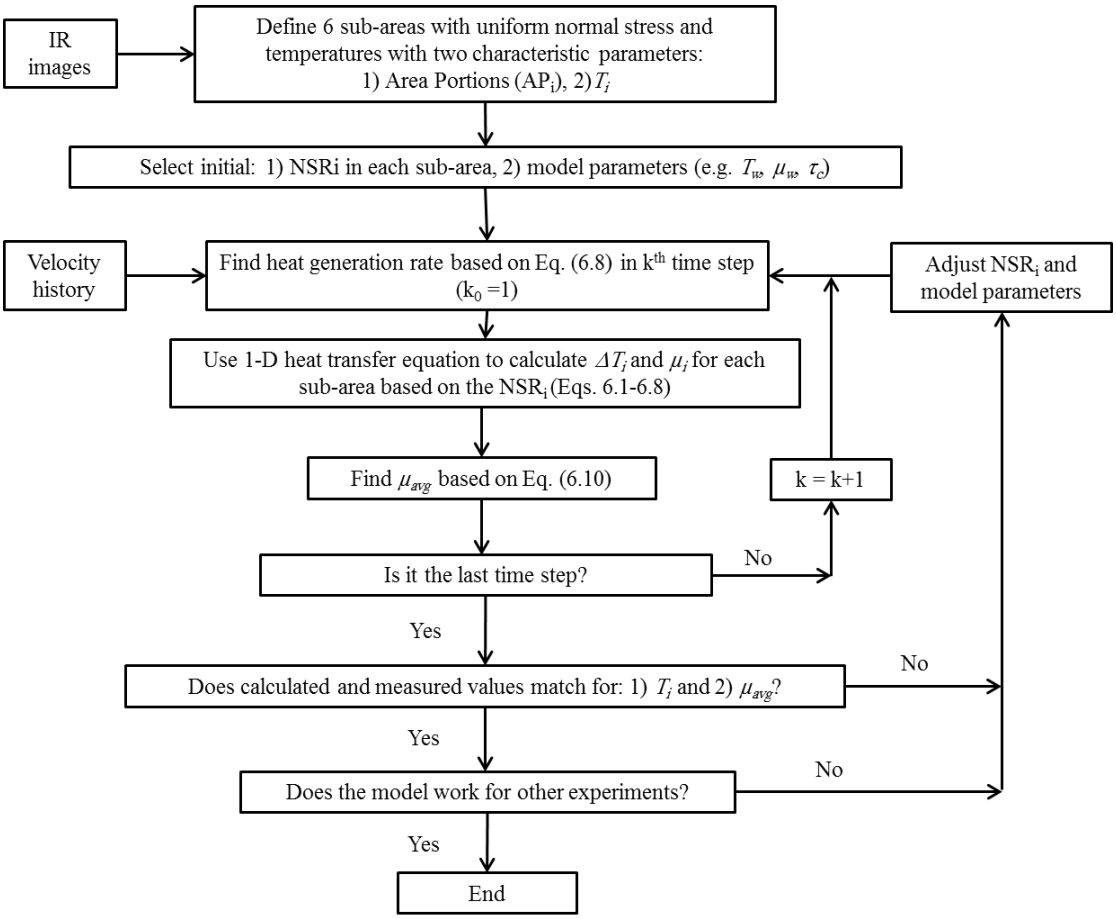

Figure 6.3: The algorithm used for calibration of the model parameters based on the IR images and macroscopic friction measurements. After the model is calibrated, for different sliding rates, the model parameters stay unchanged. In other words, after model calibration, it can be used as a forward model which takes only velocity history as input and estimates T_i, μ_i and macroscopic friction. Opposed to previous models, the forward model neither needs friction measurements to calculate T_i nor temperature measurements to calculate friction.

6.3.2 Normal stress distribution inferred from IR images

Based on the above algorithm, the forward model was calibrated for experiments conducted at a NS of 8 MPa. For the 6 subareas with representative temperatures of 37, 70, 140, 250, 350, 450 °C, and AP of 37, 24, 18, 13.5, 5, and 2.5% (as determined from

the thermographs), the ratios of local-NS to macroscopic NS (NSR) are estimated as 0.135, 0.42, 1.12, 2.4, 3.8, and 5.2, respectively. This means that maximum local-NS is 5.2 times higher than the average macroscopic NS, and a large portion of the sliding surface (37%) experiences stresses ~7.4 times smaller than the average NS. As a result of such a heterogeneous stress distribution, 21% of the surface carries about 64% of the total normal load. The NSR values were obtained using the most conservative assumption that contacts are maintained for the duration of high speed sliding. If the mm-scale contacts have shorter lifetimes, then even a smaller area would carry a greater proportion of the load.

6.3.3 Model parameters

Some of the flash-weakening model parameters were selected based on data presented in [*Passelegue et al.*, 2014] for granite (e.g. D_a, ρ, K_{th}, c_{th}). Other parameters such as μ_w, τ_c and T_w cannot be directly measured and do not have a unique value in the literature. In this study, these parameters are found by comparing the model predictions with experimental data of a set of experiments conducted at the same normal stress (~8 MPa), but under different velocity paths. Based on this approach, μ_w, τ_c and T_w were found to be 0.42 ±0.02, 1.2 GPa, and 280 °C, respectively. A weakening temperature of 280 °C is consistent with values reported in recent studies. For example, T_w = 296 °C is obtained for illite-quartz gouge [*Yao et al.*, 2016a, 2016b] and T_w = 180 °C is documented for limestone [*Tisato et al.*, 2012] well below the temperature for decarbonation of calcite in limestone (700-850 °C). A weakening temperature of 280 °C is considerably lower than the melt temperature for granite. There are several potential

reasons for low T_w in high-speed friction experiments. Only after a short distance of high-speed slip, nano particles are formed at the interface as a result of grinding and milling of the rock [*Chang et al.*, 2012; *Tisato et al*., 2012]. The activation energy for chemical reactions decreases with size of particles and consequently weakening temperature reduces significantly in the presence of nano-particles [*Tisato et al.*, 2012; *Yue et al.*, 1999]. Moreover, the internal plastic deformation caused by milling during high-speed slip may reduce the activation energy of the reaction further [*Hsu et al.*, 2002; *Steinike and Tkácová*, 2000, *Tisato et al.* 2012]. In addition to T_w, τ_c is found to be smaller than typical values predicted by micro-indentation experiments, which measure hardness of material at mico-scale; e.g., ~5.6 GPa for granite [*Passelegue et al.*, 2014; *Evans*, 1984]. However, using micro-indentation data for estimation of shear strength of micro-asperities is only valid if every in-contact micro-asperities is at the yield stress, which may not be the case for all asperities as explained in Chapter V. Alternatively, 5.6 GPa can only be used as an upper limit for τ_c.

6. 4 Effect of temperature and stress heterogeneity on micro-scale flash-weakening

As explained above, flash weakening of microscopic contacts enhances with surface temperature. In this study, the heterogeneity of stress and temperature on the sliding surface are included in the model, which is in contrast with previous studies which assumed a uniform surface temperature. To investigate the effect of stress and temperature heterogeneity, first the accuracy of the forward model is evaluated by comparing the model prediction to experimental data for a variety of velocity histories.

Next, the model predictions of the transient friction were compared for the two cases of: (1) assuming a uniform stress and temperature on the surface, (2) considering the heterogeneity of stress and temperature by using the local NS distributions inferred from the IR images. Figure 6.4 shows the model predictions for these two cases in three velocity-step experiments to sliding rates of 0.1, 0.35 and 0.8 $m.s^{-1}$. Figure 6.4 indicates that the predictions of the model which considers heterogeneity of stress, are far better compared to those of the model that assumes a uniform temperature on the surface. As a result of stress and temperature localization, the amount of weakening is generally larger than what is predicted in the case of uniform stress and temperature distribution. For example, no weakening is expected for sliding at 0.1 $m.s^{-1}$ (#HSB-WG-49) if the stress localization is ignored. Since V_w initially (when T_s = 20 °C) is higher than 0.1 $m.s^{-1}$ (based on Equation 6.2), the conventional micro-scale flash-weakening model predicts no weakening for test #HSB-WG-49 (in which sliding rate= 0.1 $m.s^{-1}$). Assuming a uniform stress distribution, the temperature rise would be about 50 °C at the end of 30 mm stroke for experiment #HSB-WG-49, which does not affect V_w significantly; however, the maximum local temperature rise is ~200 °C based on both the IR images and the revised model with heterogeneous stress distribution. A surface temperature of 200 °C decreases V_w for the sub-area to 0.008 $m.s^{-1}$, which is well below the sliding rate of 0.1 $m.s^{-1}$. This is why the revised flash-weakening model with non-uniform temperature distribution can capture experimental friction data.

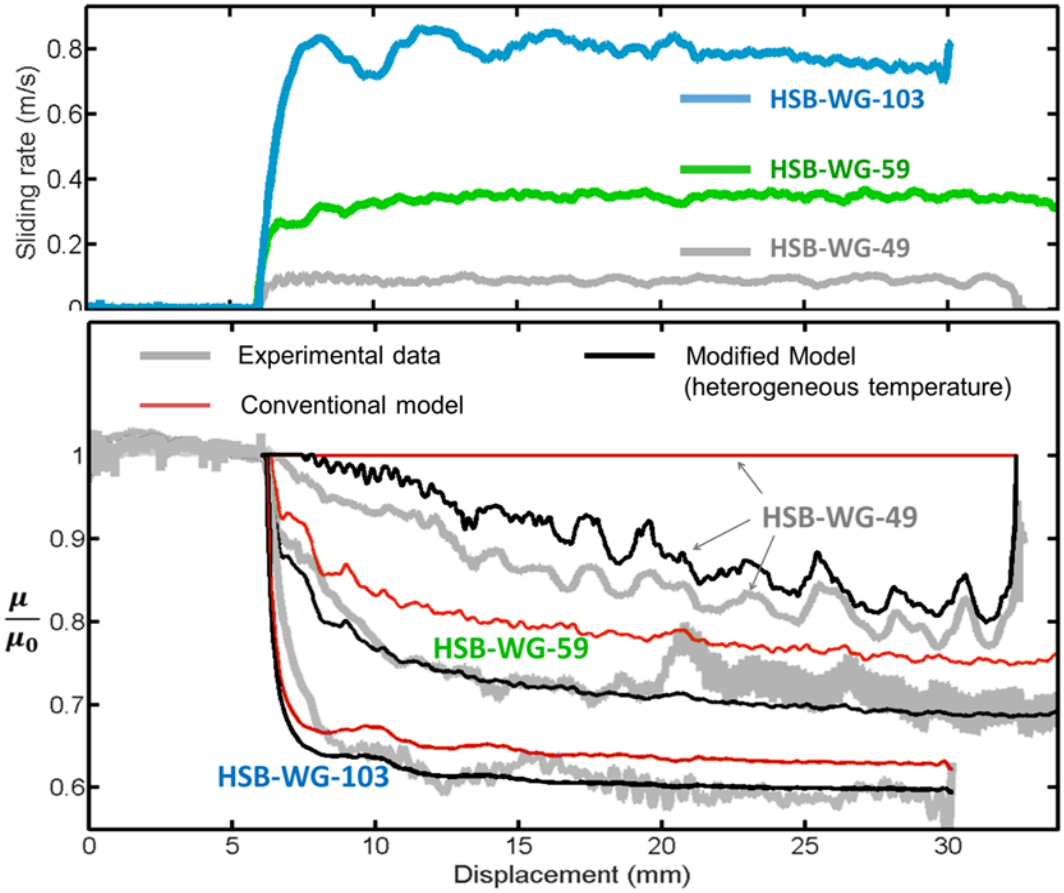

Figure 6.4: Comparison of experimental data with prediction of the micro-scale flash weakening models with uniform and non-uniform temperatures. Normalized friction curves (by the quasi-static friction, μ_{s0}) versus displacement are presented for three examples of velocity-steps from 1 mm.s^{-1} to ~100, 350, 800 mm.s^{-1} under NS of 8 ± 0.5 MPa. The flash-weakening model that accounts for stress and temperature heterogeneity provides significantly better estimations of the transient friction than the conventional flash-weakening model that assumes a uniform temperature on the sliding surface.

The results show, weakening enhances with slip and surface temperature. As a result, at the same instantaneous velocity, friction is lower at the end of slip than the beginning of slip. The evolution in surface temperature and friction results in hysteresis loops in the friction-velocity curves, as illustrated in Figure 6.5. Also, the prediction of

the micro-scale flash-weakening model considering heterogeneity of stress and temperature is shown in Figure 6.5, which fits well with data while the conventional model with uniform temperature assumption does not predict any weakening. Hysteresis loops in the friction-velocity curves can explain the healing process in natural faults and demonstrate the rate of recovery of frictional strength as velocity decelerates. Experimental data in Figure 6.5 suggest that the quasi-static friction is not recovered even when velocity is decelerated to stationary condition. This may indicate that healing process will not be completed until surface temperature decreases sufficiently. Such a behavior could not be captured accurately by the model.

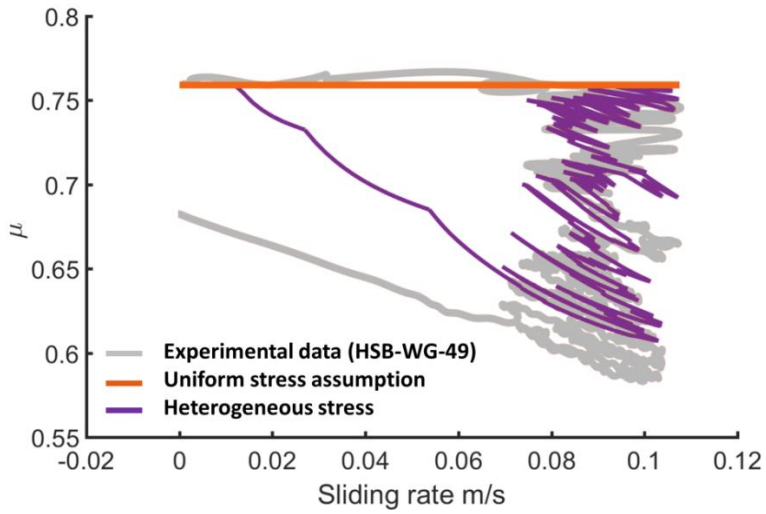

Figure 6.5: Comparing hysteresis loops in friction-velocity curves predicted by the micro-scale flash-weakening model with and without considering heterogeneity of stress and temperature on surface. The friction curve versus displacement is shown in Figure 6.4 (#HSB-WG-49). While the model with uniform surface temperature predicts no weakening, an acceptable hysteresis loop is obtained by the model that accounts for the heterogeneity of stress and temperature based on the IR images; the same model parameters are used as those in Figure 6.4.

6. 5 Multi-scale flash-weakening

Although the micro-scale flash weakening model was improved significantly relative to the conventional model by considering flash heating in multiple scales, the results could not reproduce all aspects of the transient friction accurately; specifically weakening at low sliding rates (0.1 $m.s^{-1}$) and the healing process during the deceleration phase (Figure 6.4 and 6.5). Considering that the temperature of millimetric contacts is raised significantly in a few millimeters of slip; herein, it is proposed that flash-weakening may be activated concurrently at both the mm- and micrometric- scales.

On the basis of the experimental results, transient friction upon a velocity step to high-speed sliding may be characterized by a combination of two weakening behaviors. The first one is as described by the conventional flash-weakening model for microscopic scale contacts, for which weakening is effectively instantaneous if $V > Vw$. The second weakening behavior is characterized by progressive weakening, which occurs due to a rise of T_{mm} (Figure 6.6). These two weakening behaviors satisfy the hypothesis that weakening occurs concurrently at both the micro- and mm-scales. At high sliding-rates, the heating of mm-scale and larger contacts is similar to flash-heating of μm-scale contacts in that the depth-extent of the temperature rise is much less than the dimension of the contact; i.e., temperature rise of a millimetric contact is superficial, and can be hundreds of degrees higher than the temperature of the substrate. Therefore, low shear strength at the surface and high hardness of the substrate can lead to weakening of the mm-size contact areas. Temperature and time are the main factors that control activation

of chemo-mechanical processes; thus, the longer lifetime of larger, heated contacts may activate weakening processes different than those active at the μm-scale over shorter lifetimes. Accordingly, it is hypothesized that the total flash-weakening of the surfaces may be given by the sum of weakening by independent μm- and mm-scale processes:

$$\Delta\mu = \Delta\mu_{\mu m} + \Delta\mu_{mm} \tag{6.11}$$

To test and evaluate the multi-scale flash-weakening hypothesis, a simple model has been developed that can include distinct weakening mechanisms at the μm- and mm-scale. For the μm-scale mechanism, the conventional flash-weakening relations given in Equation 6.1 and 6.2 are employed, but for the mm-scale mechanism, a gradual weakening as a function of temperature is assumed. Using a gradual weakening model as a function of temperature is consistent with work by *Noda* [2008] and *Passelègue et al.* [2014]. Here, an exponential decrease in strength of mm-scale contacts with temperature is employed, as follows:

$$\Delta\mu_{mm} = \Delta\mu_{mm_{max}} \cdot \left(1 - e^{-\frac{T_{mm} - T_a}{\alpha T_r}}\right),\ \alpha = -\frac{T_r - T_a}{\ln(0.1) \times T_r} \tag{6.12}$$

where, T_{mm} is the temperature of the mm-scale contacts, T_a is the ambient temperature, and T_r = 900 °C is the reference temperature at which 90% of $\Delta\boldsymbol{\mu_{mm}}$ occurs. Numerical time-stepping models of the experiments were run using the velocity history as input. Also, it is assumed that the LNS distribution determined from the thermograph analysis is independent of velocity and slip distance, as done for the microscale flash weakening.

a)

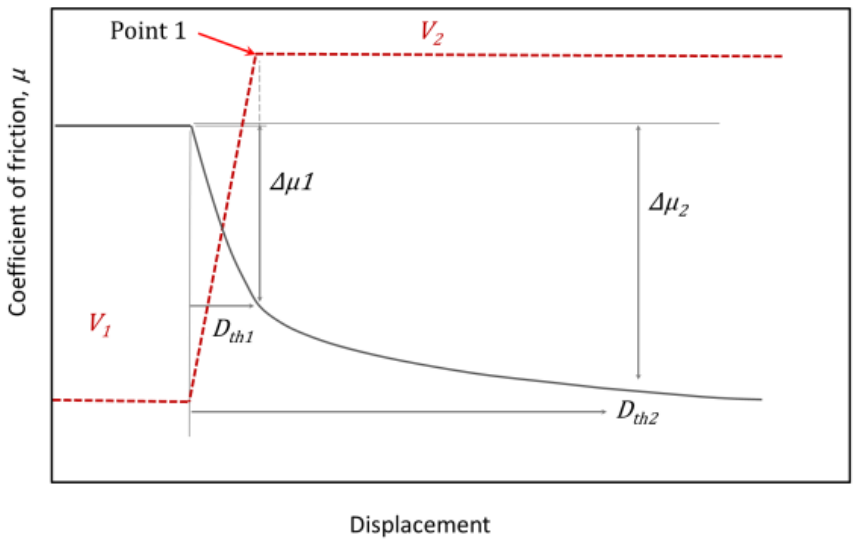

b)

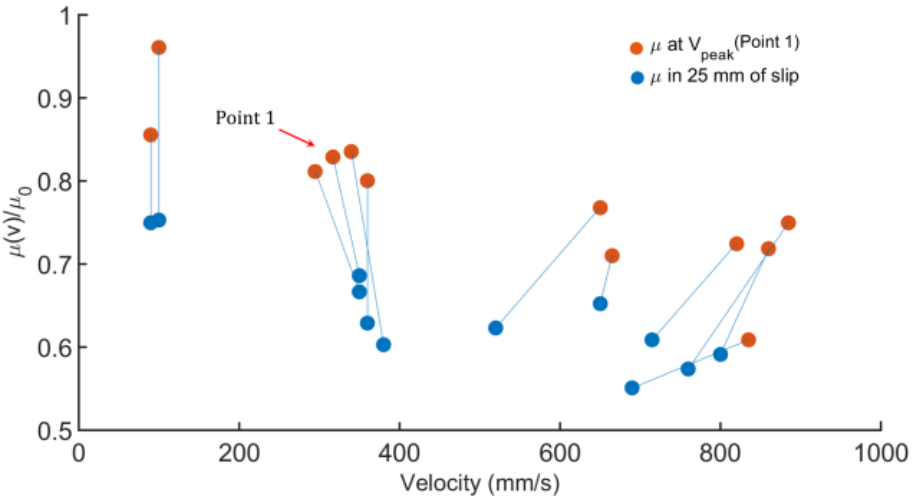

Figure 6.6: Instantaneous and gradual weakening observed in velocity-step experiments. a) Two weakening behaviors are observed. The first displays rapid weakening concurrent with increasing velocity to the peak velocity, V_{peak} (point 1), and the apparent slip distance for weakening, D_{th1} is approximately equivalent to d_r. The second is gradual weakening with slip at relatively constant velocity, with a larger apparent slip distance D_{th2}. b) Plot of friction normalized by the quasi-static friction (μ_{s0}) as a function of the velocity at V_{peak} (red symbols) and at 25 mm of high-speed slip (blue symbols) show the relative effects of the first (red) and second (blue) weakening behaviors for several experiments at normal stresses of 8-16 MPa. The lines connect measurements from the same experiment.

The strategy for testing and evaluating the hypothesis of the multi-scale flash-weakening is to use a single set of parameter values to model a subset of our experiments comprised of four velocity-step experiments, all conducted at the same NS but different velocity paths. Specifically, three of the experiments consist of velocity steps to a constant velocity of 0.1, 0.35 and 0.8 $m.s^{-1}$ for 25-30 mm of high-speed slip (Figure 6.7 and 6.8), and one experiment is a step to 0.6 $m.s^{-1}$ followed by a gradual decrease in velocity to zero over 30 mm of slip (Figure 6.9). The models were then fitted to the friction versus displacement and friction versus velocity experimental results. The efficacy of each model is determined using experimental data. The two models are: the conventional model (Equation 6.1 and 6.2) that only includes a μm-scale flash-weakening (Figure 6.4-6.5), and the (revised) multi-scale model (Equation 6.1-6.2 and Equation 6.11-6.12) that includes independent μm- and mm-scale flash-weakening (Figure 6.7-6.8). Although a reasonable fit can be achieved for any individual experiment with either friction model by adjusting the friction parameters, fitting all the four experiments with a single set of parameters is far better achieved with the multi-scale model (compare Figures 6.7, 6.8 to Figures 6.4, 6.5). In particular, the multi-scale flash weakening model has a greater ability to describe friction behavior at lower velocities, as well as the strength recovery during deceleration, and the transient progressive weakening after velocity-steps to constant velocity (Figures 6.7-6.9). Although the micro-scale flash-weakening model is not entirely capable of describing the experiment results, the model is more successful if the mm-scale when heterogeneity

of surface temperature is considered, than if a uniform surface temperature is assumed as done in all previous work.

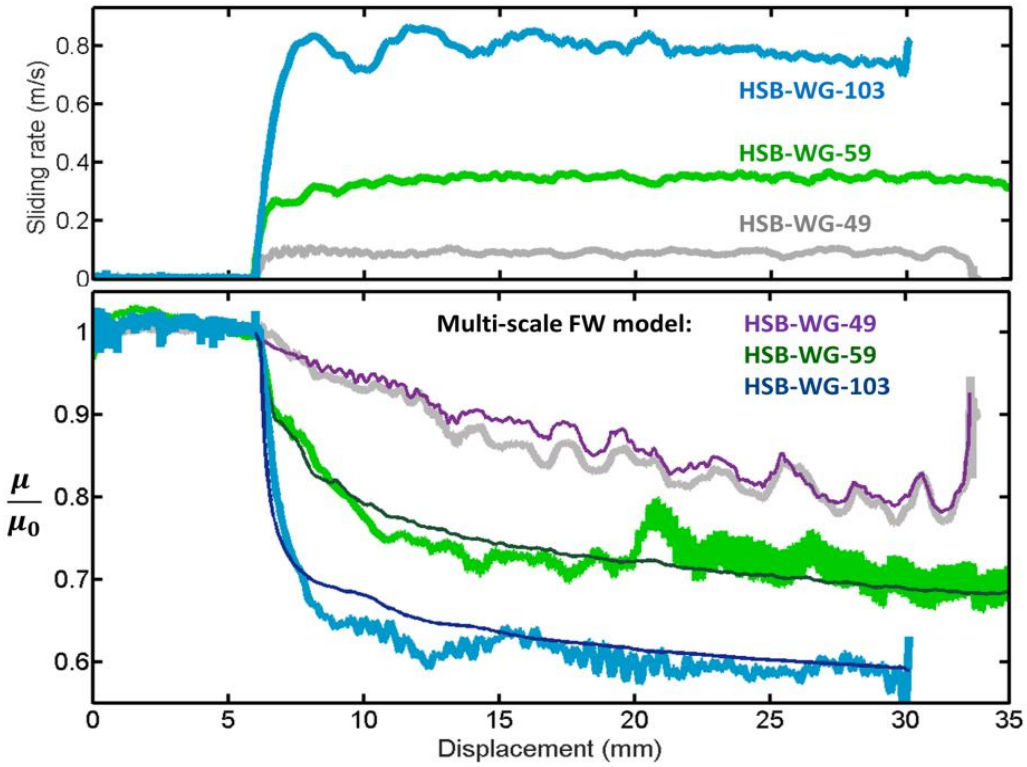

Figure 6.7: Comparison of the multi-scale flash-weakening model to experimental data in three representative velocity-step tests. Velocity-steps from 1 mm.s^{-1} to ~0.1, 0.35, 0.8 m.s^{-1} at a normal stress of 8 ±0.5 MPa are shown in the top frame. The observed flash-weakening behavior for the three experiments is shown by the thick colored lines in a plot of friction normalized by the quasi-static friction (μ_{s0}) versus displacement (μ_{s0} is within a range of 0.73±0.05). The fit of the multi-scale flash-weakening model to experimental data is shown by thin lines in the lower frame. The multi-scale model accounts for the heterogeneity of stress and temperature and is able to predict the transient friction accurately for the whole range of sliding rates using a single common set of material properties and constitutive parameters: τ_c = 1.58 GPa × μ_{so} (shear strength is considered to be proportional to quasi-static friction consistent with the flash-weakening model), μ_{s0}: measured, μ_w= 0.52 ±0.02, D_a= 4 µm, T_w= 280 °C, $\Delta\mu_{mm\text{-}max}$= 0.24, ρ= 2350 kg.m^{-3}, K_{th}=2.64 J.(s.m.K)$^{-1}$, c_{th}= 900 J.kg^{-1}.K^{-1}.

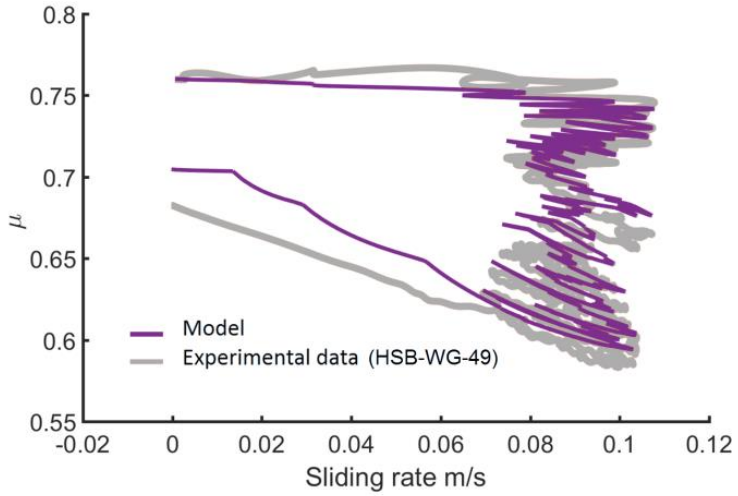

Figure 6.8: Comparison of the multi-scale flash-weakening model with experimental data. Friction versus velocity is depicted for experiment #HSB-WG-49. The multi-scale model accounts for the heterogeneity of stress and temperature and is able to predict the transient friction accurately during acceleration and deceleration (compared to Figure 6.5) using the same, single common set of material properties and constitutive parameters used in Figure 6.7.

The two transient weakening behaviors described in Figure 6.6a can be clearly seen in Figure 6.7. At 0.8 $m.s^{-1}$, the dominant weakening process is instantaneous and related to micro-scale flash-weakening, whereas at 0.1 $m.s^{-1}$, gradual weakening at mm-scale is initially dominant. However, from the increase in dependence of friction on instantaneous velocity-changes (observed in the friction curve for experiment #HSB-WG-49), it can be inferred that with gradual rise of T_{mm} with slip, micro-scale weakening is triggered with a delay. This is consistent with gradual weakening reported for meter-sized rock samples at relatively low sliding rates [*Yamashita et al.*, 2015].

In addition to frictional sliding experiments with step-like velocity paths, a set of experiments were done in which velocity is accelerated rapidly followed by gradual

deceleration to a stationary condition. These experiments are similar to Earthquake-Like Slip Events (ELSE experiments) done by *Chang et al.* [2012]. Due to the low deceleration rate, the recovery process of frictional strength and the hysteresis loop formed in friction-velocity curve can be best documented with the ELSE experiments. Figure 6.9a shows an ELSE velocity path and the corresponding frictional behavior of the sample during weakening and healing phases. Also, the prediction of the multi-scale flash-weakening model is presented in the figure. The results are shown both as a function of displacement (Figure 6.9a) and velocity (Figure 6.9b). Figure 6.9b illustrates the hysteresis loop caused by slip- and temperature- dependence of friction. The figure demonstrates that the multi-scale flash-weakening model provides a powerful tool to predict and explain the transient friction both in weakening and healing phases.

In natural faults, stress may be localized in meter-sized areas and parallel weakening mechanisms can extend from μm to meter length-scales. Characterization of natural faults has revealed that roughness decreases with scale. Lower roughness of larger length-scales can increase the duration of contact and result in high temperature rises in those scales. Due to localization of stress, large volume regions with temperatures close to weakening temperature (and dramatically higher than the mean surface temperature) can be formed that carry a major portion of the normal load and dictate frictional behavior of the sliding surface. Localization of stress and temperature in larger length-scales and consequent activation of weakening in scales greater than microscopic asperities can extend the cooling process and delay strength recovery of weakened sliding surface.

a)

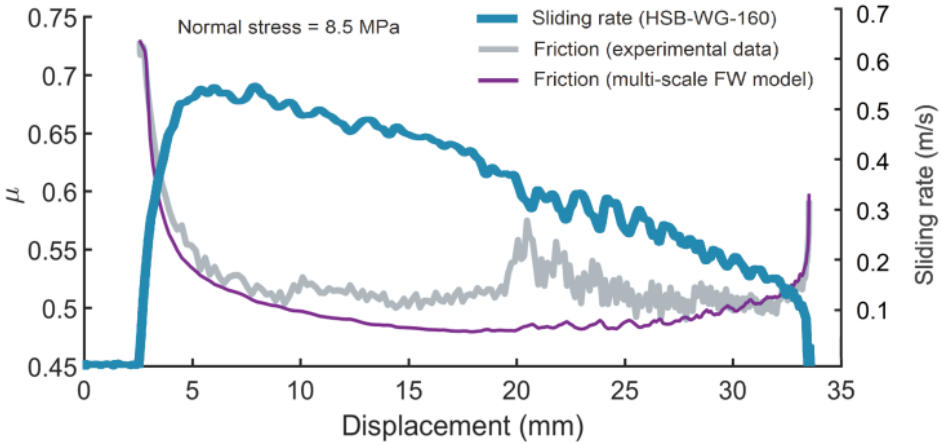

b)

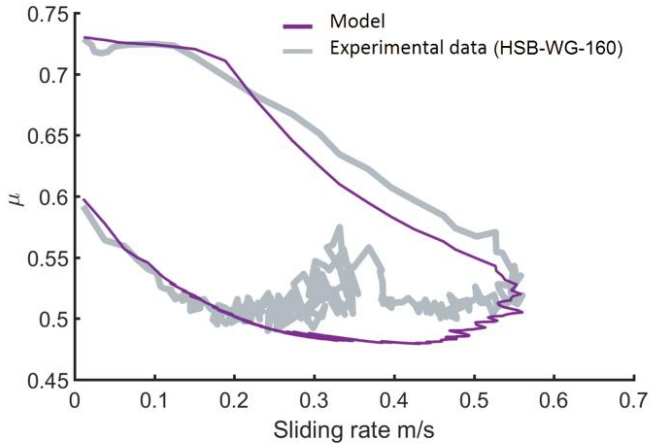

Figure 6.9: Comparison of the multi-scale flash-weakening model to flash weakening and strength recovery in two experiments with different velocity load-paths. Model parameters are the same as those used for the three velocity-step experiments shown in Figure 6.6. a) Comparison of the model prediction to the results of an experiment in which velocity is accelerated rapidly followed by gradual deceleration to a stationary condition (ELSE experiment). b) Friction-velocity curves illustrate the hysteresis in friction due to the progressive change of temperature on the sliding surface during acceleration and deceleration. Friction is low at the beginning of the deceleration phase and frictional strength recovery only occurs after V drops below 200 mm.s^{-1}.

CHAPTER VII

CONCLUSIONS

Sliding rock-samples at seismic slip-rates (0.01 – 1 ms^{-1}) demonstrate a significant reduction of friction, often referred to as dynamic weakening. Dynamic weakening can help explain earthquake rupture characteristics and the apparent low strength of crustal faults. However, at seismic sliding rates, the frictional behavior of rock materials is not well-understood and appropriate constitutive relations are not completely developed. For studying velocity dependence of friction, as well as testing models of dynamic weakening at high slip-rates, imposing a step-like velocity change during sliding is desired. Accordingly, a novel High-Speed Biaxial (HSB) testing-machine for friction was introduced, in which, achieving velocity-steps under high resistive force of samples was the main design objective. In Chapter III, the governing equations of the hydro-pneumatic loading system of the HSB were derived and its dynamics was studied in order to investigate the feasibility of achieving the desired velocity-step for the range of expected rock-sample behaviors. Rock samples can initially exhibit a large resistive frictional force, but due to dynamic weakening at high sliding rates, the resistive force may diminish dramatically. Accordingly, by considering the interaction of testing-specimen and the hydro-pneumatic loading system, an analytical model of the system was derived and analyzed. Numerical simulations were

performed to investigate the effect of different variables on the velocity pattern of the HSB, and a method of obtaining the pre-set passive control variables (PPCV) for achieving velocity-steps was presented. Finally, in Chapter III, the key design parameters of the HSB were obtained so that its workspace covers the required testing conditions, and in absence of feedback control, the step-like velocity changes could be achieved.

In Chapter IV, it was shown how the prototype of the HSB was instrumented and tested to evaluate its capability of imposing velocity-steps. Also, the analytical model developed in Chapter III was validated and calibrated using the instrumented HSB. To characterize the behavior of the prototype, the prototype HSB was equipped with sensors, and DAQ software was developed using LabVIEW (using FPGA programing) to collect and store experimental data (at 50 kHz). Experimental data confirmed that the apparatus can produce high accelerations (up to 50 g) to achieve velocity-steps over small displacement (~ 1 mm) to target velocities of $0.01 - 1\ ms^{-1}$, and that after the step, the velocity can be maintained constant for the remainder of the stroke (~4 cm). Frictional sliding experiments were done in a wide range of testing conditions on unconfined rock test-samples, and the machine could generate the step-like velocity paths successfully. In addition to sliding friction experiments, a series of experiments were designed and conducted to simulate extreme cases of dynamic weakening, which might occur in confined conditions. These tests indicated that under extreme cases of test-specimen weakening, an impact-type loading is imposed to the hydro-pneumatic loading system, which can induce undesired vibrations. To investigate the vibrations, an

analytical model was developed by considering the stiffness of the continuous loading system and the compressibility of fluid in the hydraulic damping system. The presented model could accurately represent the vibrations observed in the experiments. Moreover, the analytical model of the prototype HSB was used to identify and treat the major sources of vibrations. Accordingly, a modified design of the hydro-pneumatic system was proposed which can reduce the undesirable vibrations significantly.

After development of the HSB prototype, it was used to study frictional behavior of rock material, specifically Westerly granite, under different velocity paths and normal stresses. This study showed that friction experiments can be conducted successfully in triaxial and double-direct configurations at high velocities. The triaxial and biaxial test-configurations have been disregarded for high-speed friction experiments mostly because the displacements are limited compared to rotary shear configuration. Nevertheless, the results indicated that at high accelerations, dynamic weakening can occur in a very short displacement (as low as ~1 mm). Therefore, the entire weakening process can be observed within the stroke of the machine. By performing friction experiments under high accelerations (at least one order of magnitude higher than those in rotary configuration) major improvements can be achieved in understanding of velocity dependence of friction. Moreover, by having a pressure vessel in these two configurations, higher normal stress and fluid confinement also is possible in future work. Particularly, in using the triaxial configuration, the rock-sample is sealed simply and friction experiments at high temperature and independent pore and confining pressures can be conducted (which is not possible in the existing rotary friction-testing

machines). By employing the ultimate HSB machine with a pressure vessel, which is under development, parametric studies of the dependence of rock friction on normal stress, sliding rate, acceleration, temperature, pore water and confining pressure spanning the real conditions during natural earthquakes can be conducted.

The results of sliding-friction experiments, presented in Chapter V, showed that at seismic slip rates, the coefficient of friction of the rock sample decreases dramatically. The magnitude of weakening was found to be controlled primarily by sliding-rate and normal stress. Accordingly, experiments were designed and conducted in a wide range of velocities and normal stresses to investigate the effect of these two parameters on weakening. The experimental data indicate that weakening is enhanced with velocity and normal stress, and reductions as high as 40% of the quasi-static frictional strength were observed at a sliding rate of 0.8 $m.s^{-1}$ and under moderate normal stresses (10 – 20 MPa). Conducting experiments under high accelerations demonstrated that weakening can occur very rapidly upon a rise in velocity, and weakening distances as low as 1 mm were reported. Such a short weakening distance suggested that flash heating at true areas of contact triggers dynamic weakening. Due to flash-heating, local temperature of the contacts rises rapidly for a short time and weakening can occur in sub-millimetric distances (in contrast with bulk melting, which requires a relatively large slip distance).

In order to investigate flash heating in rock, the HSB was instrumented with a high-speed IR camera, and the 2-D distribution of temperature on the contact area was documented. Temperatures up to ~500˚C were observed in less than 25 mm of slip under normal stresses of ~8 MPa at 0.8 $m.s^{-1}$. The IR images indicate that under dynamic slip

conditions, stress localizes remarkably on the sliding surface leading to a highly heterogeneous distribution of stress and temperature on the surface. These results contrast with previous works on flash-weakening that typically assume the surface temperature is uniform at the mm-scale and raised only ~100 °C at similar conditions (based on an average stress distribution). The high flash temperatures observed on the sliding surface can trigger thermal chemo-mechanical weakening mechanisms and may explain the low magnitude of friction reported at seismic sliding rates in natural faults.

Characteristics of contact areas on a sliding surface have a fundamental influence on frictional behavior of rock material. In this study, it was shown that contacts can form over a range of length-scales. The flash temperature observations on the sliding surface were used to characterize the contacts. The results show that clusters of microscopic asperities can form millimetric contact areas. In the sliding experiments, the mm-sized contacts experienced stresses up to ~5 times the average stress. The maximum temperature of mm-sized areas increased with macroscopic normal stress for low to moderate stresses, but further increase in normal stress did not increase the maximum temperature considerably. This suggests that, millimetric contact areas reach a maximum stress limit analogous to strength of material at the millimetric scale for unconfined conditions. Also, by analyzing the size and number of millimetric contact areas formed under a range of normal stress, millimetric contacts were found to be similar to microscopic asperities in that the number of contacts increases with normal stress. Stress level at microscopic asperities has a significant effect on weakening. However, after reaching the yield strength in millimetric contact areas, microscopic contacts nested in

the saturated millimetric areas would not realize a further increase in macroscopic normal stress; instead, new millimetric contacts are formed that carry the extra normal load. Thus, for multi-scale contacts, characteristics of larger length-scale contacts can play a key role in stress realization of smaller contacts embedded in them.

Rapid weakening and flash temperatures observed in the sliding friction experiments suggest that weakening mechanism is triggered by flash-heating. However, in contrast with the flash weakening model (which neglects the dependence of friction on normal stress), the results show that weakening reduces significantly if normal stress is < 8 MPa. Contact analysis for microscopic asperities show that, on average, the effective dimension of micro-scale contacts does not change noticeably with normal stress. Therefore, expansion of microscopic contacts, which was previously proposed in the literature as a major cause of enhancement of weakening with normal stress, cannot be a significant factor. Instead, an increase in normal stress can raise temperature and stress in localized contact areas and cause a higher degree of weakening. The results also suggest that flash weakening model assumption about pure plastic deformation of microscopic contacts may not be accurate at low normal stresses. In natural faults, normal stress is generated by overburden weight of layers of rock on top of the slipping fault, thus, normal stress varies as a function of the depth. Since normal stress can influence weakening from early stages of the transient friction, nucleation and rupture propagation can be influenced significantly by the depth of the earthquake, and diverse modes of fault slip can occur across the crust.

The thermographic images presented in this dissertation, provide the first documentation of the geometry and spatial distributions of mm-scale contact areas formed in rock during frictional sliding at seismic rates. The new findings provide key observations for understanding flash-weakening in faults and testing constitutive models. In Chapter VI, it was shown that the flash-heating of mm-scale contacts can impact transient frictional weakening in two ways: (1) by raising the surface temperature, and thus decreasing V_w, for the clusters of μm-scale contacts within the mm-scale contacts, and (2) by activating an additional parallel weakening mechanism that operates at the mm-scale concurrently with μm-scale flash-weakening. The finding that contacts form at multiple length scales during frictional sliding is congruous with the fact that fault surfaces are rough over a wide range in length scales, and with previous inferences that the strength of contacts decrease with increasing contact size. Modeling our experimental results corroborated the hypothesis of parallel-concurrent mechanisms of flash-weakening operating at different scales. The significance of multi-scale flash-heating to the physics of earthquake rupture include the general expectation that (1) weakening by flash-heating is inherently transient and slip-history dependent, (2) the re-strengthening of flash-weakened surfaces during deceleration will be increasingly retarded with an increase in prior seismic-slip magnitude (which can affect the magnitude of the earthquake), and (3) conventional steady-state flash-weakening relations based on only μm-scale contacts are unable to fully capture the transient friction weakening and healing during seismic slip of natural faults.

REFERENCES

Archard, J. (1959), The temperature of rubbing surfaces, *Wear*, *2*(6), 438-455.

Bar-Sinai, Y., R. Spatschek, E. A. Brener, and E. Bouchbinder (2015), Velocity-strengthening friction significantly affects interfacial dynamics, strength and dissipation, *Scientific Reports*, *5*.

Bardenheier, R., and G. Rogers (2003), Dynamic impact testing, *Instron Ltd., High Wycombe, UK*.

Beeler, N. M., T. E. Tullis, and D. L. Goldsby (2008), Constitutive relationships and physical basis of fault strength due to flash heating, *Journal of Geophysical Research: Solid Earth*, *113*(1).

Boitnott, G. N., R. L. Biegel, C. H. Scholz, N. Yoshioka, and W. Wang (1992), Micromechanics of rock friction: 2. Quantitative modeling of initial friction with contact theory, *Journal of Geophysical Research*, *97*(B6), 8965-8978.

Boneh, Y., A. Sagy, and Z. Reches (2013), Frictional strength and wear-rate of carbonate faults during high-velocity, steady-state sliding, *Earth and Planetary Science Letters*, *381*, 127-137.

Brantut, N., and J. D. Platt (2016), The depth-dependence of dynamic weakening, unpublished material.

Brantut, N., F. X. Passelègue, D. Deldicque, J.-N. Rouzaud, and A. Schubnel (2016), Dynamic weakening and amorphization in serpentinite during laboratory earthquakes, *Geology*, *44*(8), 607-610.

Briers III, W. J. (2015), Overcoming challenges in material characterization of polymers at intermediate strain rates, in *Challenges in Mechanics of Time-Dependent Materials, Volume 2*, edited, pp. 153-164, Springer.

Brodsky, E. E., J. D. Kirkpatrick, and T. Candela (2016), Constraints from fault roughness on the scale-dependent strength of rocks, *Geology*, *44*(1), 19-22.

Candela, T., and E. E. Brodsky (2016), The minimum scale of grooving on faults, *Geology*, *44*(8), 603-606.

Carpenter, B. M., C. Marone, and D. M. Saffer (2009), Frictional behavior of materials in the 3D SAFOD volume, *Geophysical Research Letters*, *36*(5).

Carslaw, H. S., and J. C. Jaeger (1959), Conduction of heat in solids, *Oxford: Clarendon Press, 1959, 2nd ed.*

Chang, J. C., D. A. Lockner, and Z. Reches (2012), Rapid acceleration leads to rapid weakening in earthquake-like laboratory experiments, *Science*, *338*(6103), 101-105.

Chester, F. M., and J. M. Logan (1986), Implications for mechanical properties of brittle faults from observations of the Punchbowl fault zone, California, *Pure and Applied Geophysics PAGEOPH*, *124*(1-2), 79-106.

Chester, F. M., and N. G. Higgs (1992), Multimechanism friction constitutive model for ultrafine quartz gouge at hypocentral conditions, *Journal of Geophysical Research*, *97*(B2), 1859-1870.

Chester, F. M. (1994), Effects of temperature on friction: constitutive equations and experiments with quartz gouge, *Journal of Geophysical Research*, *99*(B4), 7247-7261.

Chester, F. M., and J. S. Chester (1998), Ultracataclasite structure and friction processes of the Punchbowl fault, San Andreas system, California, *Tectonophysics*, *295*(1-2), 199-221.

Cunningham, R. (1951), Orifice meters with supercritical compressible flow, *Trans. ASME*, *73*, 625-638.

De Paola, N., T. Hirose, T. Mitchell, G. Di Toro, C. Viti, and T. Shimamoto (2011), Fault lubrication and earthquake propagation in thermally unstable rocks, *Geology*, *39*(1), 35-38.

Di Toro, G., D. L. Goldsby, and T. E. Tullis (2004), Friction falls towards zero in quartz rock as slip velocity approaches seismic rates, *Nature*, *427*(6973), 436-439.

Di Toro, G., R. Han, T. Hirose, N. De Paola, S. Nielsen, K. Mizoguchi, F. Ferri, M. Cocco, and T. Shimamoto (2011), Fault lubrication during earthquakes, *Nature*, *471*(7339), 494-499.

Dieterich, J. H. (1978), Time-dependent friction and the mechanics of stick-slip, *Pure and Applied Geophysics PAGEOPH*, *116*(4-5), 790-806.

Dieterich, J. H., and B. D. Kilgore (1994), Direct observation of frictional contacts: New insights for state-dependent properties, *Pure and Applied Geophysics*, *143*(1-3), 283-302.

Dieterich, J. H., and B. D. Kilgore (1996), Imaging surface contacts: Power law contact distributions and contact stresses in quartz, calcite, glass and acrylic plastic, *Tectonophysics*, *256*(1-4 SPEC. ISS.), 219-239.

Elbanna, A. E., and J. M. Carlson (2014), A two-scale model for sheared fault gouge: Competition between macroscopic disorder and local viscoplasticity, *Journal of Geophysical Research: Solid Earth*, *119*(6), 4841-4859.

Evans, B. (1984), The effect of temperature and impurity content on indentation hardness of quartz, *Journal of Geophysical Research: Solid Earth*, *89*(B6), 4213-4222.

Goldsby, D. L., and T. E. Tullis (2011), Flash heating leads to low frictional strength of crustal rocks at earthquake slip rates, *Science*, *334*(6053), 216-218.

Green II, H., F. Shi, K. Bozhilov, G. Xia, and Z. Reches (2015), Phase transformation and nanometric flow cause extreme weakening during fault slip, *Nature Geoscience*, *8*(6), 484-489.

Green, S., J. Leasia, R. Perkins, and C. Maiden (1968), Development of Multiaxial Stress High Strain-Rate Techniques, *Final Report Material Response Studies, SAMSO TR-68-71*, *3*.

Greenwood, J. (1991), An interpolation formula for flash temperatures, *Wear*, *150*(1-2), 153-158.

Greenwood, J., and J. Williamson (1966), Contact of nominally flat surfaces, paper presented at Proceedings of the Royal Society of London A: Mathematical, Physical and Engineering Sciences, The Royal Society.

Han, R., T. Shimamoto, T. Hirose, J.-H. Ree, and J.-i. Ando (2007), Ultralow friction of carbonate faults caused by thermal decomposition, *Science*, *316*(5826), 878-881.

Hirose, T., and T. Shimamoto (2005), Growth of molten zone as a mechanism of slip weakening of simulated faults in gabbro during frictional melting, *Journal of Geophysical Research B: Solid Earth*, *110*(5), 1-18.

Hirose, T., K. Mizoguchi, and T. Shimamoto (2012), Wear processes in rocks at slow to high slip rates, *Journal of Structural Geology*, *38*, 102-116.

Hsu, S. M., J. Zhang, and Z. Yin (2002), The nature and origin of tribochemistry, *Tribology Letters*, *13*(2), 131-139.

Hulikal, S., K. Bhattacharya, and N. Lapusta (2015), Collective behavior of viscoelastic asperities as a model for static and kinetic friction, *Journal of the Mechanics and Physics of Solids*, *76*, 144-161.

Jaeger, J. (1942), Moving heat sources and friction temperature, paper presented at Proc. Roy. Soc. NSW.

Kitajima, H., F. M. Chester, and J. S. Chester (2011), Dynamic weakening of gouge layers in high-speed shear experiments: Assessment of temperature-dependent friction, thermal pressurization, and flash heating, *Journal of Geophysical Research: Solid Earth*, *116*(B8).

Lindholm, U., and L. Yeakley (1967), A dynamic biaxial testing machine, *Experimental Mechanics*, *7*(1), 1-7.

Linker, M. F., and J. H. Dieterich (1992), Effects of variable normal stress on rock friction: observations and constitutive equations, *Journal of Geophysical Research*, *97*(B4), 4932-4940.

Logan, J. M., and J. Handin (1970), Triaxial compression testing at intermediate strain rates, paper presented at The 12th US Symposium on Rock Mechanics (USRMS), American Rock Mechanics Association.

Ma, S., T. Shimamoto, L. Yao, T. Togo, and H. Kitajima (2014), A rotary-shear low to high-velocity friction apparatus in Beijing to study rock friction at plate to seismic slip rates, *Earthquake Science*, *27*(5), 469-497.

Mair, K., F. Renard, and O. Gundersen (2006), Thermal imaging on simulated faults during frictional sliding, *Geophysical Research Letters*, *33*(19).

Marone, C. (1998), Laboratory-derived friction laws and their application to seismic faulting, in *Annual Review of Earth and Planetary Sciences*, edited, pp. 643-696.

Nielsen, S., G. Di Toro, T. Hirose, and T. Shimamoto (2008), Frictional melt and seismic slip, *Journal of Geophysical Research: Solid Earth*, *113*(B1).

Niemeijer, A., G. Di Toro, S. Nielsen, and F. Di Felice (2011), Frictional melting of gabbro under extreme experimental conditions of normal stress, acceleration, and sliding velocity, *Journal of Geophysical Research: Solid Earth*, *116*(B7).

Niemeijer, A., G. Di Toro, W. A. Griffith, A. Bistacchi, S. A. F. Smith, and S. Nielsen (2012), Inferring earthquake physics and chemistry using an integrated field and laboratory approach, *Journal of Structural Geology*, *39*, 2-36.

Noda, H. (2008), Frictional constitutive law at intermediate slip rates accounting for flash heating and thermally activated slip process, *Journal of Geophysical Research B: Solid Earth*, *113*(9).

Ohnaka, M. (2003), A constitutive scaling law and a unified comprehension for frictional slip failure, shear fracture of intact rock, and earthquake rupture, *Journal of Geophysical Research B: Solid Earth*, *108*(2), ESE 6-1 - 6-21.

Ozisik, M., H. Orlande, L. Hector Jr, and P. Anyalebechi (1992), Inverse problem of estimating interface conductance during solidification via conjugate gradient method, *Journal of Materials Processing & Manufacturing Science(USA)*, *1*(2), 213-225.

Passelègue, F. X., D. L. Goldsby, and O. Fabbri (2014), The influence of ambient fault temperature on flash-heating phenomena, *Geophysical Research Letters*, *41*(3), 828-835.

Paterson, M., and T. Wong (2005), Experimental Rock Deformation: The Brittle Field, Springer-Verlag, *New York*.

Power, W. L., and T. E. Tullis (1991), Euclidean and fractal models for the description of rock surface roughness, *Journal of Geophysical Research: Solid Earth*, *96*(B1), 415-424.

Proctor, B. P., T. M. Mitchell, G. Hirth, D. Goldsby, F. Zorzi, J. D. Platt, and G. Di Toro (2014), Dynamic weakening of serpentinite gouges and bare surfaces at seismic slip rates, *Journal of Geophysical Research B: Solid Earth*, *119*(11), 8107-8131.

Rathakrishnan, E. (2010), *Applied Gas Dynamics*, John Wiley & Sons.

Renard, F., K. Mair, and O. Gundersen (2012), Surface roughness evolution on experimentally simulated faults, *Journal of Structural Geology*, *45*, 101-112.

Rice, J. R. (2006), Heating and weakening of faults during earthquake slip, *Journal of Geophysical Research B: Solid Earth*, *111*(5).

Ruina, A. (1983), Slip instability and state variable friction laws, *Journal of Geophysical Research*, *88*(B12), 10359-10370.

Saber, O., F. M. Chester, and J. L. Alvarado (2014), Dynamic analysis of a high load, high-speed actuator for rock deformation experimentation, paper presented at Proceedings of the ASME Design Engineering Technical Conference.

Saber, O., F. M. Chester, and J. L. Alvarado (2016), Development of a Material-Testing Machine for Study of Friction: Experimental Analysis of Machine Dynamics and Friction of Rock, *Experimental Mechanics*, *56*(5), 813-831.

Sagy, A., and E. E. Brodsky (2009), Geometric and theological asperities in an exposed fault zone, *Journal of Geophysical Research: Solid Earth*, *114*(2).

Sagy, A., E. E. Brodsky, and G. J. Axen (2007), Evolution of fault-surface roughness with slip, *Geology*, *35*(3), 283-286.

Schlotter, M., and A. Plummer (2011), Learning control strategies for high-rate materials testing machines, *Proceedings of the Institution of Mechanical Engineers, Part I: Journal of Systems and Control Engineering*, 0959651811404871.

Scholz, C. H. (1998), Earthquakes and friction laws, *Nature*, *391*(6662), 37-42.

Senseny, P., H. Lindberg, and T. Kennedy (1979), A machine for static and dynamic triaxial testing, *Experimental Mechanics*, *19*(2), 63-68.

Skeel, R. D., and M. Berzins (1990), A method for the spatial discretization of parabolic equations in one space variable, *SIAM journal on Scientific and Statistical Computing*, *11*(1), 1-32.

Steinike, U., and K. Tkáčová (2000), Mechanochemistry of solids—real structure and reactivity, *Journal of Materials Synthesis and Processing*, *8*(3), 197-203.

Tarigopula, V., C. Albertini, M. Langseth, O. Hopperstad, and A. Clausen (2009), A hydro-pneumatic machine for intermediate strain-rates: Set-up, tests and numerical simulations, paper presented at DYMAT Conf.

Tisato, N., G. Di Toro, N. De Rossi, M. Quaresimin, and T. Candela (2012), Experimental investigation of flash weakening in limestone, *Journal of Structural Geology*, *38*, 183-199.

Tullis, J., and R. A. Yund (1977), Experimental deformation of dry Westerly granite, *Journal of Geophysical Research*, *82*(36), 5705-5718.

Ward-Smith, A. (1979), Critical flowmetering: The characteristics of cylindrical nozzles with sharp upstream edges, *International Journal of Heat and Fluid Flow*, *1*(3), 123-132.

Yamashita, F., E. Fukuyama, K. Mizoguchi, S. Takizawa, S. Xu, and H. Kawakata (2015), Scale dependence of rock friction at high work rate, *Nature*, *528*(7581), 254-257.

Yang, X., L. Hector Jr, and J. Wang (2014), A combined theoretical/experimental approach for reducing ringing artifacts in low dynamic testing with servo-hydraulic load frames, *Experimental Mechanics*, *54*(5), 775-789.

Yao, L., S. Ma, A. R. Niemeijer, T. Shimamoto, and J. D. Platt (2016a), Is frictional heating needed to cause dramatic weakening of nanoparticle gouge during seismic slip? Insights from friction experiments with variable thermal evolutions, *Geophysical Research Letters*, *43*(13), 6852-6860.

Yao, L., S. Ma, J. D. Platt, A. R. Niemeijer, and T. Shimamoto (2016b), The crucial role of temperature in high-velocity weakening of faults: Experiments on gouge using host blocks with different thermal conductivities, *Geology*, *44*(1), 63-66.

Yuan, F., and V. Prakash (2008), Slip weakening in rocks and analog materials at co-seismic slip rates, *Journal of the Mechanics and Physics of Solids*, *56*(2), 542-560.

APPENDIX

NOMENCLATURE

AP	Area portion
DAQ	Data acquisition system
DoF	Degree of freedom
ELSE	Earthquake-like slip events
FW	Flash weakening
HSB	High-speed biaxial apparatus
HSLS	High-speed loading system
IR	Infra-red
LLMT	Lower Limit of Measurable Temperatures (for the IR camera)
NS	Normal stress
NSR	Normal stress ratio
PDE	Partial differential equations
PPCV	Pre-set control variables
QAV	Quick active valve
ULMT	Upper Limit of Measurable Temperatures (for the IR camera)
WG	Westerly granite
A^*	Area of the vena contracts

A_d	Effective area of the damper piston plate
A_{do}	Area of the damper orifice
A_P	Effective area of the pneumatic piston plate
A_t	Area of the orifice throat (at the exhaust port of the pneumatic cylinder)
C_0	Discharge coefficient of the orifice
C_d	Damping coefficient
c_{th}	Specific heat capacity
d_c	Characteristic slip distance related to dimension of micro-scale asperities
d_r	Displacement at t_r
D_a	Dimension of micro-scale asperities
D_c	Dynamic weakening characteristic slip distance
E	Young's modulus of elasticity
F_d	Damping force
F_{dc}	Force capacity of the damper
F_{lower}	Force generated by P_L acting on the pneumatic piston
F_s	Resistive force of the sample
F_{s0}	Friction strength (force) at quasi-static sliding rates
ΔF_s	Change in friction force (peak to steady state)
F_{Upper}	Force generated by P_U acting on the pneumatic piston

h_d	Height of the lower chamber of the damper
h_{do}	Initial height of the lower chamber of the damper
h_L	Initial height of the lower chamber of the pneumatic cylinder
HTG	Heterogeneity of contact areas
k_1	Stiffness of the rod connecting the damper plate to the pneumatic piston plate
k_2	Stiffness of the rod between the pneumatic piston plate and sample
K_{th}	Heat conductivity coefficient
m_d	Mass of the fluid in the lower chamber of the damper
m_g	Mass of the gas in the lower chamber of the pneumatic cylinder
m_t	Total mass of the moving parts
M	Mach number
P_0	Initial pressure in the pneumatic cylinder
P^*	Gas pressure at the vena contracta
P_c	Confining pressure
P_d	Pressure in the lower chamber of the damper
P_{ds}	Downstream pressure of the exhaust port of the pneumatic cylinder
P_e	Effective pressure (*Pc- Pp*)
P_L	Pressure in the lower chamber of the pneumatic cylinder
P_{max}	Maximum allowable pressure in the pneumatic cylinder

P_p	Pore pressure
P_U	Pressure in the upper chamber of the pneumatic cylinder
q	Heat generation rate per unit of area
R	Specific gas constant
t_r	Rise time of the velocity-step
T	Temperature
T_0	Initial temperature in the pneumatic cylinder
T^*	Temperature at the vena contracta
T_a	Ambient temperature
T_c	Temperature of micro-scale asperities
T_{c0}	Initial temperature of micro-scale asperities (surface temperature)
T_L	Temperature in the lower chamber
T_{mm}	Temperature at millimetric contact areas
T_s	Sliding surface temperature
T_w	Critical temperature for initiation of flash weakening at asperities
v^*	Flow velocity at the vena contracta
V_{d0}	Velocity of hydraulic fluid at the orifice of the damper
V_{dp}	Velocity of hydraulic fluid at the connection port of the damper
V_L	Volume of the lower chamber of the pneumatic cylinder
V_{L0}	Initial volume of the lower chamber of the pneumatic cylinder
V_U	Volume of the upper chamber of the pneumatic cylinder

V_{U0}	Initial volume of the upper chamber of the pneumatic cylinder
V_w	Minimum sliding velocity at which flash weakening occurs
y	Piston displacement in rigid model
z_1	Displacement of the damper piston plate
z_2	Displacement of the pneumatic piston plate
z_3	Displacement of the bottom of the pneumatic rod
α	Heat diffusivity (= $K_{th}/\rho c_{th}$)
β	Compressibility of the hydraulic fluid
γ	Specific heat ratio (c_p/c_v)
μ	Coefficient of friction
μ_0	Quasi-static coefficient of friction
μ_{ss}	Steady-state coefficient of friction
μ_w	Minimum value of coefficient of sliding friction in the flash weakening model (when $V >> V_w$)
τ	Shear stress
τ_c	Shear strength of micro-scale asperities
τ_{c0}	Shear strength of micro-scale asperities at quasi-static velocities
τ_{cw}	Shear strength of micro-scale asperities after weakening
ρ	Density
ρ_0	Initial gas density in the lower chamber of the pneumatic cylinder
ρ_L	Gas density in the lower chamber of the pneumatic cylinder
ρ_U	Gas density in the upper chamber of the pneumatic cylinder

ρ^*	Gas density at the vena contracta
ρ_d	Hydraulic fluid density in the damper
σ_c	Yield strength of micro-scale contacts in rock
σ_n	Normal Stress
θ	Lifetime of micro-scale asperities (= D_a/V)
θ_w	Time duration of slip at which a micro-scale asperity weakens